MICROSTRUCTURAL AND MECHANICAL PROPERTIES OF OXIDE DISPERSION STRENGTHENED INCONEL 718 ALLOYS PRODUCED BY SELECTIVE LASER MELTING

A THESIS SUBMITTED TO
THE GRADUATE SCHOOL OF NATURAL AND APPLIED SCIENCES
OF
MIDDLE EAST TECHNICAL UNIVERSITY

BY

MERVE YEŞİM YALÇIN

IN PARTIAL FULFILLMENT OF THE REQUIREMENTS
FOR
THE DEGREE OF MASTER OF SCIENCE
IN
METALLURGICAL AND MATERIALS ENGINEERING

JANUARY 2023

Approval of the thesis:

MICROSTRUCTURAL AND MECHANICAL PROPERTIES OF OXIDE DISPERSION STRENGTHENED INCONEL 718 ALLOYS PRODUCED BY SELECTIVE LASER MELTING

submitted by **MERVE YEŞİM YALÇIN** in partial fulfillment of the requirements for the degree of **Master of Science** i**n Metallurgical and Materials Engineering, Middle East Technical University** by,

Prof. Dr. Halil Kalıpçılar
Dean, Graduate School of **Natural and Applied Sciences** _____

Prof. Dr. Ali Kalkanlı
Head of the Department, **Met. and Mat. Eng., METU** _____

Assist. Prof. Dr. Eda Aydoğan Güngör
Supervisor, **Met. and Mat. Eng., METU** _____

Examining Committee Members:

Prof. Dr. C. Ali Kalkanlı
Metallurgical and Materials Eng., METU _____

Assist. Prof. Dr. Eda Aydoğan Güngör
Metallurgical and Materials Eng., METU _____

Prof. Dr. C. Hakan Gür
Metallurgical and Materials Eng., METU _____

Prof. Dr. F. Arcan Dericioğlu
Metallurgical and Materials Eng., METU _____

Prof. Dr. Ziya Esen
Department of Inter-Curricular Courses, Çankaya University _____

Date: 26.01.2023

I hereby declare that all information in this document has been obtained and presented in accordance with academic rules and ethical conduct. I also declare that, as required by these rules and conduct, I have fully cited and referenced all material and results that are not original to this work.

Name, Last name : M. Yeşim Yalçın

Signature :

ABSTRACT

MICROSTRUCTURAL AND MECHANICAL PROPERTIES OF OXIDE DISPERSION STRENGTHENED INCONEL 718 ALLOYS PRODUCED BY SELECTIVE LASER MELTING

Yalçın, Merve Yeşim
Master of Science, Metallurgical and Materials Engineering
Supervisor: Assist. Prof. Dr. Eda Aydoğan Güngör

January 2023, 141 pages

The efficiency of the systems generally increases with increasing service temperatures. For instance, high operation temperatures in the energy industry reduce operation costs, fuel consumption, and environmental pollution. Similarly, high service temperatures result in a longer range, higher carrying capacity, and performance in aerospace applications. However, service temperatures of currently used Nickel-based superalloys especially in aerospace and defense applications are limited below 700 °C. The formation of nano-sized oxide particles in the materials has been shown to improve the thermal stability and mechanical properties of the materials. In this study, three grades of oxide dispersion strengthened (ODS) Inconel 718 alloys were produced with the selective laser melting (SLM) method, and their microstructural and mechanical properties were investigated. The compositions of the alloys were determined as IN718-Y (IN718 – Y_2O_3), IN718-YF (IN718 – Y_2O_3 – FeO), and IN718-YFH (IN718 – Y_2O_3 – FeO – Hf) using thermodynamic CALPHAD (CALculation of PHAse Diagrams) calculations. Before the production of the samples, various power (P) and velocity (V) parameters were used to find the

optimum SLM processing parameters for each alloy. As-built (AB) alloys produced with the optimized parameters had > 99.7% densification, but the existence of detrimental phases such as Laves, which deteriorate mechanical properties, was detected in the microstructures of all the grades. Since the part undergoes fast heating and cooling cycles with thermal gradients up to 10^6 K/s during SLM production, detrimental phases start to form in the microstructure. In order to remove the detrimental phases which are resulted from rapid cooling during processing and promote the further precipitation of the nano-oxide particles, heat treatment was applied at 1050°C for 1 hour to all the grades. In heat-treated (HT) conditions, according to scanning electron microscopy (SEM) and energy dispersive spectroscopy (EDS) analyses, increases in oxide amounts, and some remaining Laves phase particles in IN718-Y, IN718-YF, and IN718-YFH grades were detected. Transmission electron microscopy (TEM) analyses revealed a significant increase in nano-oxide number density and in-situ tensile tests conducted at room temperature (RT) and 700°C showed an increase in tensile strengths for all the grades in HT condition.

Keywords: Oxide Dispersion Strengthening, Inconel 718, Nano-Oxide, Selective Laser Melting, Additive Manufacturing

ÖZ

SEÇİCİ LAZER ERGİTME İLE ÜRETİLEN OKSİT DİSPERSİYONU İLE GÜÇLENDİRİLMİŞ INCONEL 718 ALAŞIMLARININ MİKROYAPISAL VE MEKANİK ÖZELLİKLERİ

Yalçın, Merve Yeşim
Yüksek Lisans, Metalurji ve Malzeme Mühendisliği
Tez Yöneticisi: Dr. Eda Aydoğan Güngör

Ocak 2023, 141 sayfa

Sistemlerin verimi, genellikle artan servis sıcaklıkları ile artar. Örneğin, enerji endüstrisindeki yüksek çalışma sıcaklıkları, işletme maliyetlerini, yakıt tüketimini ve çevre kirliliğini azaltır. Benzer şekilde, yüksek servis sıcaklıkları, havacılık uygulamalarında daha uzun menzil, daha yüksek taşıma kapasitesi ve performans ile sonuçlanır. Bununla birlikte, özellikle havacılık ve savunma uygulamalarında halihazırda kullanılan Nikel bazlı süperalaşımların servis sıcaklıkları 700 °C ile sınırlıdır. Malzemelerde nano boyutta oksit partiküllerin oluşumunun, malzemenin termal kararlılığını ve mekanik özelliklerini iyileştirdiği gösterilmiştir. Bu çalışmada, seçici lazer ergitme (SLM) yöntemi ile farklı tip ve miktarlarda oksit oluşturucu içeren oksit dispersiyonu ile güçlendirilmiş (ODS) Inconel 718 alaşımları üretilmiş ve bunların mikroyapısal ve mekanik özellikleri incelenmiştir. Alaşımların bileşimleri termodinamik CALPHAD (CAlculation of PHase Diagrams) hesaplamaları kullanılarak IN718-Y (IN718 – Y_2O_3), IN718-YF (IN718 – Y_2O_3 – FeO) ve IN718-YFH (IN718 – Y_2O_3 – FeO – Hf) olarak belirlenmiştir. Numunelerin üretilmesinden önce, her bir alaşım için optimum SLM üretim parametrelerini bulmak için çeşitli güç (P) ve hız (V) parametreleri kullanılmıştır. Optimize edilmiş

parametrelerle üretilen üretim sonrası (AB) alaşımları > %99.7 yoğunluğa sahipti, ancak tüm laşımların mikroyapılarında mekanik özelliklere olumsuz etkisi olan Laves fazı gibi zararlı etkisi olan fazların varlığı tespit edilmiştir. Parça, SLM üretimi esnasında hızlı ısınma ve soğuma döngülerinin sonucu olarak 10^6 K/s' ye ulaşan termal gradyanlara maruz kaldığından, mikroyapıda zararlı etkisi olan fazlar oluşur. SLM üretimi sırasında oluşmuş olan zararlı fazları gidermek ve daha fazla nano-oksit partiküllerinin oluşmasını sağlamak için tüm alaşımlara 1050°C'de 1 saat boyunca ısıl işlem uygulanmıştır. Isıl işlem görmüş (HT) durumda, taramalı elektron mikroskobu (SEM) ve enerji saçılım spektroskopi (EDS) analizlerine göre, oksit miktarlarında artış ve bir miktar laves partiküllerinin varlığını sürdürdüğü IN718-Y, IN718-YF ve IN718-YFH alaşımlarında tespit edildi. Geçirimli elektron mikroskobu (TEM) analizleri, nano-oksit sayı yoğunluğunda kayda değer bir artış olduğunu; oda sıcaklığı (RT) ve 700°C'de gerçekleştirilen çekme testleri de HT durumdaki tüm alaşımlar için çekme mukavemetlerinde bir artış olduğunu göstermiştir.

Anahtar Kelimeler: Oksit Dispersiyonu İle Güçlendirme, Inconel 718, Nano-Oksit, Seçici Lazer Ergitme, Eklemeli İmalat

To my precious mother

ACKNOWLEDGMENTS

I wish to express my deepest gratitude to my supervisor Assist. Prof. Dr. Eda Aydoğan Güngör for her guidance, advice, criticism, encouragement, insight, endless support, and endless patience throughout this study.

I wish to thank the members of the examining committee Prof. Dr. Ali Kalkanlı, Prof. Dr. Arcan Dericioğlu, Prof. Dr. Hakan Gür, and Prof. Dr. Ziya Esen for their valuable feedback to improve this thesis.

I wish to thank Prof. Dr. C. Bora Derin for carrying out the thermochemical simulations which were used to determine the ODS alloy compositions in this study.

I would like to thank Scientific and Technological Research Council of Turkey (under grant number: 219M500) for financial support during this work. Also, I would like to thank the technical staff of METU Central Laboratory for their assistance in TEM, SEM, EBSD, ICP, and EA analyses.

I would like to thank MATEXA-LAB members Umut Tukaç, Ali Özalp, Berk Tanrısevdi, Hasan Koç, Kadir Demirci, Alkım Gökbayrak, and Yavuz Yıldız for their help and advice.

I would like to thank Süha Tirkeş and Tolga Ertürk for their help in conducting EDM cutting and in-situ tensile tests. Moreover, I would like to thank Can Okuyucu for his help in the preliminary TEM analyses of IN718-Y samples. Also, I would like to thank all the technical staff of the Metallurgical and Materials Engineering Department for their help and guidance during this work.

Finally, I am grateful to my mother and my brother for their endless love, support, and trust in every second of my life. I am also grateful to my partner for his help, support, suggestions, and love during this study as well as in our relationship. Having such a wonderful family has been the greatest support in taking one step further to accomplish this work.

TABLE OF CONTENTS

LIST OF TABLES

TABLES

LIST OF FIGURES

FIGURES

LIST OF ABBREVIATIONS

ABBREVIATIONS

AB	As-Built
AM	Additive Manufacturing
ASTM	American Society of Testing and Materials
BCT	Body Centered Tetragonal
BFTEM	Bright-Field Transmission Electron Microscopy
BSE	Backscattered Electron
CAD	Computer Aided Design
CALPHAD	Calculation of Phase Diagrams
EA	Elemental Analysis
EBM	Electron Beam Melting
EBSD	Electron Backscatter Diffraction
EDM	Electrical Discharge Machining
EDS	Energy Dispersive Spectroscopy
FCC	Face Centered Cubic
GCP	Geometrically Close-Packed
ICP-OES	Inductively Coupled Plasma Optical Emission Spectroscopy
IN718	Inconel 718
IN718-ODS	Oxide Dispersion Strengthened Inconel 718
HAADF	High-Angle Annular Dark-Field

HAGB	High Angle Grain Boundary
HB	Horizontally Built
HCP	Hexagonal Closed Packed
HIP	Hot Isostatic Pressing
HRTEM	High-Resolution Transmission Electron Microscopy
HT	Heat-Treated
HV	Vickers Hardness
HV1	Vickers Hardness Performed with 1 kg Load
IN718	Inconel 718
ISO	International Organization for Standardization
LAGB	Low Angle Grain Boundary
KAM	Kernel Average Misorientation
MA	Mechanical Alloying
Ni-based	Nickel-Based
NO	Nano-Oxide
ODS	Oxide Dispersion Strengthened
OM	Optical Microscopy
RT	Room Temperature
SAED	Selected Area Electron Diffraction
SEM	Scanning Electron Microscopy
SLM	Selective Laser Melting
STEM	Scanning Transmission Electron Microscopy

TCP	Topologically Close-Packed
TEM	Transmission Electron Microscopy
VB	Vertically Built
VIM	Vacuum Induction Melting

LIST OF SYMBOLS

SYMBOLS	
γ	Gamma – Austenite Phase
γ'	Gamma Prime Phase
γ''	Gamma Double Prime Phase
η	Eta Phase
δ	Delta Phase
σ	Sigma Phase
μ	Mu phase
%	Percentage
wt.%	Weight Percent
≤	equal to or less than

CHAPTER 1

INTRODUCTION

IN718 is a Ni-based superalloy which was developed to meet the requirement of the materials for high temperature applications such as gas turbine engines, turbine blades, aircraft skins, nuclear reactors, and combustion chambers. Having superior high-temperature mechanical properties such as high tensile and creep strength, high creep, oxidation, and wear resistance have made IN718 alloys as one of the widely used materials for high-temperature applications. The strengthening is mainly provided by coherent γ' and γ" precipitates, that nucleate during heat treatment and cooling, in the FCC γ matrix, so IN718 alloys are used in HT (or precipitation hardened) condition. Above 650 °C, precipitates start to dissolve and coarsen which causes increase in lattice mismatch and loss of coherency resulting in the formation of different precipitates at the expense of strengthening precipitates. The alloy starts to lose its strength due to the lack of γ' and γ" phases. Therefore, the service temperature of IN718 alloy is limited with 650 °C.

Most of the oxides have high melting points up to ~2500 °C which provides high stabilities at the temperatures up to 1200°C. In order to improve the strength of the matrix at elevated temperatures, ODS is applied. In oxide dispersion strengthening, oxides/oxide formers are added to where the oxide/oxide former has almost no solubility. Thus, there would be no dissolution/transformation of the strengthening phase at elevated temperatures, contrary to the precipitation strengthening.

Conventionally, IN718 alloy is produced by different casting methods which are followed by secondary processes. The main problems observed during conventional production methods are segregation, Laves phase formation, porosity, and coarse-

sized columnar grains that have sizes up to a few mm with non-uniform grain size distributions. After conventional production, a material is exposed to several machining and shaping operations in which a huge amount of material waste, and also energy loss is generated. The main limitation of conventional methods is to produce complex shaped products which are obtained by machining. In addition, high wear resistance and low material removal rate of IN718 make machining difficult and pricy mainly due to the requirement of special tools. Besides, the defects induced by machining processes deteriorate the surface quality and the strength of the material.

In order to produce dense, near-net shaped, and complex shaped products at one step without damaging the part, generating of material waste, and losing energy, AM methods are found to be promising. AM is a production technique in which the CAD model is used to build a 3D solid product. SLM is the most commonly used AM method for production of IN718 alloy products. SLM is a powder bed fusion process in which a high-intensity laser is used as energy source to melt and fuse the selected areas of the powder bed in layer-by-layer manner under an inert gas atmosphere. The main problem associated with SLM method is high thermal gradients that a product experiences during processing. High thermal gradients promote segregations and formation of detrimental phases such as Laves phase due to insufficient time for diffusion to get the equilibrium microstructure. Compared with coarse grain size up to a few mm and macro-scale segregations of detrimental phases in conventional methods, SLM method is still promising due to the existence of segregations at the micro-scale and a resultant microstructure that consists of smaller grains (~ 100 μm). As an addition to problems related with conventional methods, due to having lower densities, oxides tend to agglomerate, accumulate and float on the top of the molten alloy during casting process that results in an inhomogeneous microstructure with heterogeneously-distributed coarse oxides.

This study aims to produce oxide dispersion strengthened IN718 alloy that has >99% densification using SLM method. Thus, three different ODS alloys were designed.

First, the type and amount of oxide/oxide formers and the compositions of ODS alloys were determined using thermodynamic simulations using CALPHAD method. Y_2O_3, FeO, and Hf powders were added to IN718 alloy to promote Y-Ti-O and Y-Hf-O NO formations. Then, mechanical mixing time was optimized to get mechanical bonding between oxide/oxide former and IN718 powders without losing initial size and spherical shape of IN718 powders. Various power (W) and velocity (mm/s) parameters were used to optimize process parameters for the SLM productions of the designed ODS alloys. A series of heat treatments at different temperatures were applied to AB ODS alloys to determine the optimum heat treatment temperature. 1050 °C was found as optimum temperature and then the heat treatment duration was optimized for 1050 °C. Heat treatments with 0.5h time intervals up to 4h were applied and 1h was determined as the optimum duration for the heat treatment conducted at 1050 °C. Moreover, microstructural characterizations of AB and HT ODS alloys were carried out. Also, tensile tests were performed on AB and HT alloys according to ISO 6892-1 and ISO 6892-2 standards to investigate the mechanical behaviors of the alloys at RT and 700 °C.

This thesis consists of five main chapters that provide information on the subjects investigated in the present research. To provide the detailed information about IN718 alloy, oxide dispersion strengthening, and the production methods used for IN718, Chapter 2 is divided into six subsections. First, the investigations of superalloys, the microstructural and mechanical properties of Ni-based superalloys, strengthening mechanisms obtained in Ni-based superalloys are reviewed in Section 2.1 and Section 2.2. Then, the information about conventional production methods that are used for IN718 was given to address the problems associated with the conventional production methods and to understand the underlying reasons for the uses of powder-bed-based AM methods in Section 2.3. Moreover, the powder bed based AM processes were introduced to provide detailed information about the common use of SLM processes for IN718 alloy production in Section 2.4. In Section 2.5, a literature review on microstructural and mechanical properties of SLM'ed IN718 alloys in AB condition and HT condition was given. In addition, a detailed information about ODS

method was provided in Section 2.6. Chapter 3 includes the detailed information about initial materials, the experimental setup, optimization of mixing strategy, SLM processing, heat treatment optimization, and microstructural and mechanical property characterization methods. In Chapter 4, the results obtained in the present study are given and discussed in terms of densification, microstructural and mechanical properties for AB and HT alloys. Finally, the conclusions obtained at the end of this study are given in Chapter 5.

CHAPTER 2

LITERATURE REVIEW

2.1 Superalloys

Superalloys are defined as Nickel-based, Nickel-Iron-based, and Cobalt-based alloys having service temperatures above 540 °C [1,2]. As it is inferred from the name, superalloys were invented due to a lack of available materials that can be used at elevated temperatures at which Titanium (Ti) alloys have poor oxidation resistance, ferritic steels have poor creep and corrosion resistance, and structural stability, and ceramics have poor toughness and ductility [1,3]. High-temperature applications in which superalloys have been used include gas turbine engines, combustor chambers, nuclear reactors, aircraft skins, conveyor belts, and turbine blades [1–5]. Microstructures of superalloys consist of FCC γ matrix with different combinations of FCC carbides, FCC γ', BCT γ", HCP η, orthorhombic δ, and TCP (μ phase, Laves phase, and σ) phases [4,6–10]. Figure 2.1 shows a schematic representation of the microstructure of Ni-based superalloys [7].

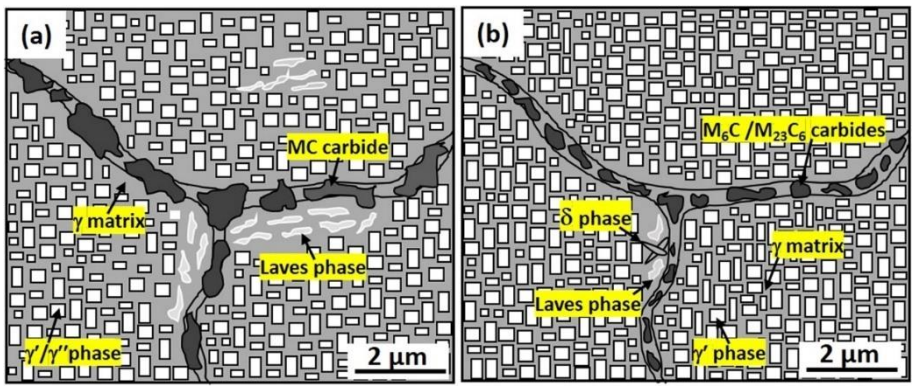

Figure 2.1. Schematic representation of the microstructure of Ni-based superalloys, a) without heat treatment, b) after heat treatment [7].

In terms of mechanical properties, superalloys are known for their superior high-temperature stabilities associated with high creep resistance, fatigue strength, oxidation, corrosion, wear resistance, and tensile strength up to the temperatures close to their melting points [11–13]. Figure 2.2 exhibits general stress-rupture strengths of superalloys at temperatures between 600 and 1200 °C for 100 h duration [14].

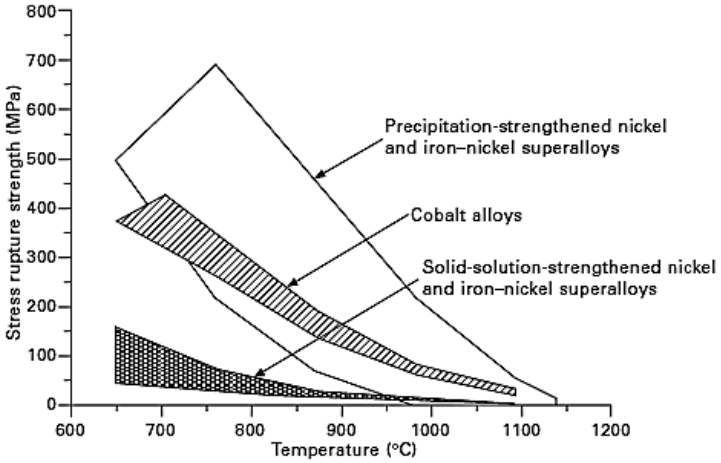

Figure 2.2. Stress-rupture behaviors of superalloys for 100h duration between 600 and 1200 °C [14].

2.2 Nickel-based Superalloys

Ni-based superalloys are types of superalloys in which Nickel is the main constituent element. Ni-based superalloys have high creep resistance, fatigue strength, toughness, and microstructural stability at elevated temperatures up to ~650 °C. Moreover, the cost of Ni-based superalloys is lower than Cobalt-based superalloys. Therefore, they are preferred for high-temperature applications rather than the other types of superalloys [3,15–18]. Since the main strengthening phases are γ' ($Ni_3(Al,Ti)$) and γ'' (Ni_3Nb), and the precipitation occurs during aging heat treatment, Ni-based superalloys are mostly used in precipitation hardened, or HT condition [2,14,19,20].

2.2.1 Microstructures of Nickel-based Superalloys

Typically, microstructures of Ni-based superalloys consist of FCC γ matrix, GCP intermetallics having A_3B stoichiometry, TCP intermetallics, carbides, nitrides, and oxides. GCP phases exist as γ' ($Ni_3(Al,Ti)$ – FCC), γ'' (Ni_3Nb – BCT), η (Ni_3Ti – HCP), δ (Ni_3Nb – Orthorombic) while TCP phases exist as σ (FeCr or NiCrMo – Tetragonal, layered), μ (FeMo – Rhombohedral), and Laves phase (NiCrFe-NbMoTi – Hexagonal structure) [1,2,4].

FCC γ matrix is mainly composed of Nickel, having broad solubility of secondary elements at elevated temperatures, which allows precipitations of intermetallic compounds such as γ' ($Ni_3(Al,Ti)$) and γ'' (Ni_3Nb) at lower temperatures. Moreover, densely packed Nickel matrix decreases the diffusivities of alloying elements providing phase stability at elevated temperatures [1,2,4]. Generally, Cr, Co, Mo, and W alloying elements are used as γ formers in γ matrix with the purposes of which are given in Table 2.1 [14,15,19].

Table 2.1. Roles of alloying elements in Ni-based superalloys [14,15,19].

Element	Function
Ni	To stabilize the FCC matrix, to inhibit the formation of detrimental phases, to form strengthening precipitates (γ' and γ'')
Cr	Solid solution strengthening, to increase corrosion resistance
Co	Solid solution strengthening, to decrease stacking fault energy to inhibit dislocation motion, to increase solvus temperature of γ'
W	Solid solution strengthening
Mo	Solid solution strengthening

γ' precipitate has $Ni_3(Al,Ti)$ stoichiometry with FCC crystal structure and spherical or cubic morphology. The morphology of γ' precipitate may vary according to its Mo content and Al/Ti ratio. Precipitation takes place at grain boundaries with a coherent interface having a lattice misfit of ≤ 0.5%. Moreover, γ' is a highly stable phase, so the existence of γ' precipitates at grain boundaries enhances the creep resistance and allows grain size control. Above 700 °C, due to coarsening, lattice mismatch increases that results in the formation of η (Ni_3Ti) at the expense of γ' phase. η phase has an HCP crystal structure and generally forms during prolonged exposure to high temperatures in the microstructures of Ni-based superalloys containing high Ti/Al ratios. Precipitation may occur as either intergranular or intragranular platelets [1–4,20,21]. Figure 2.3 shows representative morphologies of γ' and η phases [9,22].

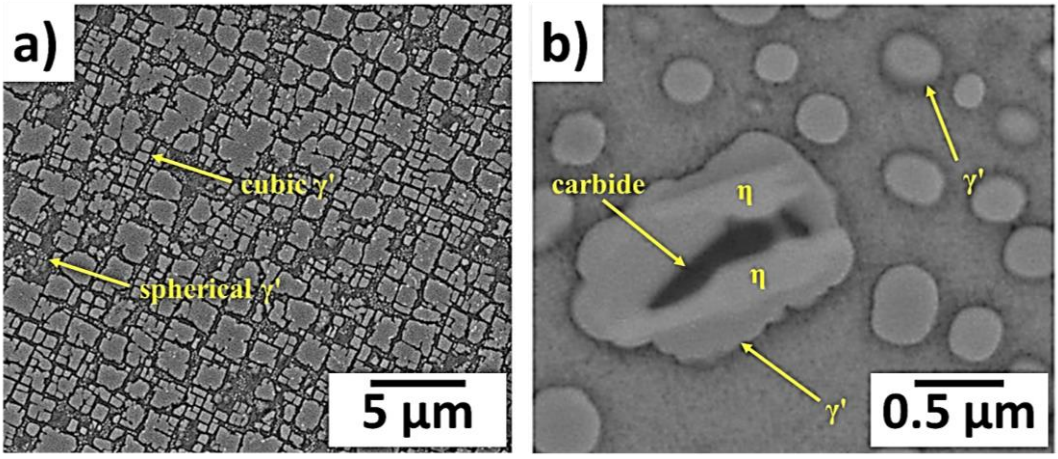

Figure 2.3. a) SEM micrograph showing γ' precipitates in René 108 alloy [22], b) SEM-BSE image showing η phase in Waspaloy [9].

γ'' precipitate has Ni_3Nb stoichiometry with BCT crystal structure and disk-shaped morphology. Precipitates start forming at grain boundaries with a coherent interface having a lattice misfit of ~2-3%. Due to lattice mismatch, coherency strains are formed in the microstructure which improves the strength of the alloy. Compared with the γ' precipitate, γ'' is considered as a principal strengthening phase for IN718 alloys, due to higher lattice mismatch between the particle and the matrix. On the other hand, γ'' phase is a metastable phase and it starts to transform into δ phase which is the thermodynamically stable form of Ni_3Nb compound above ~700 °C. δ

phase has an orthorhombic crystal structure and generally forms during over-aging. It forms an incoherent plate-like morphology and generally occurs at the intergranular regions [2,21,23,24]. Figure 2.4 shows representative disc-like/needle-like and plate-like morphologies of γ" and δ phases, respectively [25].

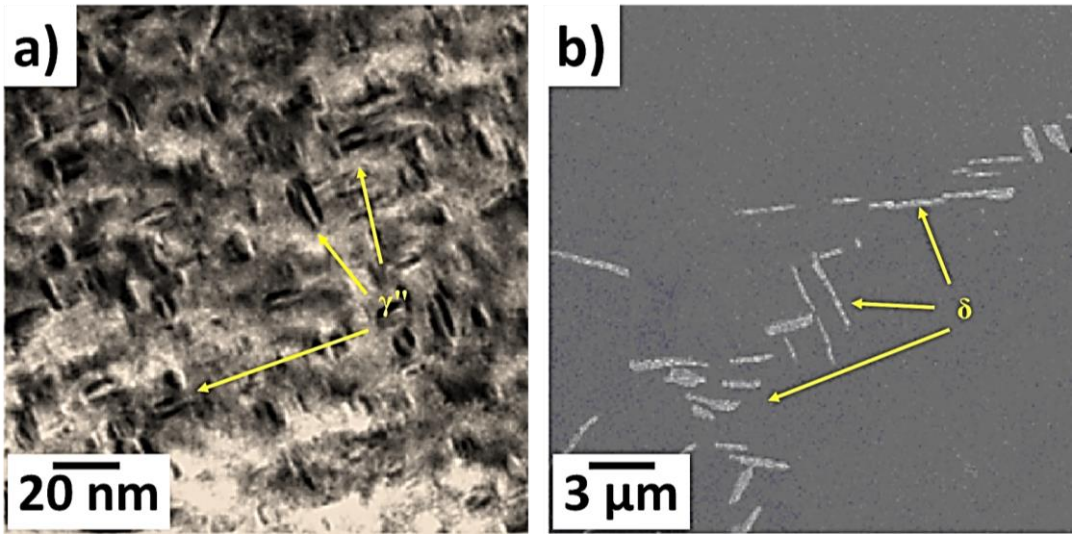

Figure 2.4. a) BFTEM micrograph showing γ" precipitates, b) SEM micrograph showing existing δ phase precipitated during heat treatments in IN718 microstructure [25].

Carbide phases may have MC, $M_{23}C_6$, and M_6C stoichiometries depending on Carbon (C) content, existing Metal (M), heat treatment temperature and time, and service life. Metal element may be Ti, Nb, Hf, W, Cr, Mo, Ta, or Co [2,4,26–28]. Carbide precipitation takes place either at the grain boundaries, called intergranular precipitation or within the grains, called intragranular precipitation. Moreover, the existence of carbide phases may contribute to strengthening depending on the precipitation mechanism. For example, carbides contribute to strengthening when the precipitation occurs as intragranular precipitation. On the other hand, if carbide precipitates exist as heterogeneously distributed discrete particles at grain boundaries, they inhibit grain boundary sliding, resulting in grain size control and an increase in the resistance against damage accumulation at the grain boundaries at elevated temperatures. However, if the carbides form as a continuous film at grain

boundaries, they act both as crack initiation sites and crack propagation paths which degrade mechanical properties, especially creep-rupture strengths of the materials [16,17]. Figure 2.5 represents continuous film-type and intragranular carbides observed in the 617B superalloy [29].

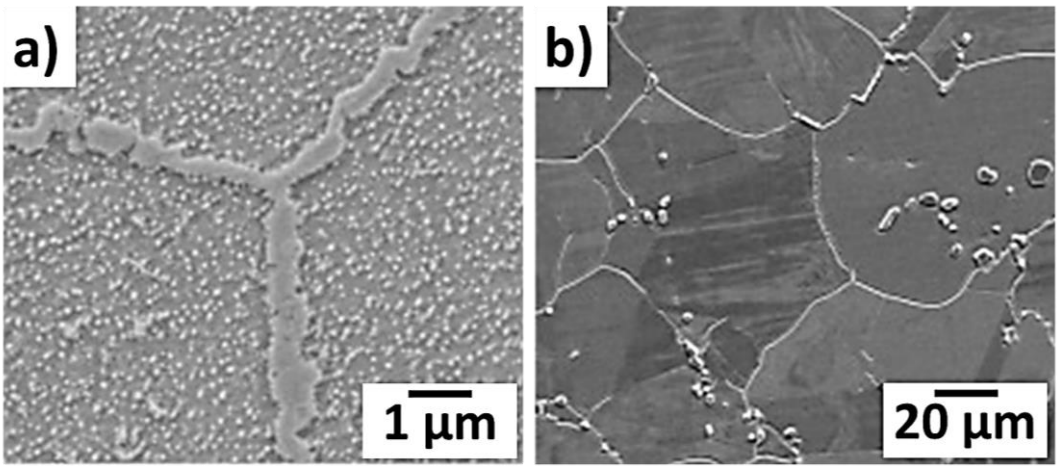

Figure 2.5. SEM micrographs of a) grain boundary carbides in continuous film form, b) intragranular carbides heterogeneously distributed in the matrix phase [29].

MC carbides have cubic crystal structures and exist as globular, irregularly shaped particles. As the precipitation takes place directly from the liquid phase during solidification at elevated temperatures, MC carbides are also named primary carbides. The elements having affinity to form MC carbides are Nb, Ti, Mo, Zr, W, Hf, V, and Ta. Moreover, precipitation occurs either in intragranular, where the individual particles are heterogeneously dispersed in interdendritic regions, or intergranular manner, in which the precipitation occurs at grain boundaries [2,4,16,30–32]. Depending on the composition of the primary MC phase and existing constituent elements in the superalloy, during long period high-temperature service life, MC carbides decompose into $M_{23}C_6$ type and M_6C type carbides in the following sequence [3,4,16]:

$$MC + \gamma \rightarrow M_{23}C_6 + \gamma' \qquad \text{(Eq.2.1)}$$

$$MC + \gamma \rightarrow M_6C + \gamma' \qquad \text{(Eq.2.2)}$$

$M_{23}C_6$ type carbides have FCC crystal structure and may form as globular precipitates, platelets, lamellar precipitates, films, and cells mostly at grain boundaries at ~750 °C. Since the precipitation takes place at the expense of MC carbides, $M_{23}C_6$ precipitates are named secondary carbides. The elements having affinity to form $M_{23}C_6$ carbides are Cr, Fe, Mo, W, Co, and Ni. $M_{23}C_6$ carbides have been reported to promote the complex structures like the σ phase, one of the TCP phases. Due to high coherency between $M_{23}C_6$ and σ phases, the σ phase generally starts to nucleate at $M_{23}C_6$ precipitates [2–4,19,33–35].

M_6C carbides have complex FCC crystal structures similar to $M_{23}C_6$ type carbides. However, the formation of M_6C carbides occurs at higher temperatures, ~800 °C, compared to $M_{23}C_6$ carbides. Moreover, higher amounts of Mo and/or W elements are required to promote the nucleation of M_6C carbides. In addition, Mo, W, Ni, Nb, Cr, and Ta elements have high affinity to form M_6C carbides. Besides, as the formation temperature of M_6C carbides is higher compared to $M_{23}C_6$ carbides, they are more stable at higher temperatures. Precipitation of M_6C carbides occurs as heterogeneously distributed particles in the matrix phase. They may precipitate as block-shaped particles or intragranular precipitates in a Widmanstätten pattern which degrades the ductility and rupture life of a material [2–4,36–38].

Borides have a tetragonal crystal structure and form in the microstructure when the amount of B is equal to or greater than 0.03 wt.%. Precipitation occurs mainly at grain boundaries similar to carbide precipitation. Boride precipitates are known as hard and they appear as block-shaped or half-moon shaped. The elements that have affinity to form borides are Ta, V, Nb, Mo, Ni, Cr, and Fe. Similar to the carbides, borides also inhibit grain boundary sliding, allow grain size control, therefore increase rupture strength when they exist in trace amounts in the microstructure [1,3,4,39–41]. Figure 2.6 represents block shaped borides existing in the microstructure of Ni-based superalloy, B1914 [42].

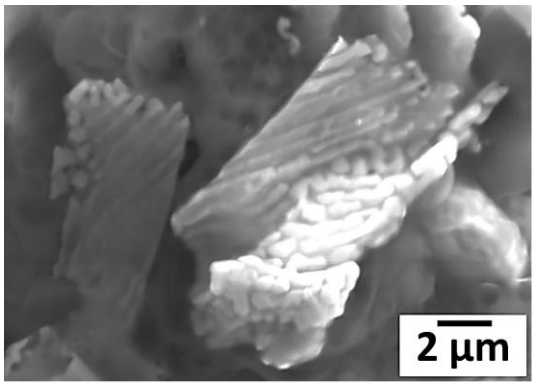

Figure 2.6. SEM-BSE micrograph showing block shaped borides in the as-cast microstructure of B1914 superalloy [42].

Nitrides have cubic crystal structure and precipitation is mainly observed in alloys that contain Ti, Nb, and/or Zr. Nitrides are insoluble up to around their melting point, and they may exist in the shapes of square to rectangular [1,4,43]. Other than Ti, Nb, and Zr elements, Si and Cr also have an affinity to form nitride phases [44]. Besides, during solidification, it is observed that nitrides act as nucleation sites for formation of primary carbide phases [2,45–47]. Nitrides take a role in improving hardness, corrosion and wear resistance of Ni-based superalloys [4,46,48]. However, Ni-based superalloys that contain relatively high amounts of N also tend to include excessive microporosity, and nitrides have low plastic deformation energy associated with reduced ductility and rupture strength [19,46]. Figure 2.7 shows a block-shaped nitride precipitate existing in Inconel 625 superalloy [44].

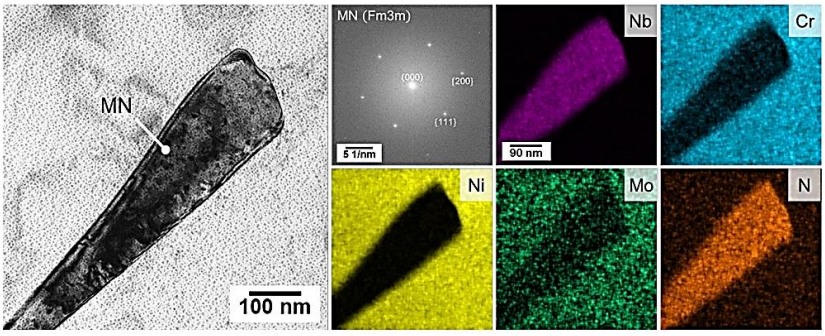

Figure 2.7. HRTEM micrograph (left), FFT micrograph, and qualitative EDS elemental maps of nitride (MN) phase in the as-deposited microstructure of Inconel 625 superalloy [44].

Oxides generally create an oxide layer on the surface and exist in Cr, Al, Mg, and Ni-Cr oxide forms. Oxide surface layer improves oxidation, corrosion and erosion resistance and strength of a Ni-base superalloy [1–3,14,49–52].

TCP phases consist of layers of closely packed atoms that are separated from one another by intervening layers of relatively large atoms. TCP phases have three distinct characteristics:

- Atoms are arranged in a configuration of high and uniform density
- Bonding is directional and non-metallic
- They consist complex crystal structures

These phases may form in plate-like or needle-like shapes and have brittle characteristics that cause degradation in rupture strength and ductility of an alloy. σ, μ, and Laves phases are the TCP phases observed in Ni-based superalloys [1,3,4,17]. σ phase has tetragonal, layered crystal structure and appears as elongated irregularly shaped globules. It is observed after long time high temperature exposure between 540 and 980 °C. Moreover, chemical composition of σ phase may be FeCr, FeCrMo, CrFeMoNi, CrNiMo and CrCo [2,53,54]. μ phase has rhombohedral crystal structure and generally appears as coarse, irregular Widmanstätten plates formed at high temperatures. Moreover, chemical composition of μ phase may be $(Fe,Co)_7(Mo,W)_6$ or Co_7W_6 [2,55,56]. Laves phase has $MgZn_2$ hexagonal crystal structure with a stoichiometry of AB_2 and observed after long time-high temperature exposure. A general formula showing chemical composition of Laves phase is $(Fe,Cr,Mn,Si)_2(Mo,Ti,Nb)$ and it may also appear as Fe_2Nb, Fe_2Ti, Fe_2Mo, Co_2Ta, and Co_2Ti. Moreover, they generally have elongated, irregularly shaped globular or plate-like morphology. Precipitation may occur as either intergranular or intragranular. In addition, Laves phase has brittle characteristics, thus, existence of it degrades ductility, corrosion resistance and rupture strength of an alloy [1,2,19,57–60]. Figure 2.8 exhibits the SEM images showing the morphology of Laves phase in the microstructure of laser direct energy deposited IN718 alloy in HT condition [61].

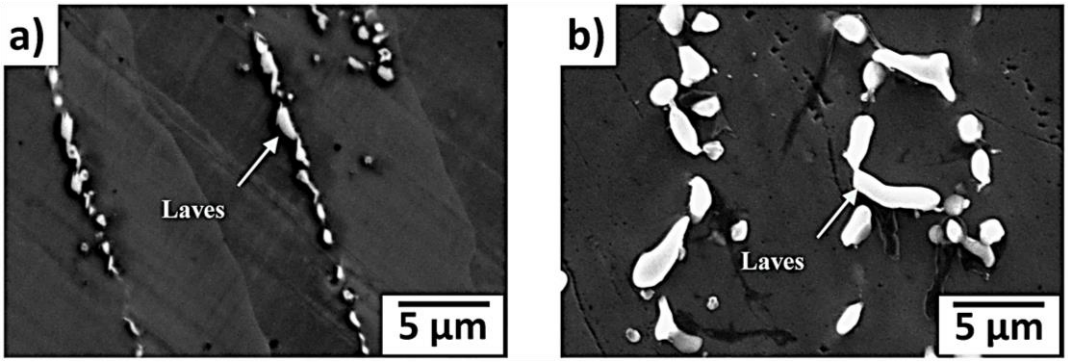

Figure 2.8. SEM micrographs showing laves phase morphologies in the microstructure of laser direct energy deposited IN718 superalloy: a) after heat treatment at 890 ℃ for 12 h followed by 1020 ℃ for 30 min, b) after heat treatment at 1020 ℃ for 30 min [61].

2.2.2 Mechanical Properties of Nickel-based Superalloys

Ni-based superalloys have been known by their outstanding high-temperature properties such as high creep resistance, high temperature corrosion and oxidation resistance, high temperature tensile strength, rupture strength, and fatigue strength [1,3,4,19,62]. Figure 2.9 shows tensile yield strengths of some of Ni-based superalloys between 0 and 900 °C [63]. In order to improve high temperature mechanical properties, some alloying elements are also added into γ matrix. Table 2.2 exhibits related alloying elements and their functions in Ni-based superalloys [1,19].

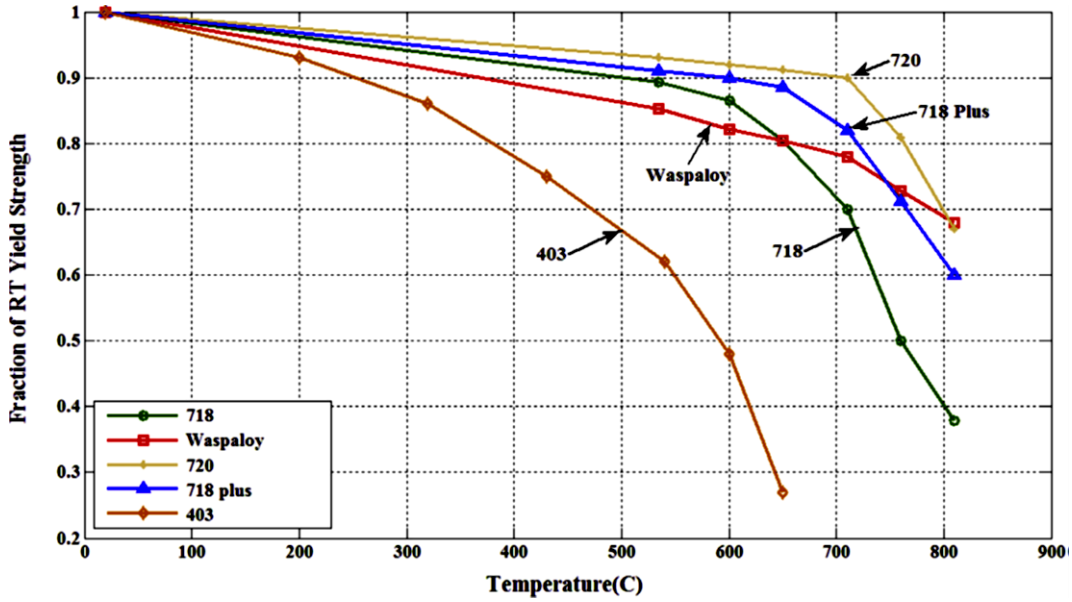

Figure 2.9. Tensile yield strengths of some Ni-based superalloys changing with temperature [63].

Table 2.2. Roles of alloying elements used to improve mechanical properties in Ni-based superalloys [1,19].

Role of the Alloying Element	Element
Solid solution strengthening	Co, Cr, Fe, Mo, W, Ta, Re
MC formation	W, Ta, Ti, Mo, Nb, Hf
$M_{23}C_6$ formation	Cr, Mo, W
M_6C formation	Mo, W, Nb
Carbonitride M(CN) formation	C, N
γ' formation	Al, Ti
γ' solvus temperature increasing	Co
Formation of hardening precipitates	Al, Ti, Nb
Improvement of oxidation resistance	Al, Cr, Y, La, Ce
Improvement of hot corrosion resistance	La, Th
Improvement of sulfidation resistance	Cr, Co, Si
Improvement of creep properties	B, Ta
Improvement of rupture strength	B
Grain boundary refining	B, C, Zr, Hf
Retardation of γ' coarsening	Re

2.2.3 Strengthening Mechanisms of Nickel-based Superalloys

About Ni-based superalloys, the principal requirement is to be stable both mechanically and microstructurally at elevated temperatures. High temperature strengthening is mainly provided by two mechanisms: solid solution strengthening

and precipitation/age hardening. For the case of precipitation/age hardening, γ' and γ'' precipitates form during subsequent heat treatments. These precipitates inhibit dislocation movement and pin grain boundaries providing both strengthening and grain size control [1,4,21].

2.2.3.1 Solid Solution Strengthening

In solid solution hardening, a different solute element is added into the matrix in order to enhance the strength of the matrix phase. Due to atomic size misfit, new element creates a distortion in the matrix which inhibits dislocation motion. So, increasing atomic size up to 10% increases solid solution strengthening. Moreover, when the melting point of solute element is high, lattice cohesion becomes stronger and diffusion becomes harder at elevated temperatures. On the other hand, main deformation mechanism in imperfect crystals at elevated temperatures is dislocation cross slip. Solid solution hardening decreases stacking fault energy (SFE) in the lattice, so it becomes harder for dislocation to change their directions and bypass a barrier by moving towards a new slip plane [2,4,19].

2.2.3.2 Precipitation Hardening

Precipitation hardening or age hardening, is a strengthening mechanism in which the matrix is strengthened by the existence of precipitates depending on precipitate-dislocation interactions and precipitate sizes. Precipitates inhibit dislocations by either cutting or looping (bowing/bypassing) mechanisms: if the precipitate size is too small, then dislocations cut through the precipitate; if the precipitate size is too big for cutting, dislocations leave loops around the precipitates, named Orowan looping/bowing [2,3]. Representative TEM micrograph of Ni-based superalloy showing the cutting and looping mechanisms is given in Figure 2.10 [64].

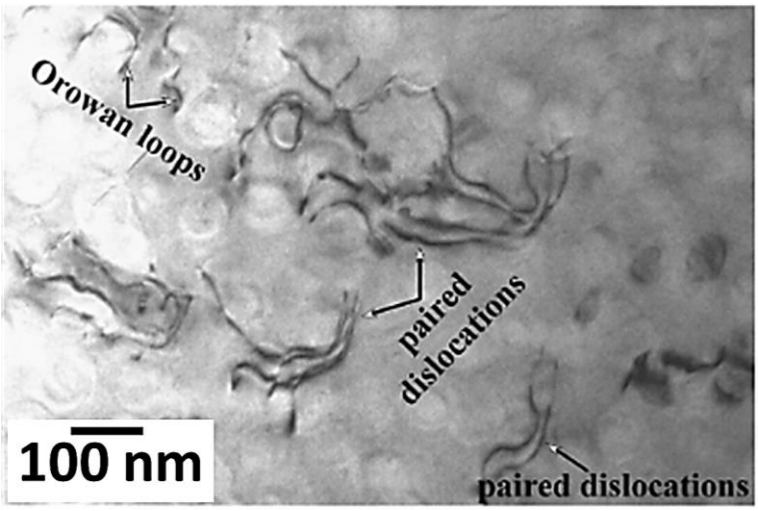

Figure 2.10. TEM micrograph of GH4037 superalloy showing the deformation of γ' precipitates by cutting (by paired dislocations) and Orowan looping [64].

In Ni-based superalloys, precipitation hardening is achieved by γ' ($Ni_3(Al,Ti)$) and γ'' (Ni_3Nb) precipitates. Moreover, precipitates generally form during heat treatment, so a heat treatment is required to provide precipitation hardening. Al, Ti, and Nb have low solubility in Ni matrix, and their solubility decreases with decreasing temperature. Thus, precipitates start to form in the matrix from a supersaturated solid solution during heat treatment. There are four main factors controlling the effectiveness of precipitation hardening:

- Particle sizes and morphologies of γ' and γ'' precipitates
- Volume fractions of γ' and γ'' precipitates
- Coherency strains between the matrix phase (γ) and γ' - γ'' precipitates originating from the lattice parameter differences. It should be noted that increasing coherency strains results in increasing strengthening as long as coherency is maintained.
- The anti-phase boundary energy (APBE) in the existence of ordered γ' and γ'' precipitates. The APBE is the energy required for the dislocation to cut through the ordered precipitate if the cutting results in disordering between the matrix and the precipitate phases. Since the precipitates are ordered,

dislocations in ordered phase require more energy to disorder the precipitate while passing through.

There are some limitations of precipitation hardening, though. First, when the alloy is exposed to high temperatures for long intervals, γ' precipitates start to transform into η phase and γ'' precipitates start to transform into δ phase which are detrimental for mechanical properties. Second, at temperatures above 700°C, γ' and γ'' precipitates start to experience rapid coarsening and dissolving in the matrix, which degrades precipitation strengthening [1,2,4,65–67].

2.3 Nickel-based Superalloys Produced by Conventional Methods

The conventional production methods involve the melting of the base alloy, addition of alloying elements to the molten metal, and casting of the molten metal into a solid product. Then, the forming process is applied to the solid product followed by machining and heat treatment [14,17]. For the case of Ni-based superalloys, VIM is required as primary melting process. VIM process is applied in vacuum environment, so Oxygen and Nitrogen amounts are kept at the lowest value to control the γ' and γ'' former elements, Al and Ti. Moreover, contaminations originated from slag and/or dross formation could be kept at minimum compared with other casting techniques applied in air. Vacuum arc remelting and electro-slag remelting processes are applied to materials as secondary melting processes. [3,68]. When investment casting is applied, VIM process is generally used as a single melting process [17]. Although common manufacturing methods for Ni-based superalloys are casting and investment casting, conventional methods are inadequate for the production of complex shaped products. Moreover, there are other limitations associated with conventional methods, such as existence of coarse grains that have columnar morphology with sizes up to several mm, non-uniform grain size distributions, segregations, porosities and Laves phase formation [69–73]. Figure 2.11 shows orientation maps of the as-cast alloy produced by investment casting and AB alloy deposited on top the as-cast alloy using direct metal deposition AM technique. EBSD

analyses indicate that the average grain size in AB alloy is determined as 43 µm while it is 1584 µm in as-cast alloy, as seen in Figure 2.11 (b) [72]. Besides, Figure 2.12 shows the extensive Laves phase segregation at the grain boundaries in as-cast microstructure of IN718 alloy [74].

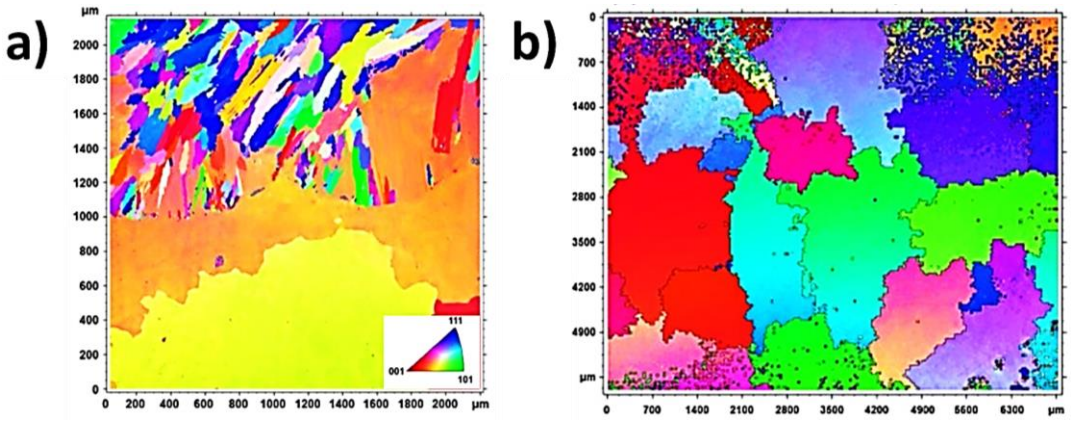

Figure 2.11. EBSD analysis microstructures of IN718 produced by different techniques a) Orientation map showing grain orientations. Upper part: direct metal deposition technique, bottom part: investment casting method; b) Grain map, as a result of investment casting, showing individual grains [72].

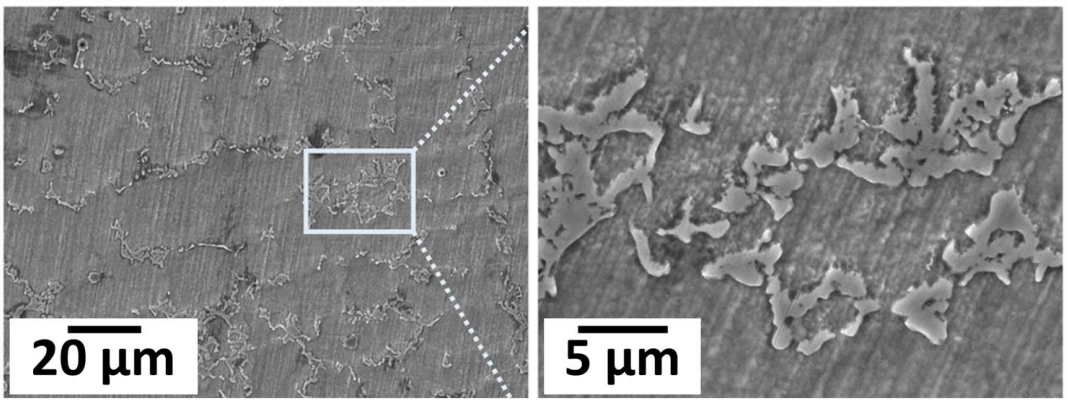

Figure 2.12. Grain boundary Laves phase segregation in the as-cast microstructure of IN718 produced by investment casting [74].

2.4 Additive Manufacturing Processes for Nickel-based Superalloys

AM is a production technique in which a 3D solid product is built by using CAD model in layer-by-layer deposition manner [75–78]. Ni-based superalloys are mostly used as complex shaped products such as turbine blades for high temperature applications. Production of complex shapes is one of the limitations of conventional production methods. Moreover, Ni-based superalloys have high strength and high wear resistance which results in difficulty in machining process when they are produced by conventional methods. In addition, large amount of waste is generated during machining process. Therefore, AM methods are used to produce Ni-based superalloys which allow production of complex and near-net shaped products having enhanced properties with reduced number of post-processing techniques and material loss [79–82]. Commonly used AM processes used for Ni-based superalloy production are based on powder bed fusion techniques which include SLM and EBM methods [79,83,84].

2.4.1 Selective Laser Melting

SLM is a powder bed fusion process in which a high-intensity laser is used as an energy source to melt and fuse the selected regions in powder bed layer by layer under an inert gas atmosphere according to a sliced CAD image. As the laser melts powders, a melt pool forms along the path of the laser. The melt pool is exposed to rapid cooling and forms a layer of solidified product. By SLM technique, almost full densification could be reached in the final product [76,85]. Figure 2.13 shows a schematic representation of the SLM process [86].

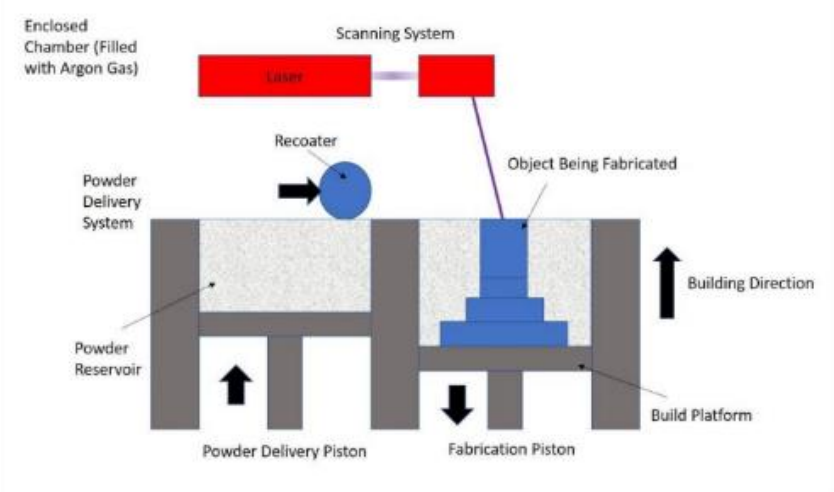

Figure 2.13. Schematic representation of the SLM process [86].

During SLM production, a part experiences high thermal gradient up to 10^6 K/s, i.e., rapid heating and cooling cycles [81,87,88]. Applying such high thermal gradients to a part causes high residual strains and discontinuities in the final part [89–91]. Since the thermal gradient is directly related with laser energy density, process parameters should be set properly. Typical process parameters include laser spot size, laser power (P), scanning speed (mm/s), layer thickness, hatch distance and scan rotation. It should be noted that the powder characteristics have critical effect on the microstructure, mechanical properties, surface roughness, and density of the final products [79,90,92–97].

As an advantage, SLM process allows to produce complex and near-net shaped products with minimum production time and material consumption [85,98]. However, high thermal gradient during the process is the main problem for the final parts produced with SLM method [91]. In addition to creating residual strains and discontinuities, high thermal gradient promotes segregations and formation of undesirable phases, such as Laves phase, due to insufficient time for diffusion [87,91,99]. In order to remove these side effects, usually post processing techniques such as heat treatment or HIP is applied to the final product [91,98,100–104].

2.4.2 Electron Beam Melting

EBM is one of the powder bed fusion processes in which electron beam is used as an energy source to fuse and melt the selected regions in powder bed in layer-by-layer manner according to the CAD image. Schematic representation of the EBM process is given in Figure 2.14 [105]. EBM is very similar to SLM with two main differences: first, an electron beam is used as the energy source, and second, EBM process is carried out in vacuum environment at 10^{-4} – 10^{-5} mbar levels. Carrying out the EBM process under vacuum prevents parts from oxidation [76,105]. Moreover, in EBM system, powder bed is allowed to be pre-heated above 800 °C. Therefore, the thermal gradient is minimized during the process which results in lower residual strains [105–107]. Reduced thermal gradients enables production of brittle materials by EBM method. Thus, brittle materials such as high entropy alloys can be produced without solidification cracks generated by high thermal gradients [106]. However, keeping the powder bed at elevated temperatures for such a long-time result in the formation of detrimental phases, like δ, in the microstructure of Ni-based superalloys [108–110]. Besides, processing at elevated temperatures requires long cooling times, generally overnight, to cool the powder bed after production which makes the EBM process quite slow [105–107].

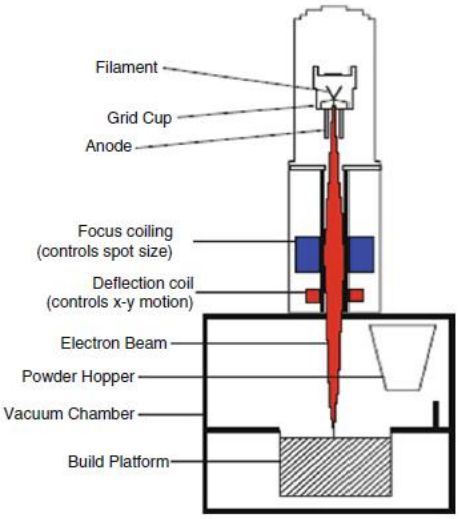

Figure 2.14. Schematic representation of the EBM method [105].

Compared to the SLM method, EBM process is not widely used due to higher cost, lower accuracy, and unfeasibility for the production of larger parts. A brief summary of characteristics of SLM and EBM processes is given in Table 2.3 [76,105].

Table 2.3. Characteristics of SLM and EBM methods [76,105].

Feature / Process	**SLM**	**EBM**
Power source	Fiber laser/s of 200-1000W	High power electron beam of 3kW
Process environment	Inert gas	Vacuum
Powder pre-heating temperature (°C)	100-200	700-900
Max available built volume (mm)	500x350x300	350x380 (dia x h)
Maximum build rate (cm^3/h)	20-35	80
Layer thickness (µm)	20-100	50-200
Melt pool size (mm)	0.1-0.5	0.2-1.2
Surface finish	Excellent to moderate	Moderate to poor
Feature resolution	Excellent	Moderate

2.5 Microstructural and Mechanical Properties of Inconel 718 Alloys Produced by Selective Laser Melting

IN718 alloy is a Ni-based superalloy in which the matrix phase is composed of Ni, Cr, and Fe elements. In addition to Ni, Cr, and Fe, there are other elements such as Nb, Mo, Ti and Al existing in minor amounts. The alloy is also known as UNS N07718, and the chemical composition is given in Table 2.4 [2,19,111]. IN718 superalloy is considered a high-performance alloy due to its superior oxidation resistance, corrosion resistance, and high strength up to 700 °C [2,112,113].

Conventional production methods have limitations for the production of complex-shaped and fully dense final parts consisting relatively small grains and homogeneous microstructure without segregations [71–74,82], Most of these problems could be solved or minimized by production of IN718 parts with AM method [95,98,114]. SLM method is one of the widely used processes for the manufacturing of IN718 components [85,106].

Table 2.4. Nominal composition of wrought IN718 alloy [2,19,111].

Element	Composition (wt.%)
Ni	52.5
Cr	19
Fe	18.5
Mo	3.0
Nb	5.1
Ti	0.9
Al	0.5
C	0.08 max
Cu	0.15 max

2.5.1 Inconel 718 Alloys in As-Built Condition

AB condition is the condition of the final part right after the SLM production. Microstructure of an SLM-produced IN718 alloy consists of distinct melt pools, columnar dendrites along the building direction, cellular substructures, Nb-Mo-Ti segregations indicating the formation of Laves phase, delta phase, and carbides [58,115–117]. Figure 2.15 presents a typical microstructure of an AB IN718 part

[118]. The reason behind the formation of such a microstructure is related with high thermal gradients and lack of time for diffusion during the SLM process [87,91,99].

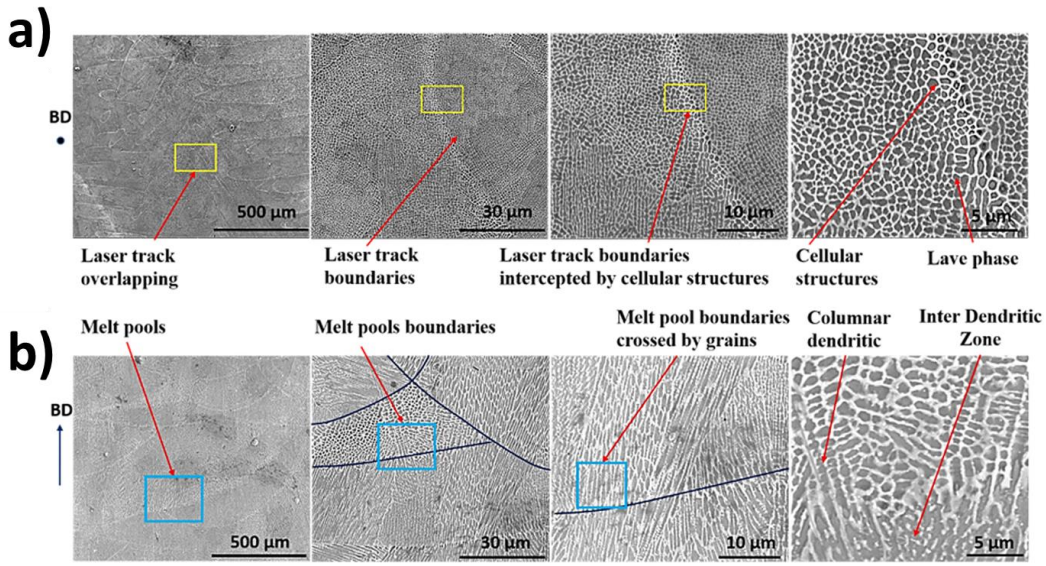

Figure 2.15. SEM micrographs of IN718 alloy produced by SLM: a) along the building direction, b) across the building direction [118].

Laves and δ phases are incoherent with the matrix and they have irregular, block-shaped and needle-like geometries, respectively. Due to having such geometries and sharp corners, these precipitates may act as stress concentrators and crack initiators in the microstructure. Therefore, the existence of Laves and δ phases degrades the mechanical properties of IN718 alloys [2,19,21,82,119]. Figure 2.16 exhibits a BFTEM micrograph showing the morphologies of typical Laves and δ precipitates in AB IN718 alloy produced by SLM method [21].

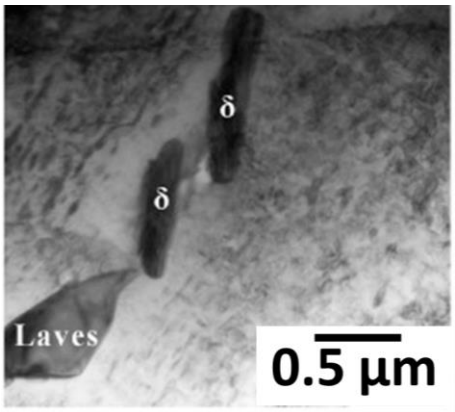

Figure 2.16. BFTEM micrograph showing needle-like δ and block-shaped laves precipitates [21].

In terms of mechanical properties, yield strength, tensile strength, and elongation of AB IN718 parts produced by SLM range roughly between 600 and 1000 MPa, 800 and 1200 MPa, and 15-35%, respectively [58,113,119–124]. When compared with conventional cast and wrought IN718 alloys, SLM-ed alloys have higher tensile strength than cast alloys and lower tensile strength than wrought alloys. The reason of having lower strength than wrought alloys is that during forging, precipitation of strengthening phases takes place while there is no such occasion during SLM process. In order to provide strengthening by γ' and γ" precipitates, various heat treatments are applied to AB IN718 alloys [82,98,125–127]. Figure 2.17 shows comparison of tensile strengths of IN718 alloys produced by different methods [113].

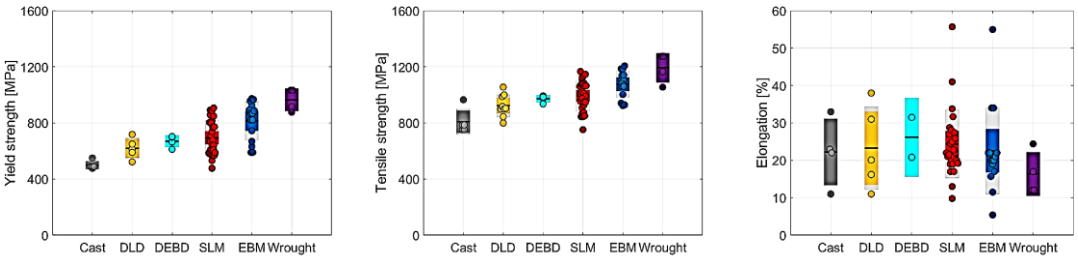

Figure 2.17. Comparisons of yield strength, tensile strength, and elongation values of AB IN718 alloys produced with SLM, EBM, DLD (direct laser deposition), DEBM (direct electron beam (wire) deposition) metal AM methods, as-cast IN718 alloys, and wrought IN718 alloys [113].

2.5.2 Inconel 718 Alloys in Heat-Treated Condition

There are mainly three types of heat treatments applied to AB IN718 alloy: homogenization heat treatment, solutionizing heat treatment, and aging heat treatment. The ultimate aim in homogenization and solutionizing heat treatments is to dissolve detrimental phases, such as Laves, in the microstructure. Aging heat treatment is applied to IN718 alloy to promote the nucleation of strengthening precipitates, γ' and γ'', which provides precipitation strengthening [21,100,102,128]. In order to apply a successful heat treatment, the time and temperature of the heat treatment should be well-designed considering the time-temperature-transformation (TTT) diagram of IN718 alloy given in Figure 2.18 [129].

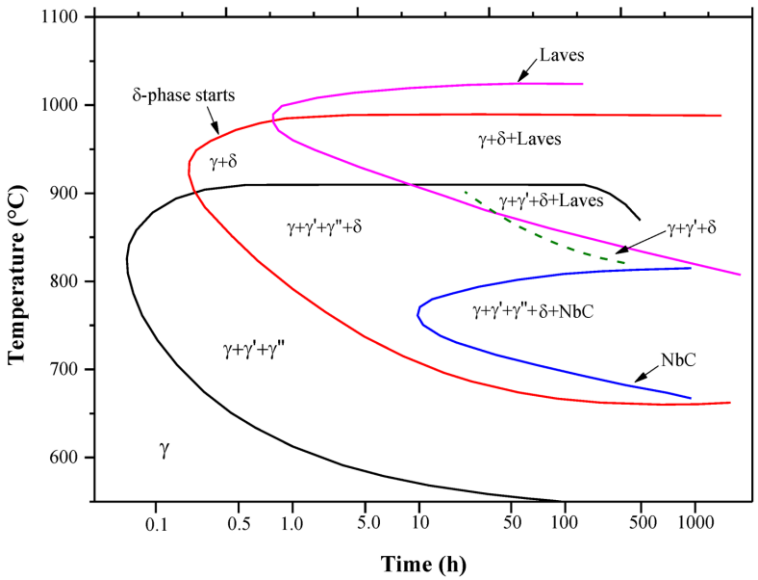

Figure 2.18. TTT diagram of IN718 alloy [129].

Generally, homogenization and/or solutionizing heat treatments are applied as an initial heat treatment step and it is followed by aging heat treatment. At the end of the heat treatments, the microstructure consists of some residual Laves phase, carbides, γ', γ'', and δ phases [21,101,102,130]. In HT condition, a significant improvement in mechanical properties is observed. Yield strength, tensile strength, and elongation of HT IN718 parts range roughly between 900 and 1100 MPa, 1200 and 1500 MPa, and 5-25%, respectively [113].

2.6 Oxide Dispersion Strengthening

Oxide dispersion strengthening is a strengthening method in which the matrix of an alloy is strengthened by oxide dispersoids which are stable at elevated temperatures. In oxide dispersion strengthening, used oxide/oxide former elements/compounds have almost no solubility in the alloy matrix, so there will be no dissolution of the strengthening phase in the matrix phase at elevated temperatures, contrary to the precipitation strengthening [1,2,4,131]. In addition to high temperature stability, oxides have high strengths at elevated temperatures which improves strength, oxidation resistance, corrosion resistance, creep resistance, and irradiation resistance of the alloy at elevated temperatures [1,2,4,132–139]. Figure 2.19 represents the strengthening effect in ODS alloys on tensile properties between RT and 900 °C [133].

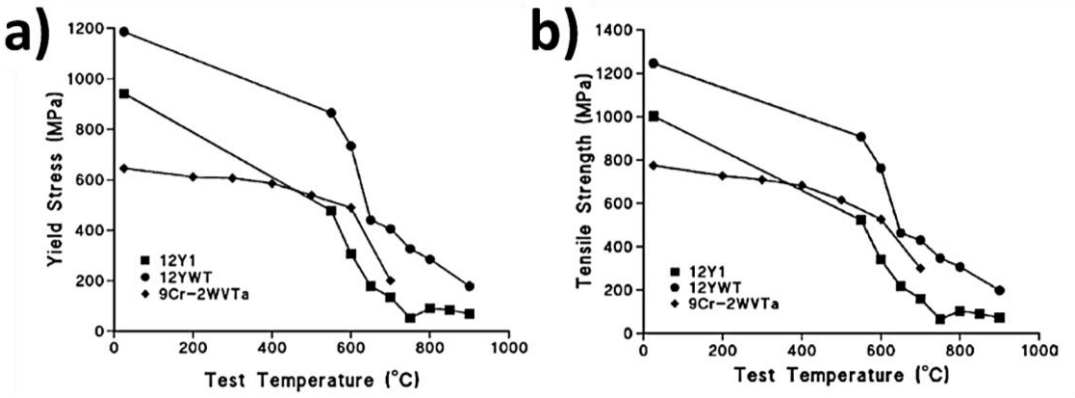

Figure 2.19. Comparison of tensile properties of ODS steels 12Y1 and 12YWT with the non-ODS, reduced-activation steel ORNL 9Cr-2WVTa: a) yield strength, b) tensile strength [133].

Oxide dispersoids act as barriers for dislocation motion and grain growth [4,138,140–143]. In addition, oxide dispersoids are generally incoherent with the matrix, so the strengthening is provided by Orowan looping mechanism [1,2,4,144–

147]. Figure 2.20 shows a representative microstructure showing the interactions between dislocations and NO particles as well as generated dislocation loops [144].

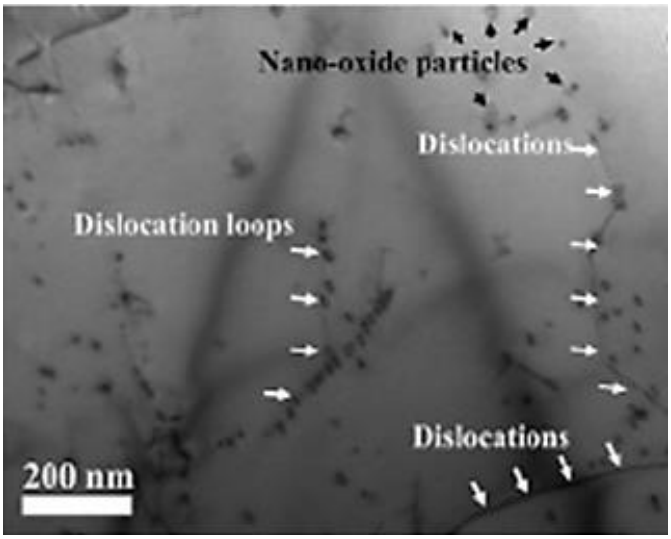

Figure 2.20. BFTEM micrograph of ODS ferritic steel produced by electron beam selective melting method [144].

The production of ODS alloys by conventional methods such as casting and welding is extremely complicated because oxides tend to agglomerate, accumulate, and float at the surface of molten metal due to having nano-size and lower density than the base alloy. Therefore, generally, production of ODS alloys includes MA followed by consolidation/production of the final part and heat treatments [1,2,4,142,148–150]. MA is a deformation-based powder processing method in which a powder mixture is ball-milled using high energies in order to obtain homogenous alloy powders. In the case of ODS alloys, oxide/oxide former powder and base alloy powder mixture is added into the veil to produce ODS alloy powders at the end of the process. During MA process, repeated steps of cold welding and fracturing are applied to the powder mixture as a result of collision of powders and grinding media in an inert environment [1,19,151,152]. Moreover, vacancy formation takes place in MA process due to the high amount of deformation. The existence of vacancies promotes the formation of NO clusters and enhances their stability in the matrix phase [153–156]. As a disadvantage, powder size and sphericity are lost at the end

of the MA process due to the repeated cold welding and fracture steps [136,142]. Figure 2.21 shows the effect of MA process on powder size and shape [142].

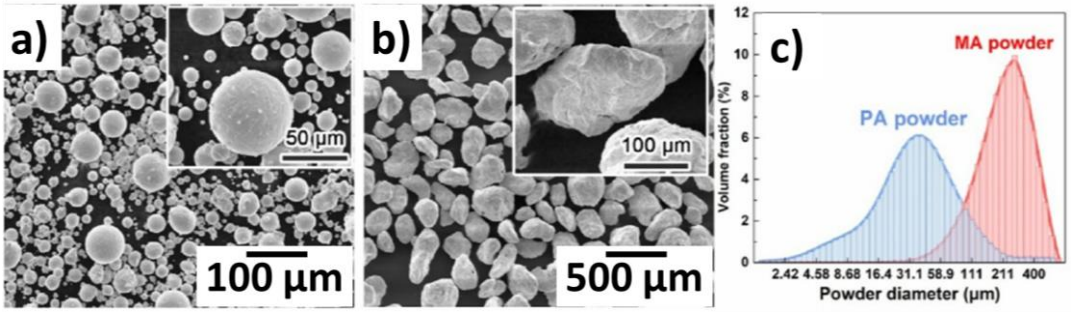

Figure 2.21. SEM micrographs showing the effect of MA process on powder size and morphology: a) pre-alloyed (PA) powder without MA, b) mechanically alloyed (MA) powder after 36 h MA process at 350 rpm with ball to powder ratio 1 [142].

Y-Ti-O oxides are known by their superior structural and morphological stabilities up to ~1100 °C [157–161]. Y-Ti-O oxides generally start to form with a size of several nanometers in the following stoichiometries: $YTiO_3$, Y_2TiO_5, and Y_2TiO_7. Y_2TiO_7 is known as stoichiometric form of Y-Ti-O oxides while the other forms are generally called as nanoclusters or non-stoichiometric forms [162–168]. Moreover, Park et al. [169] studied the effect of oxide size on mechanical properties of ODS Ni-based alloys, and demonstrated that the existence of coarse oxides such as Y-Al-O, and TiO_2, degrades mechanical properties while the existence of smaller-sized Y-Ti-O NOs enhances the mechanical properties of the alloy significantly. Additionally, the dissolution of unstable oxides and the presence of residual Oxygen promote the nucleation of the Y-Ti-O complex oxides in the presence of additional oxygen carriers, such as iron oxides, that have lower stability than Y-Ti-O oxides at elevated temperatures [170–173]. In other studies, on the relation between oxide particle refinement and matrix strengthening, it is observed that the decrease in oxide particle size and particle separation results in the increase in hardness and strength properties of the alloys. It is also observed that Hf is the best for enhancing the strength compared to Ti, Zr, Ca, Al, and Mg [174–181]. Figure 2.22 shows TEM

micrographs showing the effects of Ti, Mg, Zr, Ca, and Hf elements on the oxide particle refinement [174].

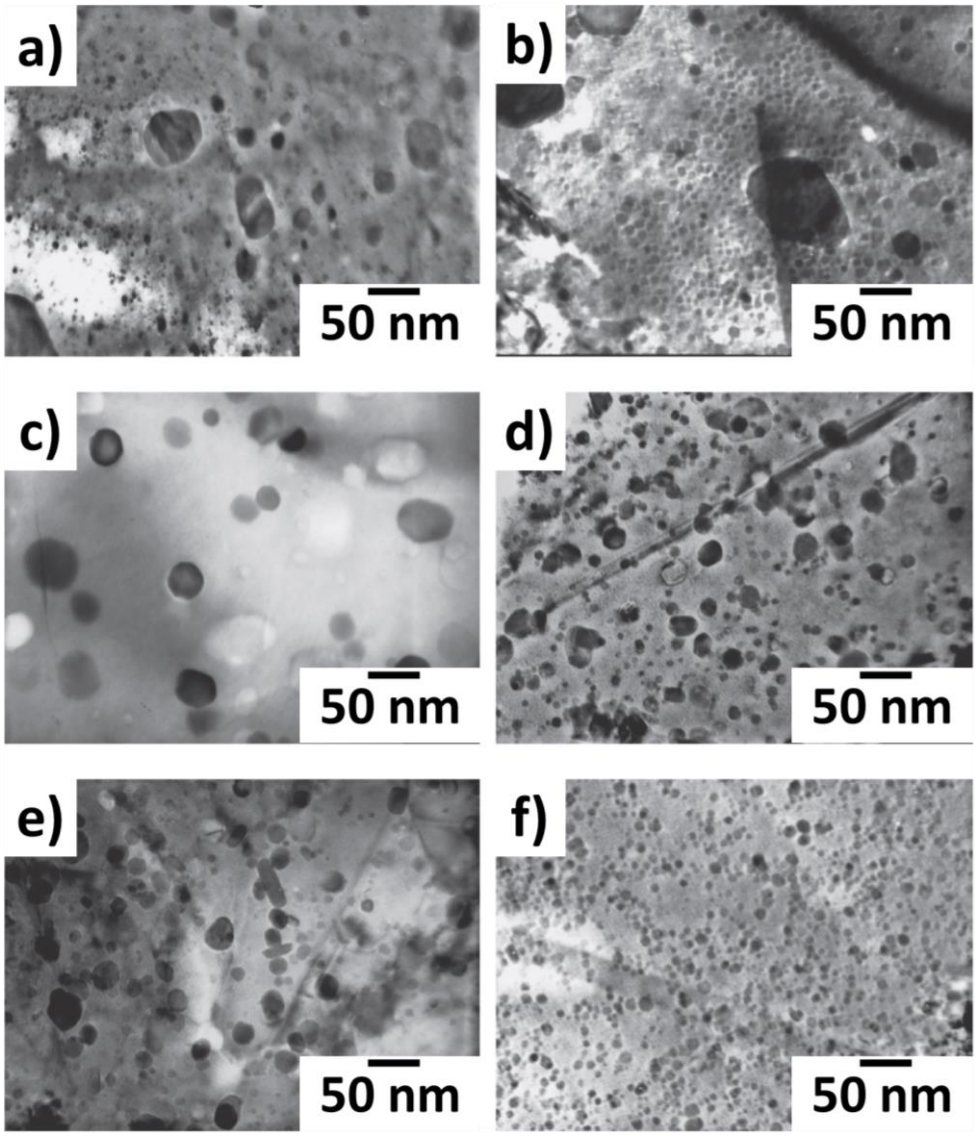

Figure 2.22. TEM micrographs of a) the Ni – 0.5 Al – 1.1 Y_2O_3 with the additions of b) 0.4 wt.% Ti; c) 0.7 wt.% Mg; d) 0.4 wt.% Zr; e) 0.2 wt.% Ca; e) 0.4 wt.% Hf showing NO sizes and morphologies [174].

CHAPTER 3

METHODS AND EXPERIMENTAL PROCEDURE

3.1 Alloy Design

SLM is a process that includes high thermal gradient due to fast heating and cooling cycles. This mechanism results in insufficient time for diffusion for the equilibrium phases to nucleate. As a result, non-equilibrium phases such as Laves, χ, and σ may be observed in the final product [4,115,182,183]. CALPHAD is a method that enables the prediction of phase diagrams on the basis of thermodynamics [184,185] FactSage 8.0 software, one of the thermochemical software that uses CALPHAD method to predict the thermodynamical properties of the alloy systems, [186] was used to determine the equilibrium, non-equilibrium, and Scheil-Gulliver prediction of IN718 alloy upon cooling. Also, the effect of Y, Ti, Hf, Y_2O_3 and FeO addition on the formation of Y-Al-O, Y-Ti-O and Y-Hf-O systems was simulated by the software. For the solidification under equilibrium and non-equilibrium conditions, calculations were conducted using SGTE database. A metastable strengthening phase, γ'', obtained from Mat-Calc open database (Ni-base, mc_ni.tdb) was utilized for non-equilibrium calculations at a fixed temperature [187]. On the other hand, for the prediction of Y-Ti-O and Y-Al-O systems in the microstructure, the ab-initio materials project (AIMP) v4.0 database was used [188]. The Oxygen amount in IN718 powders determined by EA was used to determine the oxide/oxide former type and amount in thermochemical calculations to determine the chemical composition of IN718-Y alloy. Thus, required amounts of Y, Ti, and Y_2O_3 were determined to obtain maximum number density of Y-Ti-O oxides. Then, required amounts of Y_2O_3 and FeO were determined for IN718-YF alloy to increase NO number density in the microstructure. Also, for IN718-YFH alloy, required amounts of Y_2O_3, FeO, and Hf for obtaining the maximum number density of Y-Hf-O oxides

were determined by thermodynamic simulations which were carried out with a CALPHAD-based FactSage 8.0 software.

3.2 Materials

IN718 superalloy, Y_2O_3, FeO, and Hf powders were used as starting materials in this study.

IN718 alloy powders produced by gas atomization technique were purchased from Oerlikon Metco. According to provider, IN718 powders have chemical composition similar to AMS 5662 standard and particle size ranges between 15 and 45 µm [111,189]. SEM micrographs showing the particle size and morphology of IN718 powders are given in Figure 3.1.

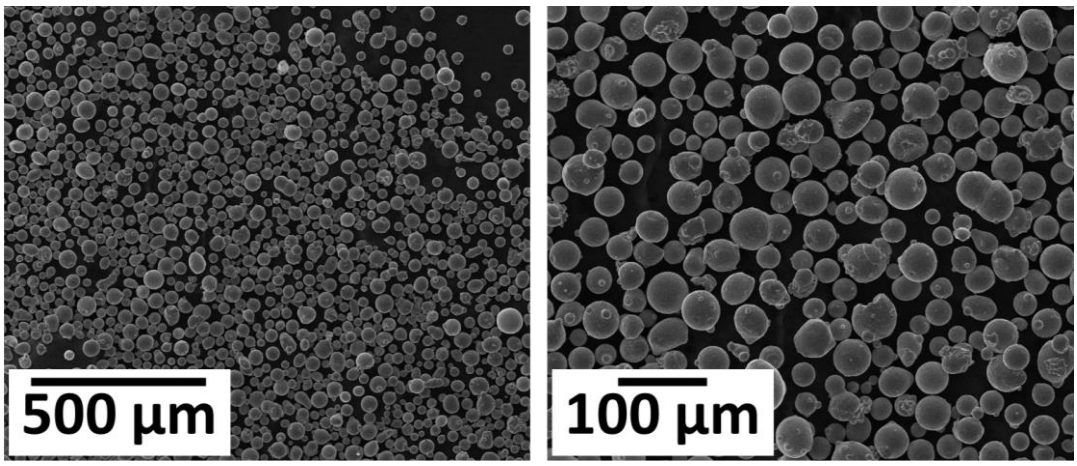

Figure 3.1. SEM micrographs showing particle morphology and size of IN718 powders.

In order to determine the chemical composition of purchased IN718 alloy powders ICP-OES analysis was conducted with Perkin Elmer Optima 4300DV analyzer. Since the oxide type and amount depend on the Oxygen amount in the microstructure [190], elemental analysis (EA) was conducted using LECO ONH 836 analyzer to determine existing Oxygen amount in the alloy powder. Table 3.1 shows the resultant IN718 alloy composition with Oxygen content.

Table 3.1. Chemical composition of IN718 powders including Oxygen content.

Element	Ni	Fe	Cr	Nb	Mo	Ti	Al	Co	Mn	Cu	Si	O
Wt.%	54	18.4	17.3	5	3.1	0.94	0.5	0.036	0.22	0.024	<0.03	0.0162

Y_2O_3, FeO and Hf powders were purchased from Nanografi Nano Teknoloji A.Ş. Y_2O_3 powders had a particle size of 18-38 nm with a purity of 99.99%, FeO powders had a particle size below 1 µm with a purity of 99.9%, and Hf powders had an average particle size of 45 µm with a purity of 99.9%. Figure 3.2 exhibits SEM micrographs showing the morphologies and sizes of afore-mentioned powders.

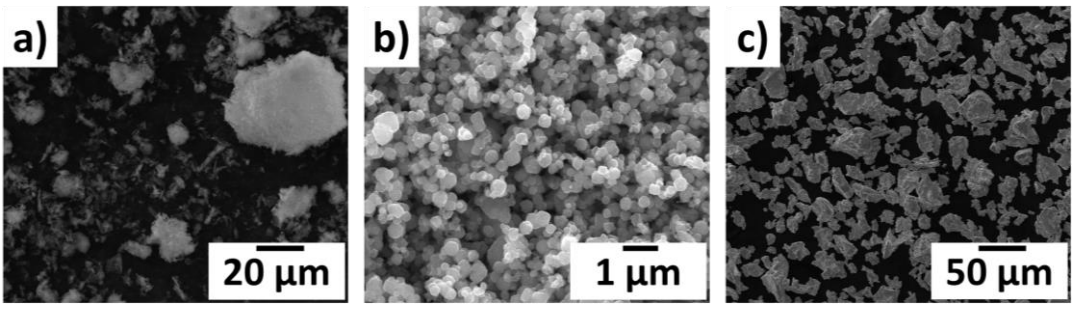

Figure 3.2. SEM micrographs showing particle size and morphologies of a) Y_2O_3, b) FeO, c) Hf powders.

3.3 Mixing Strategy

First, IN718 and oxide/oxide formers of each alloy (IN718-Y, IN718-YF, IN718-YFH) were mixed by using spatula in hardened stainless-steel veil. Then the veil was placed in the Fritsch Pulverisette P6 classic line planetary mono mill high-energy ball milling machine purchased from Fritsch GmbH, Germany. Mixing stage was carried out at 300 rpm speed in Argon environment. The aim was sticking oxide/oxide formers on the surface of IN718 powders without losing morphology and size of the IN718 powders. In order to determine optimum duration for mechanical mixing process, the powder mixtures were mechanically mixed for 2 min, 5 min, 10 min, 20 min, and 30 min. After choosing optimum duration, SLM

production was carried out with the mechanically mixed alloy powders. Figure 3.3 shows the ball mill machine used during the mechanical mixing process.

Figure 3.3. The ball mill machine setup used for mechanical mixing.

3.4 Production of IN718-ODS Alloys with Selective Laser Melting Method

For the production of ODS alloy grades, EOS M290 SLM machine equipped with 400 W Yb-fiber laser and the C-45 base plate was used. During productions, laser spot size, hatch spacing, layer thickness, and rotation angle were kept constant as given in Table 3.2. In order to find optimum SLM process parameters, power (W) and velocity (mm/sec) were chosen as varying parameters. A plate with the dimensions of 20 x 20 x 5 mm^3 was produced for each parameter set of power and velocity under Argon atmosphere.

Table 3.2. SLM process parameters that were kept constant.

Parameter	Value
Laser spot size (µm)	100
Layer thickness (µm)	40
Hatch spacing (µm)	110
Rotation degree (°)	67

For IN718-Y alloy production, a matrix composed of four different power and five different velocity values was created. Corresponding parameter matrix is given in Figure 3.4.

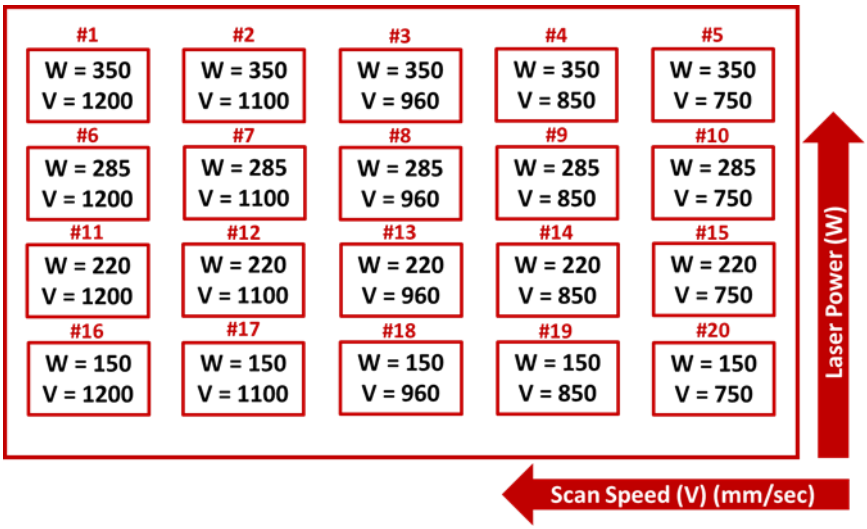

Figure 3.4. Matrix of SLM process parameters for IN718-Y alloy.

According to the power and velocity values that were promising for the final parts that have acceptable densification and hardness properties, three different power and two different velocity values were selected for the productions of IN718-YF and IN718-YFH alloys. The corresponding parameter matrix is given in Figure 3.5.

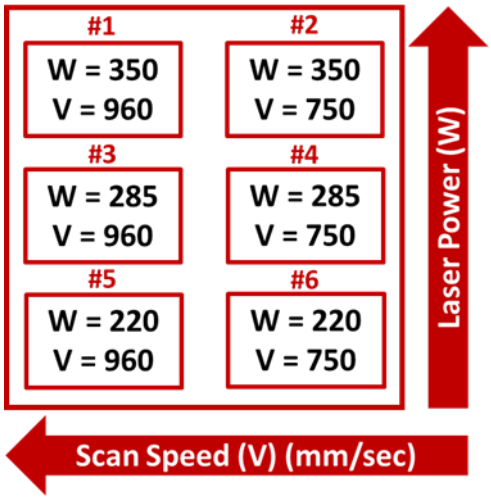

Figure 3.5. Matrix of SLM process parameters for the IN718-YF and IN718-YFH alloys.

After determining the optimum SLM process parameters for all the ODS alloy grades, cylinders having diameters of 10 mm and lengths of 60 mm were produced as shown in the Figure 3.6. The samples were cut from the base plate by EDM cutting that was performed by using Makino U3 and Mitsubishi Electric – Advance Type 3 – MV2400S wire EDM machines.

Figure 3.6. The cylinders produced with optimum process parameters.

3.5 Heat Treatment

In order to promote further oxide formation and to solutionize/homogenize the microstructure [21,116,191,192], five different heat treatment routes were designed for IN718-Y alloy. According to the change in hardness values, the sample that have highest hardness was selected. Then, eight different durations were selected to find the optimum time for the heat treatment. Corresponding heat treatment routes are listed in Table 3.3. Then the optimized heat treatment was applied to IN718-YF and IN718-YFH alloys, too.

Table 3.3. Heat treatment routes.

Heat Treatment	Temperature (°C)	Duration (h)
HT850	850	1
HT1050	1050	1
HT850-1050	850 – 1050	1 – 1
HT1050-650	1050 – 650	1 – 5
HT850-1050-650	850 – 1050 – 650	1 – 1 – 5
HT1050 – 0.5	1050	0.5
HT1050 – 1.5	1050	1.5
HT1050 – 2	1050	2
HT1050 – 2.5	1050	2.5
HT1050 – 3	1050	3
HT1050 – 3.5	1050	3.5
HT1050 – 4	1050	4

The heat treatments were conducted using Lindberg tube furnace in Argon environment followed by furnace cooling. Figure 3.7 shows the tube furnace used

for the heat treatments. The furnace was heated to 1050 °C in 80 min and during the heat treatments, error margin for the furnace temperature was ±13 °C.

Figure 3.7. The tube furnace used for heat treatments.

3.6 Microstructural Characterizations

Samples were cut with Makino U3 wire EDM machine for metallographic preparation to conduct porosity measurements, SEM – phase analyzes, EBSD analyzes and TEM analyzes. Grinding stage was performed by using 60 – 220 – 400 – 800 – 1200 – 2000 grit SiC abrasive papers. After grinding, samples were mechanically polished with diamond pastes consisting of 6 µm and 1 µm diamond particles.

3.6.1 Porosity Measurements with Optical Microscopy

For porosity measurements, OM images of mechanically polished AB samples were taken using Huvitz HDS–5800 digital microscope. At least 5 different OM images at low magnifications were taken. After OM imaging, Image J 1.49 V digital processing software was used for pore analyzes. 5 samples having minimum porosity

were selected for further investigations for IN718-Y alloy and 1 sample was selected for further investigations for IN718-YF and IN718-YFH alloys. Moreover, selected as-polished samples were etched with Kalling's Reagent No.2 (20 ml C_2H_6O – 20 ml HCl – 1 gr $CuCl_2$) for several seconds by immersion technique at RT to obtain the AB SLM microstructures.

3.6.2 Phase Analyzes with Scanning Electron Microscopy

Microstructures of etched AB samples and as-polished HT samples were obtained using FEI Nova Nano SEM 430 microscope equipped with EDAX Pegasus system by using operation parameters of aperture as 6, spot size as 3.5, and 20 kV voltage. The morphology and the size of the micron-sized precipitates were determined from the SEM micrographs. Moreover, chemical compositions of the phases were determined using an EDAX SDD Apollo 10 EDS detector placed in the EDAX Pegasus system. Data collection time for the point EDS analyses was selected as 60 seconds to obtain high peak-to-background ratios. In addition, EDS-mapping was performed using parameters of 1024x1024 resolution, 600 µs dwell time, and 16 frames.

3.6.3 EBSD Analyzes

In order to determine texture, grain structure and phase content after SLM process and heat treatment, EBSD analyzes were conducted. After grinding with 2000 grit SiC abrasive paper, samples were chemically polished by electropolishing technique using Struers TenuPol-5 twin jet electro polisher. Electropolishing was carried out at -40 °C and 11 V using an electrolytic solution of 5 vol.% perchloric acid ($HClO_4$) and 95 vol.% methanol (CH_3OH). After the electropolishing, samples were cleaned with methanol and deionized water. EBSD analyses were conducted on 400 µm x 400 µm area with a step size of 2.2 µm using EDAX Hikari EBSD detector in the EDAX Pegasus system. The other parameters were selected as aperture 5, spot size

5 and 20kV voltage. TSL OIM Data Collection software was used during EBSD data collection and OIM 5.31 software was used to obtain orientation maps, grain boundary maps, KAM maps, and pole figures.

3.6.4 TEM Analyzes

TEM analyzes were accomplished on disk shaped samples having a diameter of 3 mm. To prepare the samples for TEM studies, electropolishing was applied to the disks having a thickness of ~80 µm in the same manner that was explained in Section 3.6.3. JEOL JEM-ARM200CFEG UHR-TEM equipped with EDAX EDS camera as well as FEI Tecnai G2 F20 was used for TEM studies. For EDS analyzes, data collection time was selected as 60 seconds to obtain high peak-to-background ratios.

3.7 Mechanical Tests

3.7.1 Hardness Measurements

Vickers microhardness tests were conducted on as-polished samples using Shimadzu HMV–2 E microhardness tester with a prismatic diamond tip, 1 kg load and 10 sec holding time. At least 20 measurements were taken from different points on the surfaces of each sample.

3.7.2 Tensile Tests

Tensile tests were carried out on AB and HT samples at RT and at 700 °C. First, cylindrical samples that have dimensions of 10 mm in diameter and 60 mm in length along the axis perpendicular to the built direction were machined into the tensile test samples having 8 mm diameter with M8 x 1.25 external thread heads at grips. Then, further machining to 4 mm sub-size cylindrical dog-bone shaped test specimens with the gauge length five times the diameter as suggested by the ASTM E-8m [193] and

ASTM E21-20 [194] standards was applied for each sample. Figure 3.8 and Table 3.4 show the shape and the size of the tensile test samples, respectively.

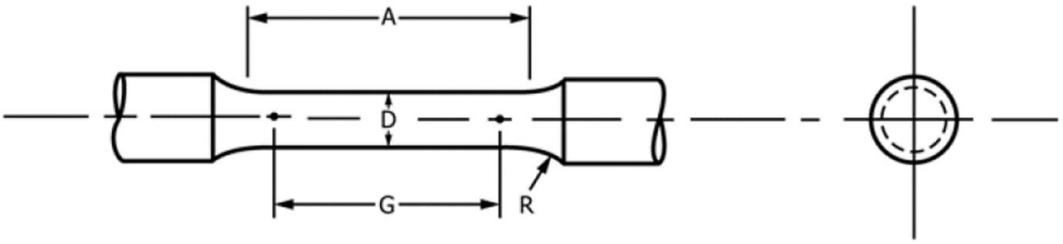

Figure 3.8. Cylindrical tensile test sample as suggested by ASTM E-8m and ASTM E21-20 standards [193,194].

Table 3.4. Dimensions of tensile test samples [193].

Property	**Dimension (mm)**
G (Gauge Length)	20.0 ± 0.1
D (Diameter)	4.0 ± 0.1
R (Radius of Fillet, min)	4
A (Length of Reduced Parallel Section, min)	24

RT tensile tests were performed according to ISO 6892-1 standard [195] whereas elevated temperature tests were performed according to ISO 6892-2 standard [196]. At least two samples were tested for each condition. BESMAK BMT-E series universal testing machine equipped with a high-temperature furnace and rod type extensometer was used for all of the tests of IN718-Y grade. For the other grades, IN718-YF and IN718-YFH, BESMAK BMT-E series universal testing machine with a high-temperature furnace and with rod type extensometer was used for the first two samples while for the third samples of each condition, INSTRON 5582 universal testing machine with a high-temperature furnace and INSTRON 2632-057 extensometer was used to test the reliability of the previous tests. The samples having 25 mm reduced parallel section length were tested with a strain rate of $7x10^{-5}$ up to

yield point where $4x10^{-4}$ strain rate was used between yield and fracture points [195,196].

CHAPTER 4

RESULTS AND DISCUSSION

4.1 Determination of Alloy Compositions and Heat Treatment Temperatures

In order to study the types and fractions of the phases at various temperatures, equilibrium phase diagrams and non-equilibrium cooling diagrams have been obtained as seen in Figure 4.1 (a) and Figure 4.1 (b), respectively. According to equilibrium cooling diagram, a typical RT microstructure of IN718 alloy consists of γ (matrix phase), γ'', σ, γ', α-Cr (Cr-Ni-Fe), and $M_{23}C_6$ type carbides. According to non-equilibrium cooling diagram that shows changes in fractions of different phases during non-equilibrium cooling, the alloy completely solidifies at 800 °C with a solidification sequence of γ, MC carbide, δ, σ, γ', Laves, and χ.

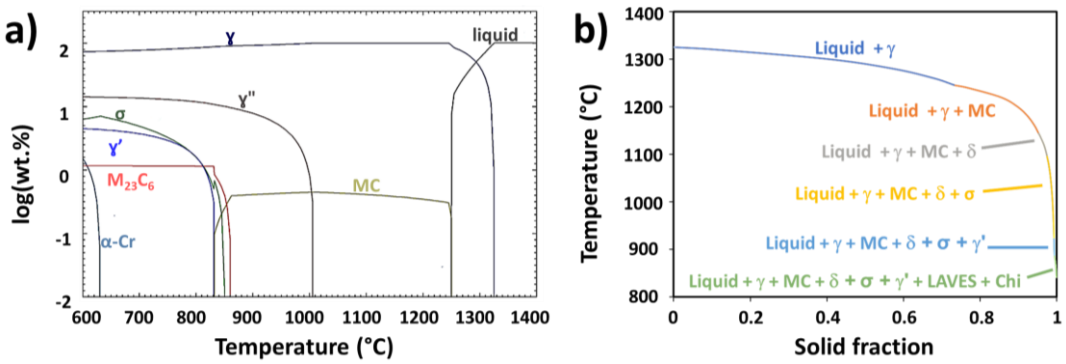

Figure 4.1. a) Equilibrium phase diagram, and b) Solidification path during non-equilibrium (Scheil) cooling of IN718 alloy calculated by CALPHAD method.

4.1.1 IN718-Y Alloy

Having almost no solubility of Y in Iron and Nickel matrices allows Y to promote Y-Ti-O NO formation [197,198]. The composition of IN718-Y alloy was determined based on the maximum amount of Y-Ti-(Al)-O formation. Besides the effect of Y_2O_3, Y, and Ti as well as the temperature on oxide formation was investigated by thermochemical simulations. Figure 4.2 represents related thermochemical simulation results. In Figure 4.2 (a), the effect of Ti amount on the formation of oxides in the microstructure was studied. It can be easily deduced that the addition of Ti has no effect on oxide formation and oxide amounts were kept constant up to 4 wt.% Ti addition. Moreover, increase in Ti amount results in the formation of α-Cr phase which has Cr-Ni-Fe elements. Formation of α-Cr phase indicates the degradation of the matrix phase, which is Ni-Cr-Fe solid solution, and reduction in the strengthening phases γ' and γ''. Therefore, Ti addition has a detrimental effect on both microstructural and mechanical properties. Considering that IN718 has already 0.94 wt.% Ti, addition of extra Ti is unnecessary. Figure 4.2 (b) shows the effect of the addition of oxide/oxide-former, Y_2O_3 or Y, on the Y-Ti-O oxide formation when the total amount of Y and Y_2O_3 was kept constant at ~0.6 wt.%. It was observed that an increase in elemental Y causes not only degradation of Y-Ti-O oxides but also increases the amount of unreacted elemental Y in the microstructure. So, the addition of Y_2O_3 was preferred rather than elemental Y for IN718-Y alloy. Figure 4.2 (c, d) show the thermochemical simulation results conducted at 650 °C (Figure 4.2 (c)) and 850 °C (Figure 4.2 (d)) to obtain the effect of Y_2O_3 addition on the formation of Y-Ti-O oxides. Both the simulation results showed that in order to reach the maximum number density of Y-Ti-O oxides in the matrix, 0.3 wt.% Y_2O_3 should be added to IN718 alloy. It was also observed that compositions and phase fractions are relatively insensitive to temperature except σ, Al_2O_3, and Ti_2O_3 phases. As a result, the composition of IN718-Y alloy was determined as “IN718 – 0.3 wt.% Y_2O_3”.

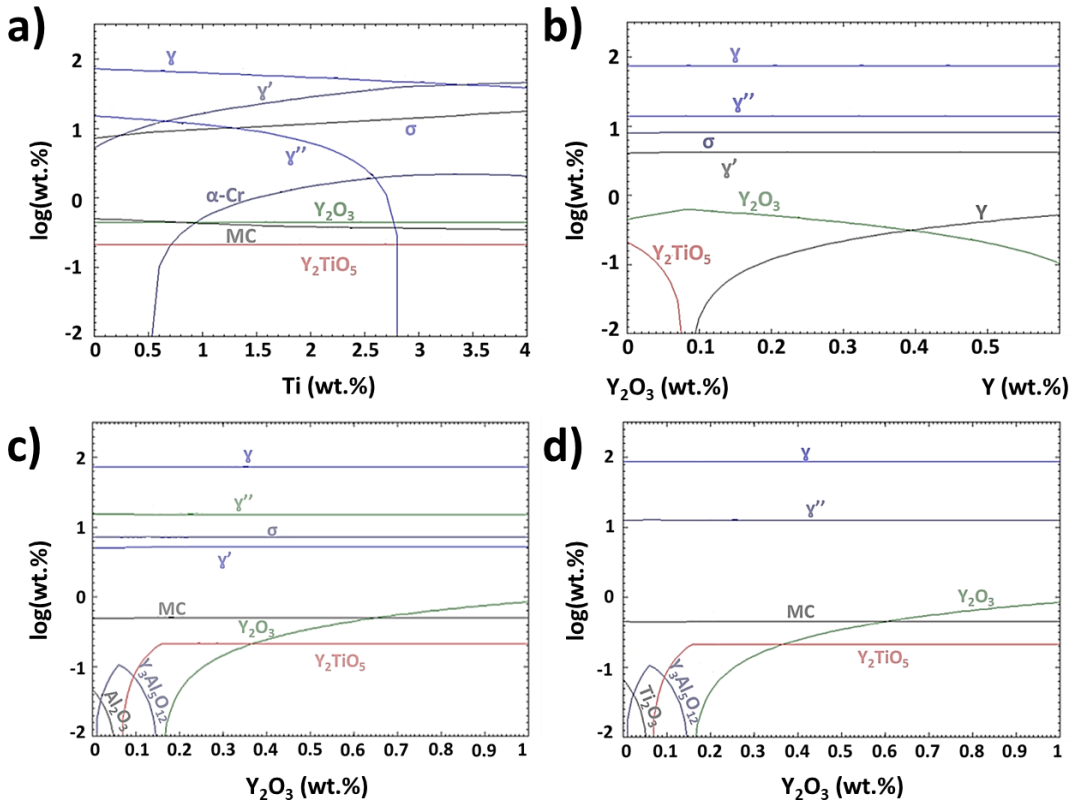

Figure 4.2. Non-equilibrium phase diagrams of IN718 describing the effect of additive oxide/oxide-formers a) Ti, b) Y_2O_3/Y, c) Y_2O_3 at 650 °C, and d) Y_2O_3 at 850 °C.

Figure 4.3 shows the effect of Oxygen amount on the formation of oxides. According to simulation print, increase in Oxygen amount results in formation of Y-Al-O, Al_2O_3, Ti_3O_5, and TiO_2 oxides and increase in their fractions at the expense of Y-Ti-O oxides one of the strengthening phases, γ'. Due to their coarse size and tendency to be coarsen at elevated temperatures, existences of Y-Al-O and Al_2O_3 oxides in the microstructure are undesirable [169,174,175,199]. So, to obtain maximum number density of Y-Ti-O oxides, the Oxygen content should be less than 0.09 wt.% (900 ppm) in the alloy.

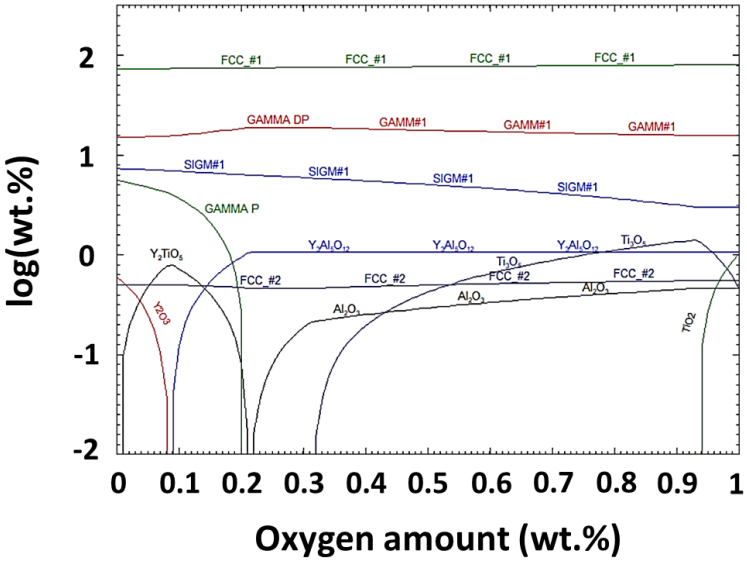

Figure 4.3. Property diagram showing the effect of Oxygen fraction on the oxide formation at 650 °C.

Calculated Scheil cooling diagram and non-equilibrium phase diagram for IN718-Y alloy are given in Figure 4.4. According to Scheil cooling diagram (Figure 4.4 (a)), it is expected that AB microstructure consists of γ matrix phase, Laves phase, δ phase, Y-Ti-O oxides, α-Cr (BCC – Cr-Ni-Fe) phase and some unreacted Y_2O_3. Non-equilibrium phase diagram given in Figure 4.4 (b) predicts the phases forming during heat treatments. Formation of δ phase was suppressed because long-term high-temperature is required for this phase to form in the matrix. Instead, the γ" phase forms due to relatively short-term high-temperature exposure [200–202]. However, it is known that the phases forming towards the end of the solidification might not form which suggests non-existence of γ' and γ" phases in AB condition [119]. According to non-equilibrium phase diagram, γ', γ", σ, α-Cr (Cr-Ni-Fe), and $M_{23}C$ type carbides dissolve in the matrix while γ, M(C,N), Y-Ti-O oxides, and Y_2O_3 phases continue to exist in the microstructure between 950 and 1250 °C which indicates that the heat treatment temperature should be in this temperature range. 850 °C was selected as one of reasonable heat treatment temperatures to dissolve σ and α-Cr (Cr-Ni-Fe) in the matrix phase and anneal existing oxides. At the end of the heat treatment, it is expected to have $M_{23}C_6$ type carbides, M(C,N), γ", Y_2O_3, and Y-

Ti-O oxides in the γ matrix. Second heat treatment temperature was selected as 1050 °C to dissolve all the phases except oxides in the matrix phase in order to obtain only oxide dispersion strengthening effect in the microstructure. 1050 °C heat treatment was also selected to anneal existing oxides. At the end of this heat treatment, it is expected to have M(C,N), Y_2O_3, and Y-Ti-O oxides in the γ matrix. The heat treatment temperature for aging was selected as 650 °C which was conducted after 850 °C and/or 1050°C heat treatments. The aim of aging heat treatment was to maximize number fractions of γ' and γ'' precipitates to obtain whether there is a detrimental effect when oxides and strengthening precipitates coexist in the microstructure or not.

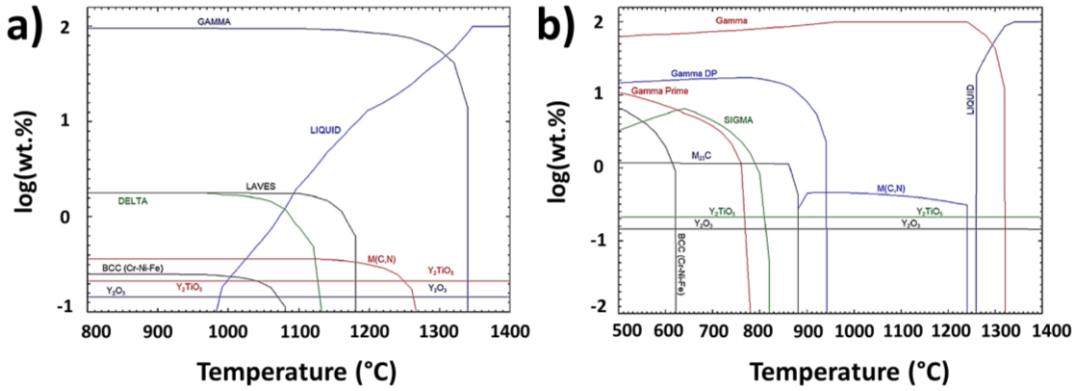

Figure 4.4. a) Scheil cooling diagram of IN718-Y alloy under non-equilibrium conditions, b) Non-equilibrium phase diagram of IN718-Y alloy by suppressing δ phase formation and adding γ''.

4.1.2 IN718-YF Alloy

Figure 4.5 (a) shows the thermochemical simulation results showing the effect of the addition of oxide/oxide-formers, Y_2O_3 and FeO, on the Y-Ti-O oxide formation when the total amount of FeO and Y_2O_3 was kept constant at 1 wt.%. According to the graph, maximum number density of Y-Ti-O oxides are obtained when the composition of FeO and Y_2O_3 is 0.33 wt.% FeO and 0.67 wt.% Y_2O_3. In addition, Y-Al-O and Ti-O oxides start to form with increasing FeO content associated with

decreasing Y_2O_3 content. So, the composition of IN718-YF alloy was determined as "IN718 – 0.67 wt.% Y_2O_3 – 0.33 wt.% FeO". Moreover, according to Scheil cooling diagram (Figure 4.5 (b)), it is expected that AB microstructure consists of γ matrix phase (FCC #1), Laves phase, δ (Ni_3Nb) phase (which is attributed to be γ" phase due to short-term high-temperature exposure), Y-Ti-O oxides, σ (Fe-Cr-(Mo)), χ (CHI_, Fe-Cr-Mo)), γ' (Ni_3Ti), and MC type carbides. As in the case of IN718-Y microstructure in AB condition, γ' and γ" precipitates are not expected in AB microstructure of IN718-YF alloy.

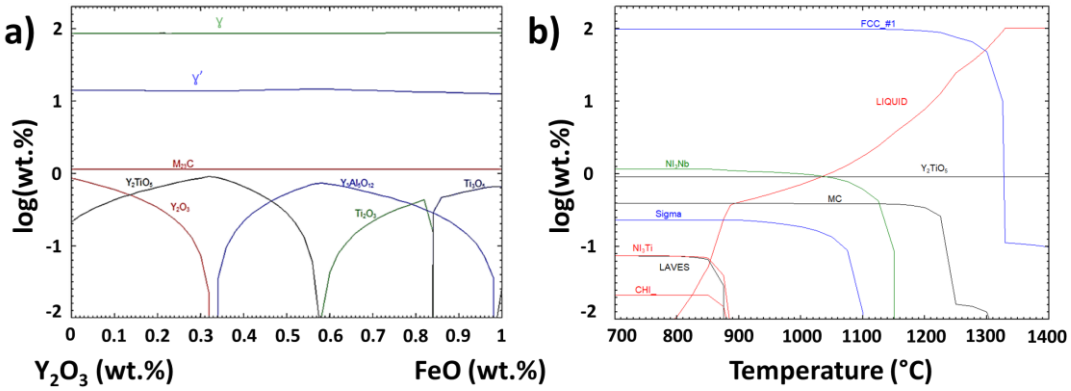

Figure 4.5. a) Property diagram showing the effect of addition of FeO on the oxide formation, b) Scheil cooling diagram of IN718-YF alloy.

4.1.3 IN718-YFH Alloy

Figure 4.6 (a) presents the thermochemical simulation showing the effect of the addition of Hf on the Y-Hf-O oxide formation up to 1 wt.% Hf is addition into IN718-YF alloy. According to the graph, maximum number density of Y-Hf-O oxides are obtained at the expense of Y-Ti-O oxides when more than ~0.55 wt.% Hf is added. Moreover, increase in number density of Y_2O_3 is obtained with increasing Hf content. In addition, increasing Hf content leads MC type carbide (FCC #2) formation and increase of MC carbide amount at the expense of $M_{23}C_6$ type carbides. As mentioned in Section 2.2.1, $M_{23}C_6$ type carbides promote nucleation of TCP phases, such as σ phases due to high coherency between $M_{23}C_6$ and σ phases, and

they form at the expense of MC carbides, which results in a decrease in mechanical properties [2–4,19,33,35]. So, the existence of $M_{23}C_6$ type carbides in the microstructure is not preferred. As a result, the composition of IN718-YFH alloy was determined as "IN718 – 0.67 wt.% Y_2O_3 – 0.33 wt.% FeO – 0.84 wt.% Hf". Moreover, according to Scheil cooling diagram (Figure 4.6 (b)), it is expected that AB microstructure consists of γ matrix phase (FCC #1), Laves phase, δ (Ni_3Nb) phase (which is attributed to be γ'' phase due to short-term high-temperature exposure), Y-Hf-O oxides, σ (Fe-Cr-(Mo)), χ (CHI_, Fe-Cr-Mo)), γ' (Ni_3T), some unreacted Y_2O_3 and MC type carbides. As in the case of IN718-Y and IN718-YF microstructures in AB condition, γ' and γ'' precipitates are not expected to be obtained in AB microstructure of IN718-YFH alloy.

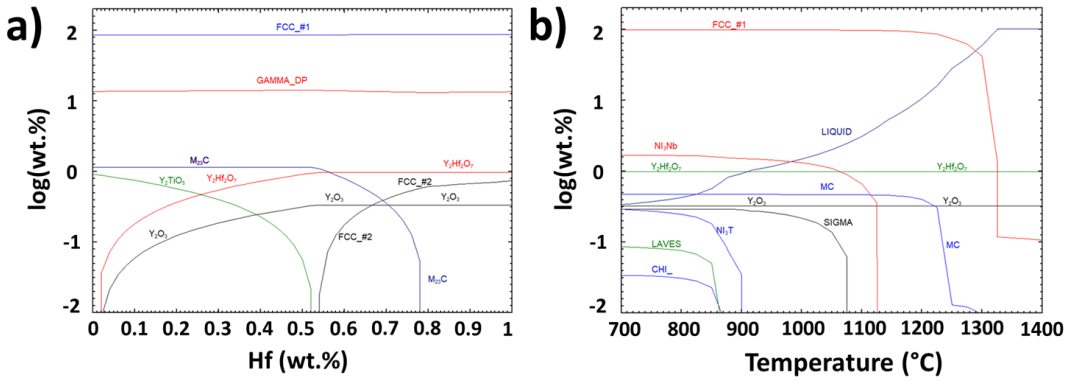

Figure 4.6. a) Property diagram showing the effect of addition of Hf on the oxide formation, b) Scheil cooling diagram of IN718-YFH alloy.

4.2 Mixing Strategy

To avoid size and shape changes of the powders, mixing strategies were selected as hand-mixing and mechanical mixing without grinding balls. The optimization for mixing strategy was carried out on IN718-Y alloy (IN718 – 0.3 wt.% Y_2O_3) powders. Figure 4.7 shows SEM micrographs of hand-mixed and mechanically mixed powders. For hand-mixed powders, it was seen that some of Y_2O_3 powders were simply attached to the IN718 powders while some of Y_2O_3 powders were agglomerated. Thus, mechanical bonding between Y_2O_3 and IN718 was not achieved

when powders were mixed by hand-mixing. In cases of mechanical mixing for 2 min and 5 min, no mechanical bonding between Y_2O_3 and IN718 powders were detected. On the other hand, Y_2O_3 powders that are stuck on the IN718 powders started to lose their shape after mechanical mixing for 10, 20, and 30 mins. The changes in their shapes after 10 min mechanical mixing indicates that there exists mechanical bonding between Y_2O_3 and IN718 powders.

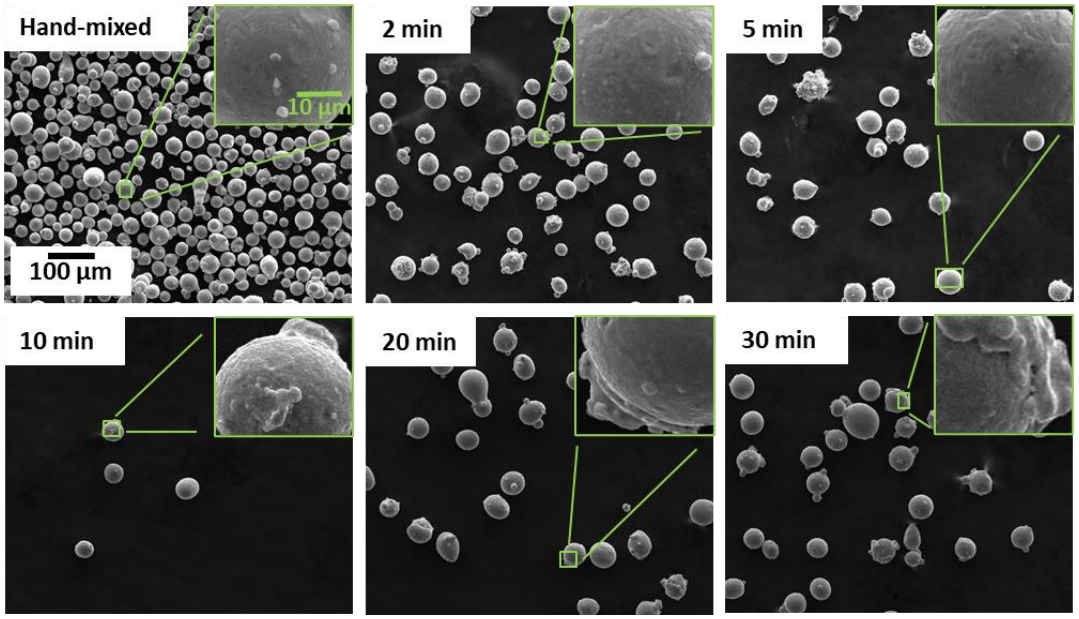

Figure 4.7. SEM micrographs showing powder shapes and sizes of hand-mixed and mechanically mixed IN718-Y alloy powders.

Particle size of IN718 powders was between 15 and 45 µm with an average particle size close to upper bound. As mechanical bonding between oxides and IN718 powders was provided with almost no change in powder shapes, the last criterion was to maintain particle size similar to IN718 powders provided by the supplier. Figure 4.8 represents average particle size analyzes of hand-mixed and mechanically mixed powders. In hand-mixed condition, a decrease in the particle size was detected. The reason of this behavior was the existence of unattached but agglomerated Y_2O_3 powders having smaller average particle sizes than IN718 powders. After 20 min of mechanical mixing, an increase in average particle size was observed. The increase of average particle size was related to agglomeration of

smaller particles on IN718 powder surfaces which resulted in losing spherical shape. On the other hand, it was observed that average particle size was kept close to IN718 powders' sizes for mechanical mixing between 2 and 10 min. A slight deviation was obtained in average particle sizes in case of mechanical mixing for 5 min. According to SEM micrographs given in Figure 4.7, no mechanical bonding was observed for mechanical mixing for 2 min and 5 min. So, 10 min was selected as ideal mechanical mixing time for IN718-Y alloy. The same procedure was applied to IN718-YF and IN718-YFH alloys.

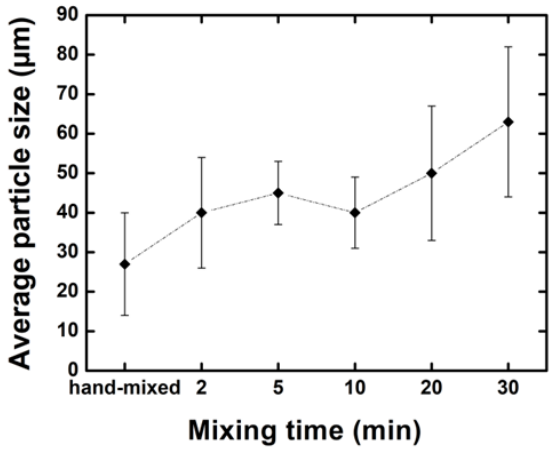

Figure 4.8. Change in average particle size of IN718-Y alloy powders with respect to mixing time.

Figure 4.9 shows SEM micrographs of mechanically mixed IN718-Y, IN718-YF, and IN718-YFH alloy powders. It was observed that mechanical bonding was attained for all the grades. Therefore, the mechanically mixed powders were ready for the SLM productions.

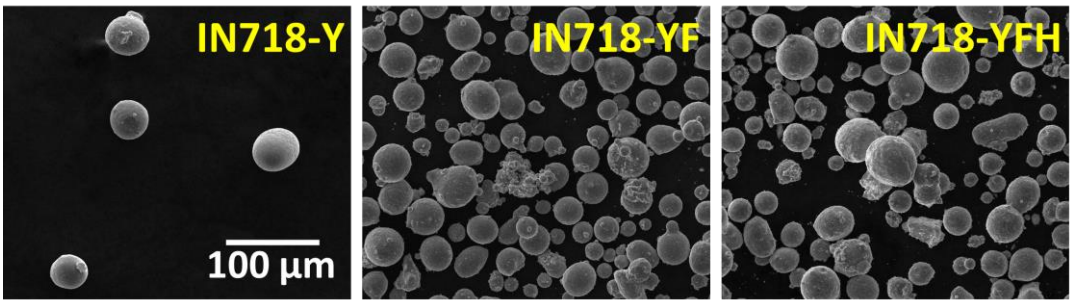

Figure 4.9. SEM micrographs of mechanically mixed IN718-Y, IN718-YF, and IN718-YFH alloy powders just before SLM productions.

4.3 Parameter Optimizations for Selective Laser Melting

20 samples for IN718-Y alloy were produced by the SLM method with various power and velocity parameters given in Figure 3.4. Figure 4.10 shows the OM images of AB IN718-Y samples in as-polished condition. It was observed that power has a predominant role in densification rather than velocity. At high powers, pore sizes and amounts remain similar with the increasing velocity, while, at low powers, pore sizes and amounts increase drastically with increasing velocity. When low power is combined with high velocity values, the time for obtaining a homogeneous melt pool could not be provided and some powders remain unmolten. In other words, energy density is not enough to obtain homogeneous melt pools. On the other hand, high powers combined with low velocities causes keyhole porosity formation due to turbulent flow as a result of dendrite formation and pore growth [95,203,204]. The samples produced with the lowest power (150 W) exhibited an extensive amount of porosity. Similarly, high scan speeds (1100 mm/s and 1200 mm/s) caused increase in amount of porosity even at high powers.

Figure 4.11 shows the porosity of IN718-Y alloy samples produced with different power and velocity parameters. As observed from OM images, use of low powers caused large amounts of porosity values up to ~7% of the total area. On the other hand, use of high power combined with low velocity values resulted in porosity amounts much less than 1% of the total area.

Additionally, hardness measurements were conducted and compared with the hardness values of IN718 produced by standard parameters (285 W, 960 mm/s) [21,205]. Among the samples that have least porosity amounts, sample #13 (220 W-960 mm/s, 318 ±7 HV) had the highest hardness which is close the hardness of the standard IN718 sample (~300 HV). Figure 4.12 represents the measured hardness values of AB samples.

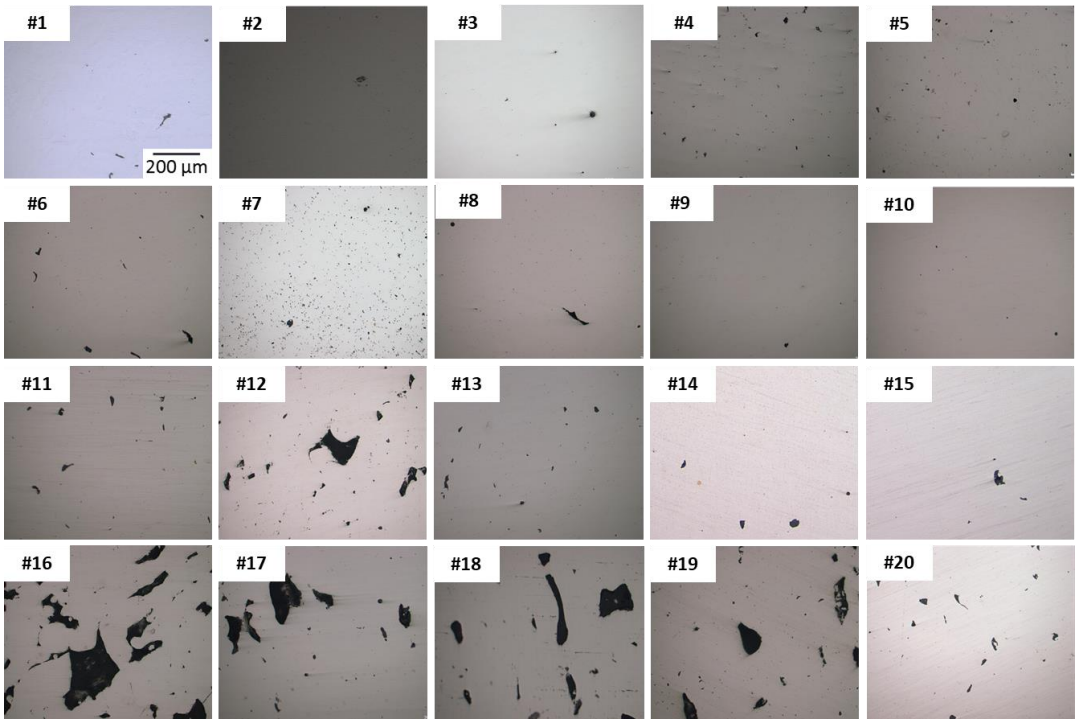

Figure 4.10. OM images of AB IN718-Y alloy samples in as-polished condition after SLM manufacturing with various parameters given in Figure 3.4.

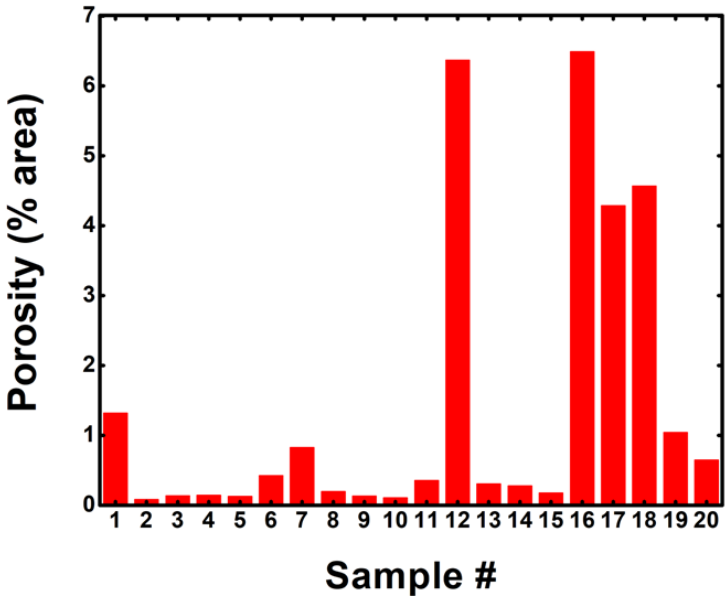

Figure 4.11. Porosity amounts of AB IN718-Y alloy after SLM manufacturing with various power and velocity parameters given in Figure 3.4.

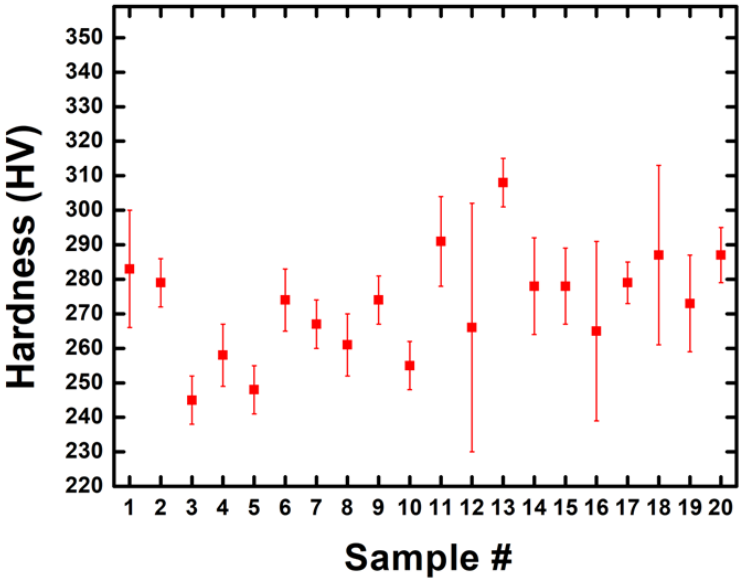

Figure 4.12. Hardness values of AB IN718-Y alloy after SLM manufacturing with various parameters given in Figure 3.4.

Besides sample #13, four different samples were selected for further microstructural analyzes. The selected samples were #3 which was produced with the same velocity value but with highest power value, #8 which was produced by standard parameters

for IN718 alloy, #10 which had one of the lowest porosities, and #15 which was produced with the same power value but with the lowest velocity. Table 4.1 shows porosity and hardness values of the selected samples.

Table 4.1. Porosity and hardness values of the selected IN718-Y samples for SLM process parameter optimization.

Sample #	Porosity (% Area)	Hardness (HV)
3	0.1	245 ± 7
8	0.2	261 ± 9
10	0.1	255 ± 7
13	0.3	308 ± 7
15	0.2	278 ± 11

Figure 4.13 shows OM images of the standard IN718 sample and the selected IN718-Y samples in etched condition. According to OM images, melt pools were in the well-defined manner and there were no significant differences in the OM microstructures at low magnifications. The OM image of sample #3 showing the existence of a long crack path is given in Figure 4.14. So, the parameters used for #3 sample were inappropriate for the SLM production of IN718-Y alloy. To carry out phase analyses of samples #8, #10, #13, and #15, the samples were examined under SEM. Figure 4.14 exhibits corresponding SEM images of other selected samples. Carbides with irregular shapes and sizes of ~50 μm were detected in the microstructures of #8 and #10 samples. As carbides have blocky shapes and large sizes, they are expected to act as stress concentrators and crack initiation points which degrades mechanical properties of the alloy. Moreover, existence of microcracks/micropores were detected in the microstructure of sample #15. It is known that existences of cracks are avoided due to their detrimental characteristics for mechanical properties [206]. Thus, the parameters used for the production of

sample #8, #10, and #15 were found to be unsuitable. In the microstructure of sample #13, Y-Ti-Al-O oxides having irregular shapes and sizes up to ~50 µm and carbides with sizes of ~2-3 µm were detected. Besides, there is no crack observed. Except the large-sized and complex-shaped oxides, sample #13 satisfies optimum characteristics for SLM production. Therefore, the best SLM process parameters were selected as 220 W and 960 mm/s for IN718-Y alloy. Sample #13 will be considered as IN718-Y from now on.

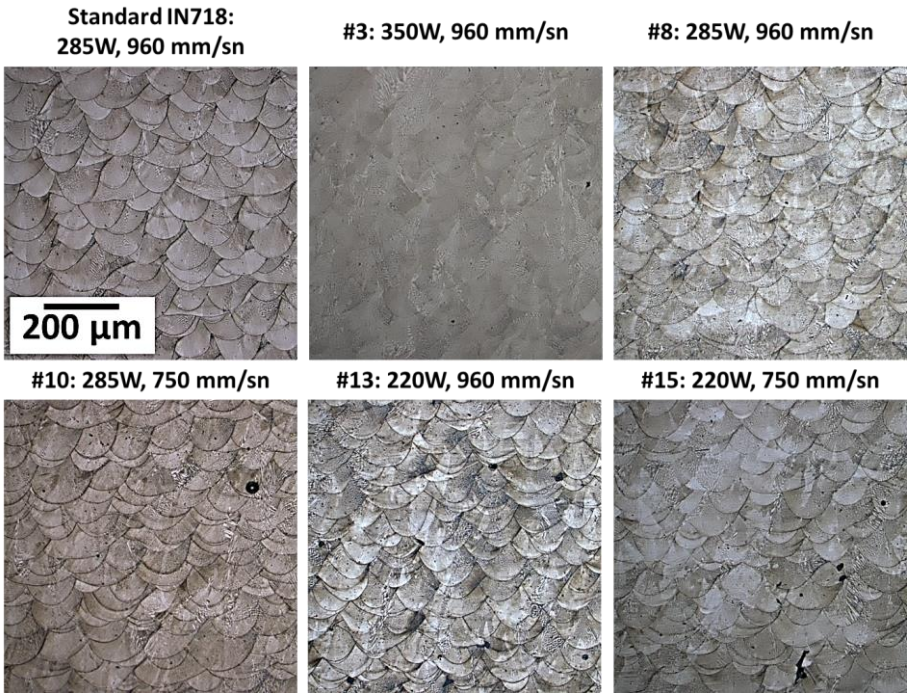

Figure 4.13. OM images of standard IN718 sample and selected IN718-Y alloy samples (#3, #8, #10, #13, and #15) for further examinations.

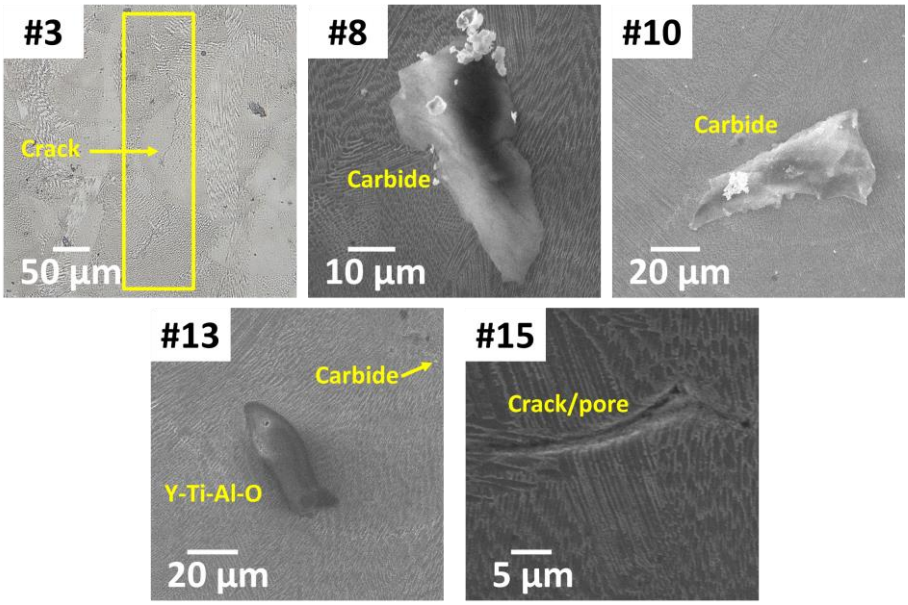

Figure 4.14. SEM micrographs showing defects and phases in the microstructures of selected IN718-Y alloy samples.

Three different power and two different velocity values were selected (given in Figure 3.5) for SLM parameter optimization for IN718-YF and IN718-YFH alloys. The parameters were selected based on the analyzes carried out for the optimization of SLM parameters for IN718-Y alloy. Below 220 W power, lack of fusion porosities were obtained in IN718-Y alloy, so lower power values were subtracted from the production matrix. In addition, to provide enough time for obtaining homogeneous melt pools, velocity values higher than 960 mm/s were also subtracted from the production matrix. Figure 4.15 shows the OM images of AB IN718-YF and IN718-YFH samples in as-polished condition. Similar to parameter optimization carried out for IN718-Y alloy, power has a predominant role in densification rather than velocity. At high powers, pore sizes and amounts remain similar with the increasing velocity, while, at low powers, pore sizes and amounts increase drastically with increasing velocity. Moreover, high powers combined with high velocity (960 mm/s), increase the porosity. As inferred from OM images, the parameter set used for the production of sample #2 of both IN718-YF and IN718-YFH alloy resulted in lowest porosities, in other words, highest densifications. The porosity and hardness

measurements for IN718-YF and IN718-YFH alloy samples given in Figure 4.16 confirmed that sample #2 of both the alloys had highest hardness and lowest porosity. As a result, the best SLM process parameters were selected as 350 W and 750 mm/s for IN718-YF and IN718-YFH alloys. #5 samples will be considered as IN718-YF and IN718-YFH from now on.

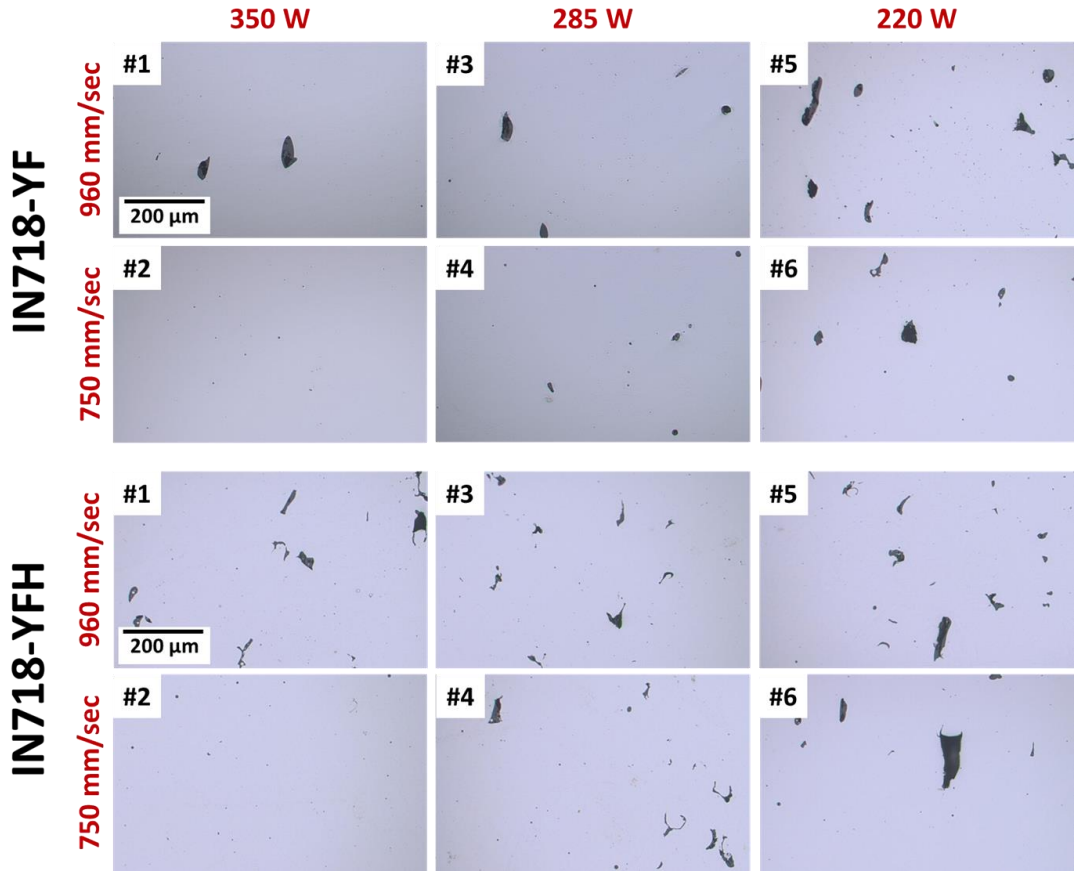

Figure 4.15. OM images of AB IN718-YF and IN718-YFH alloy samples in as-polished condition after SLM manufacturing with various parameters given in Figure 3.5.

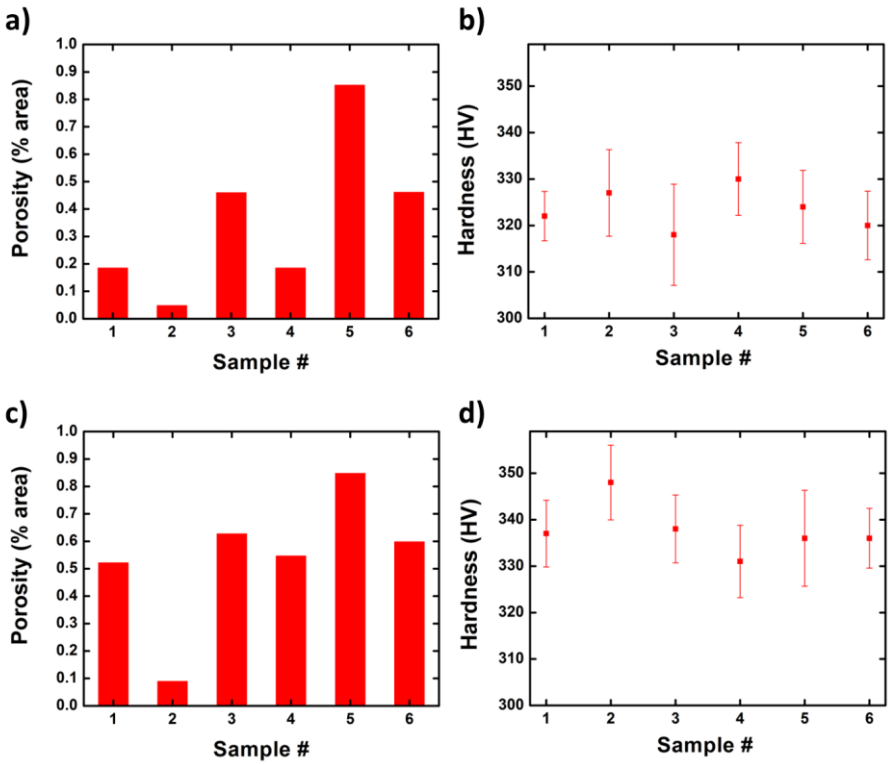

Figure 4.16. Porosity values of AB a) IN718-YF, c) IN718-YFH; and hardness values of b) IN718-YF, d) IN718-YFH after SLM manufacturing with various parameters given in Figure 3.5.

4.4 Parameter Optimizations for Heat Treatment

As the first step, in order to decide the optimum heat treatment procedure, five different heat treatment routes were designed, given in Table 3.3, and applied to the IN718-Y alloy. Figure 4.17 shows the corresponding hardness values of IN718-Y samples after heat treatment. Considering the calculated non-equilibrium phase diagram given in Figure 4.4 (b), the aim of HT850 heat treatment was to dissolve σ and α-Cr phases in the matrix phase while keeping the strengthening phases of γ' and γ''. At the end of the heat treatment, thermochemical simulations suggested to obtain γ', γ'', $M_{23}C$, M(C,N), Y_2O_3, and Y-Ti-O oxides in the γ matrix. On the other hand, the aim of HT1050 heat treatment was to dissolve all of the phases except oxides and M(C,N) in the matrix phase. So, thermochemical calculations suggest that the

resultant microstructure consists of γ matrix, M(C,N), Y_2O_3, and Y-Ti-O oxides. Hardness measurement revealed that HT850 sample had lower hardness value than HT1050 sample. So, it can be inferred that existence of $M_{23}C_6$ type carbides had negative effect on the hardness of IN718-Y alloy. Moreover, applying heat treatment at 1050 °C may contribute to the annealing of existing oxide particles into more stoichiometric forms which improve the hardness of the IN718-Y alloy [207]. When HT850-1050 heat treatment was applied, hardness was not improved as much as in HT1050 heat treatment. So, applying a heat treatment at 850 °C followed by 1050 °C identified as an ineffective method. Also, the fact that the hardness was not improved as much as HT1050 heat treatment showed that HT850 heat treatment is unnecessary. When HT1050-650 and HT850-1050-650 heat treatments are compared, it was seen that no contributions of the heat treatment step at 850 °C were detected. The heat treatment at 650 °C as a final step promoted the formation of γ' and γ'' precipitates which increases the hardness considerably. However, this work focuses on the formation and maximization of NOs rather than γ' and γ'' precipitates. Therefore, the optimum heat treatment was selected as HT1050 to study of the effect of NOs formed in the microstructure.

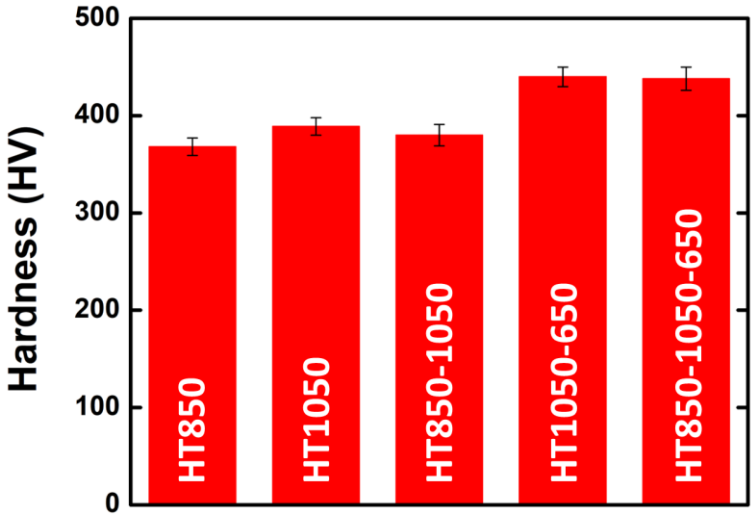

Figure 4.17. Comparison of hardness values of HT IN718-Y samples.

As the second step, HT1050 heat treatment was applied to IN718-Y samples between 0.5 and 4h durations with 0.5h intervals. Figure 4.18 presents the resultant hardness

values obtained after the heat treatments. HT1050 – 0.5, HT1050 – 1.5, HT1050 – 3.5, HT1050 – 4 samples had slightly higher hardness compared to the others. Huang et al. [101] developed a model that represents the relation between temperature and the time required to dissolve Laves phase completely in the microstructure in their study on heat treatment of IN718 produced by SLM. According to their model, the minimum time required to dissolve Laves phase completely in the microstructure can be found by the following formula:

$$t = \frac{1}{3266} exp \frac{21642}{T}$$

where t: minimum required time (sec), and T: temperature (K). When this model was applied to IN718-Y alloy system, the minimum required time was found as 65 min to dissolve Laves phase completely in the microstructure. So, HT1050 – 0.5 heat treatment was not long enough to dissolve Laves phase. When the microstructure of HT1050 – 1.5 sample was investigated, intergranular precipitations of second phase particles were observed. These particles were identified as carbides and Laves phases. Figure 4.19 represents the SEM micrographs showing intergranular segregation and carbide phase with its chemical composition.

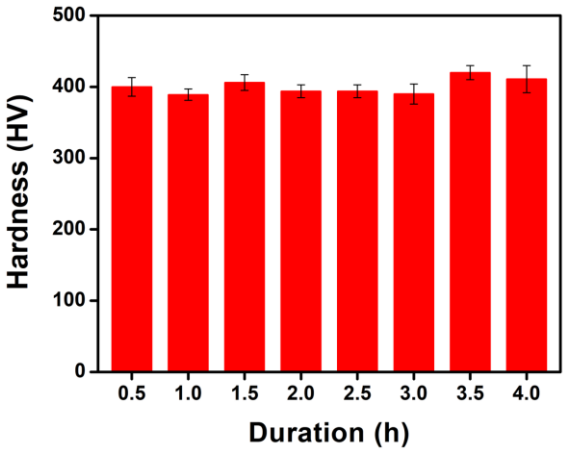

Figure 4.18. Comparison of hardness values of HT IN718-Y samples for different durations.

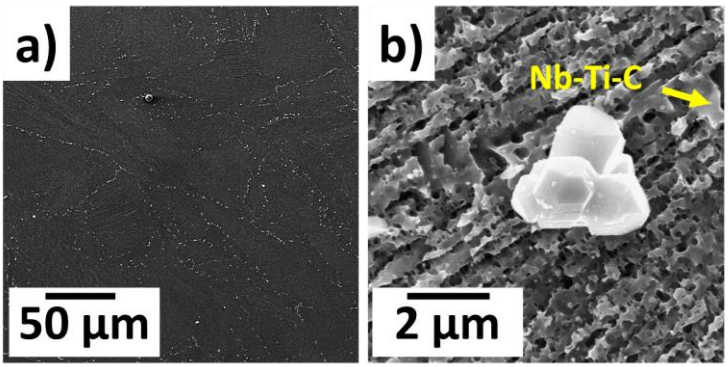

Element	Wt.%
Nb	11.32
Ti	63.72
C	1.98

Figure 4.19. SEM micrograph of HT1050 – 1.5 sample showing a) grain boundary segregation, b) carbide phase with its chemical composition.

Figure 4.20 exhibits EDS maps of secondary particles in the microstructure of the HT1050 – 1.5 sample. The maps given in Figure 4.20 (a) indicate existence of irregular-shaped Nb-Ti-(Mo) particles in the matrix. These Nb-Ti-(Mo) particles are Laves phases. The maps given in Figure 4.20 (b) were obtained from a grain boundary area. The EDS mapping suggests segregation of needle-like and irregular-shaped Nb-Mo-(Ti) particles along the grain boundary. Similar to the other studies, these particles were determined to be Laves phases [58,61,208]. Therefore, 1.5 h was determined to be such a long time that causes intergranular segregation of detrimental phases.

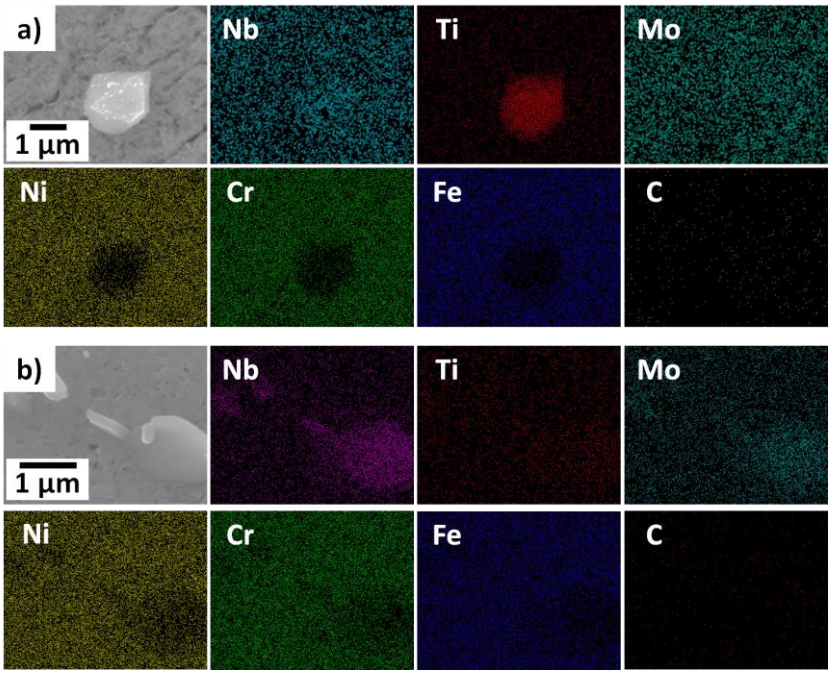

Figure 4.20. EDS map results of particles observed in the microstructure of the HT1050 – 1.5 sample.

Figure 4.21 represents the SEM micrographs showing intergranular segregations in HT1050 – 3.5h sample. It was observed that most of the segregates had needle-like morphology which results in acting as stress concentrators and/or crack initiation sites.

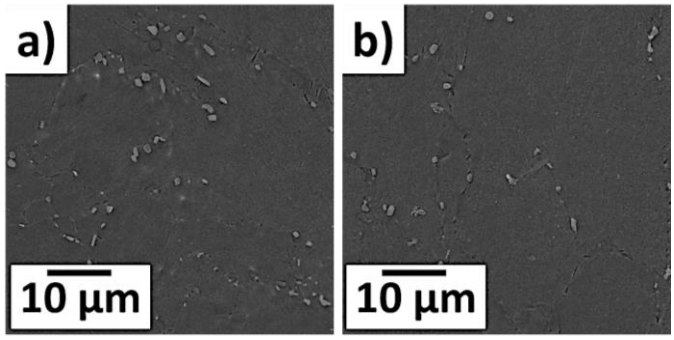

Figure 4.21. SEM micrographs of HT1050 – 3.5 samples showing precipitate size and morphology.

Figure 4.22 exhibits EDS maps showing the elemental content of the precipitates. The elemental maps given in Figure 4.22 (a) indicate the existence of Nb-Mo-(Ti)

Laves phases while the maps given in Figure 4.22 (b) indicate the existence of Nb-Mo-(Ti) Laves phases and Al-O oxides. Laves phase was obtained in both irregular and needle-like morphologies while oxide particle was obtained in irregular shape. Also, Al-O oxides have tendency to coarsening at elevated temperatures, meaning that the existence of this phase affects high-temperature mechanical properties in a negative manner [169,174,175,177,178,199,209]. Therefore, 3.5 h was determined to be extensively long time that causes enhanced segregations of detrimental phases such as Laves and Al-O oxides. The microstructural examination of the HT1050 – 4 was not carried out because the time elapsed during heat treatment was already longer than 3.5h.

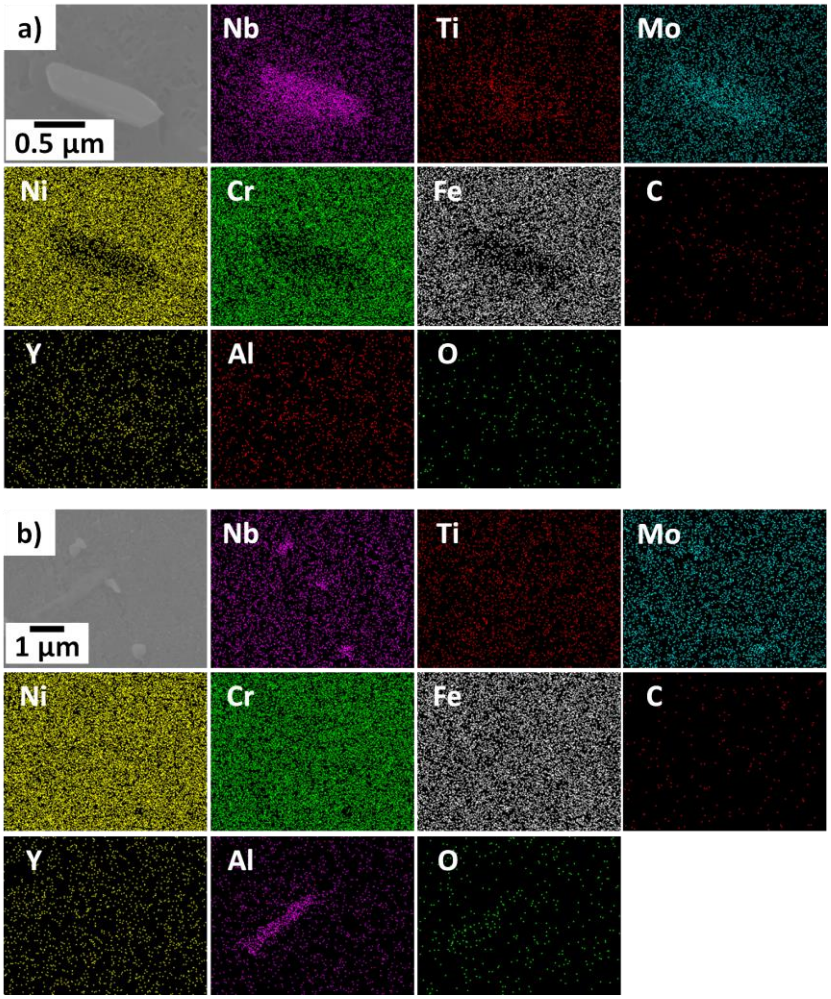

Figure 4.22. EDS map results of particles observed in the microstructure of the HT1050 – 3.5 sample.

Figure 4.23 shows SEM images (Figure 4.23 (a-c)) of the HT1050 sample and corresponding EDS analysis of a spherical particle shown in Figure 4.23 (c). Figure 4.23 (a) indicates the existence of sub-micron and nano-sized particles while the onset of segregation is observed in Figure 4.23 (b). It is clearly seen that most of the particles had spherical morphology, so they are expected to contribute to strengthening. Figure 4.23 (c) reveals the existence of micron-sized oxides with a spherical morphology in the microstructure. According to EDS analysis, these oxides were Y-Ti-Al-O oxides. Compared with HT1050 – 0.5, HT1050 – 1.5, HT1050 – 3.5, and HT1050 – 4, HT1050 was obtained to be an optimum heat treatment for IN718-Y alloy. The same heat treatment (HT1050 – 1h) was applied to IN718-YF and IN718-YFH alloys.

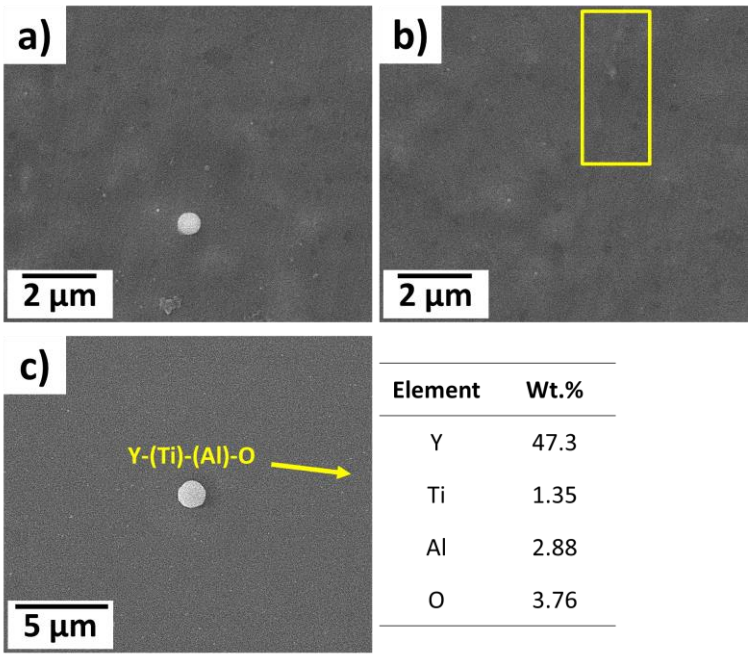

Element	Wt.%
Y	47.3
Ti	1.35
Al	2.88
O	3.76

Figure 4.23. SEM micrograph of HT1050 sample showing a) sub-micron precipitates, b) the onset of the segregation, c) micron-sized precipitate with its chemical composition.

4.5 Microstructures and Mechanical Properties in As-built Condition

Figure 4.24 shows SEM micrographs of IN718-Y, IN718-YF, and IN718-YFH alloys in AB condition taken at a low magnification (Figure 4.24 (a-c)) and at a high magnification (Figure 4.24 (d-f)). According to SEM micrographs, AB microstructures consist of fine cells having sizes below 1 μm at different orientations located within well-defined melt pools. The formation of the cell structure is generally related with high thermal gradients up to 10^6 K/s that a part experiences during SLM processing. Rapid heating and rapid cooling cycles result in dendritic microstructure with Laves phase segregations in inter-dendritic regions due to lack of time for diffusion [6,81,99]. Figure 4.25 shows EBSD orientation maps of AB alloys. Orientation maps indicate that IN718-Y alloy shows a slight preferred orientation along (001) plane while such a behavior is not observed for IN718-YF and IN718-YFH alloys. For further texture analysis, pole figures were obtained for (001), (011), and (111) planes. Related pole figures are given in Figure 4.26. The MUD (multiple of uniform density) number given on the color scales of the pole figures is a measure of texture strength, high values indicating a strong alignment. In the literature studies, the samples are considered to have a texture when the MUD number exceeds ~8 with a specific pattern/distribution is obtained along that direction [210–212]. According to the given information, none of the alloys have shown specific pattern on the related pole figures and the maximum MUD number was measured as ~6. Therefore, no obvious preferred orientation was detected for all the AB alloys. Moreover, no preferentially oriented texture was observed for IN718-Y, AB IN718-YF and IN718-YFH alloys. All the AB alloys have shown random texture with almost no preferred orientation.

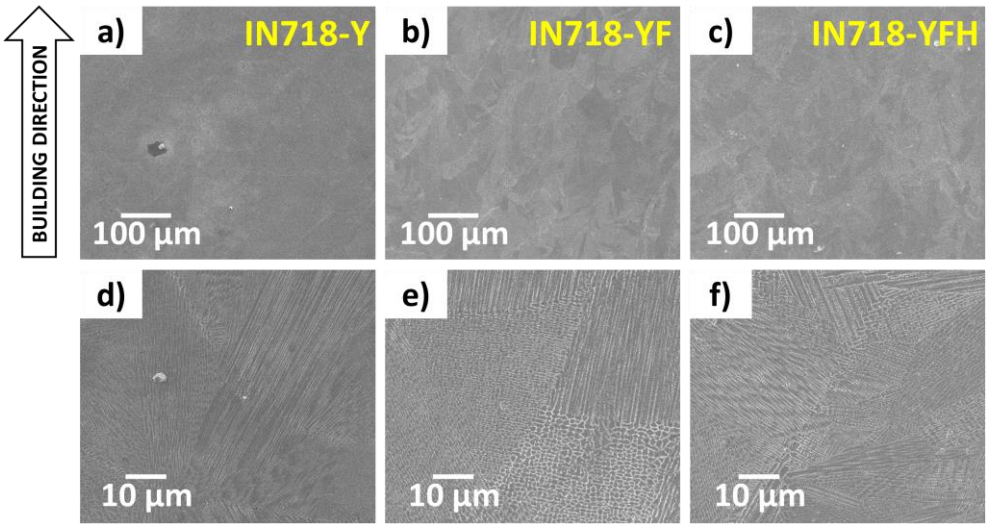

Figure 4.24. SEM micrographs of AB microstructures: (a,d) IN718-Y, (b,e) IN718-YF, (c,f) IN718-YFH.

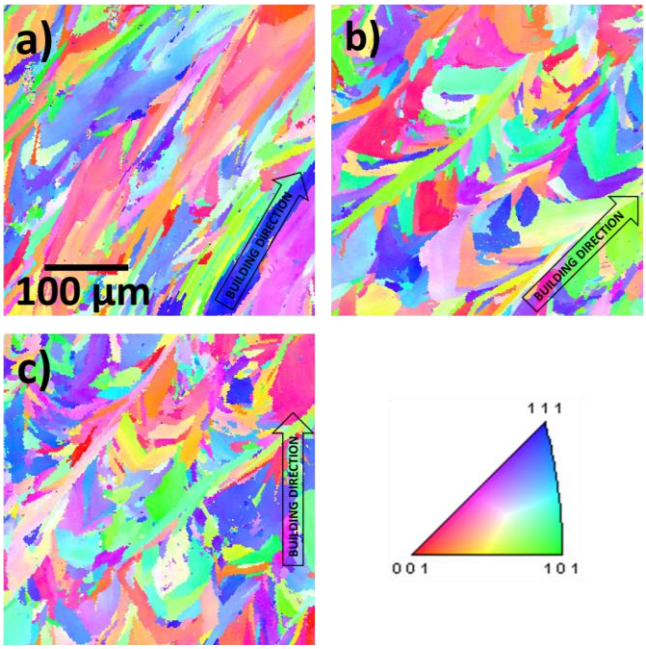

Figure 4.25. EBSD orientation maps of AB a) IN718-Y, b) IN718-YF, c) IN718-YFH alloys.

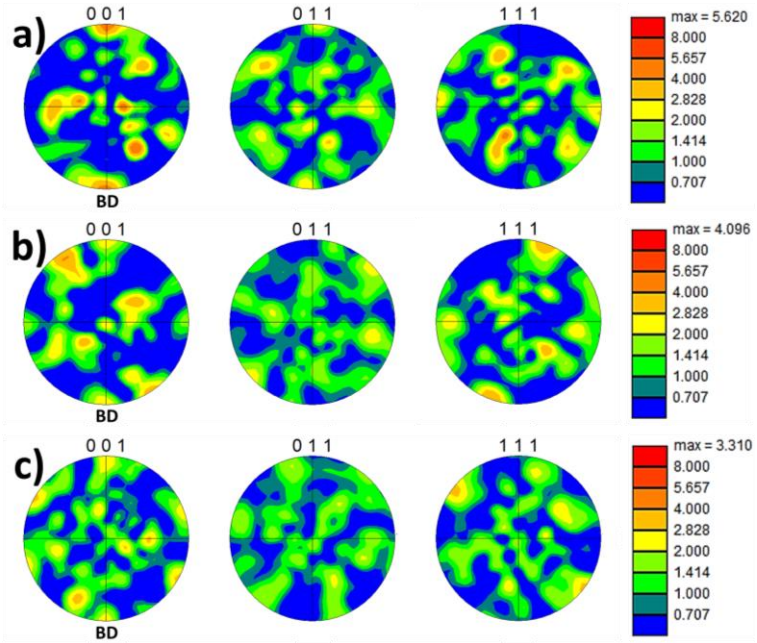

Figure 4.26. Pole figures of AB a) IN718-Y, b) IN718-YF, c) IN718-YFH alloys for (001), (011), and (111) planes.

Figure 4.27 shows EBSD grain boundary maps of AB IN718-Y (Figure 4.27 (a)), IN718-YF (Figure 4.27 (b)), and IN718-YFH (Figure 4.27 (c)) alloys. As inferred from the maps, higher fractions of low angle grain boundaries (misorientation between 2 and 15°) were detected in the microstructures of IN718-Y and IN718-YFH alloys compared with the LAGB fraction in IN718-YF alloy. Low angle grain boundaries are defined as regions where dislocations accumulate. During SLM processing, high thermal gradients result in formation of non-equilibrium microstructure leading an increase in LAGB fraction [213,214]. Higher fractions of low angle grain boundaries in IN718-Y and IN718-YFH alloys may infer the existence of lower residual strains coming from SLM processing. Figure 4.28 presents the KAM maps of AB IN718-Y (Figure 4.28 (a)), IN718-YF (Figure 4.28 (b)), and IN718-YFH (Figure 4.28 (c)) alloys showing the arithmetic mean of the scalar misorientation between kernel groups, or pixel groups [215]. In other words, KAM maps in Figure 4.28 indicate that all the AB alloys include residual strains in their microstructures, originated from high thermal gradients during SLM processing. The minimum residual strain fraction was obtained for IN718-YF alloy

compared with the others which verifies the information about LAGBs and residual strains acquired from grain boundary maps given in Figure 4.27.

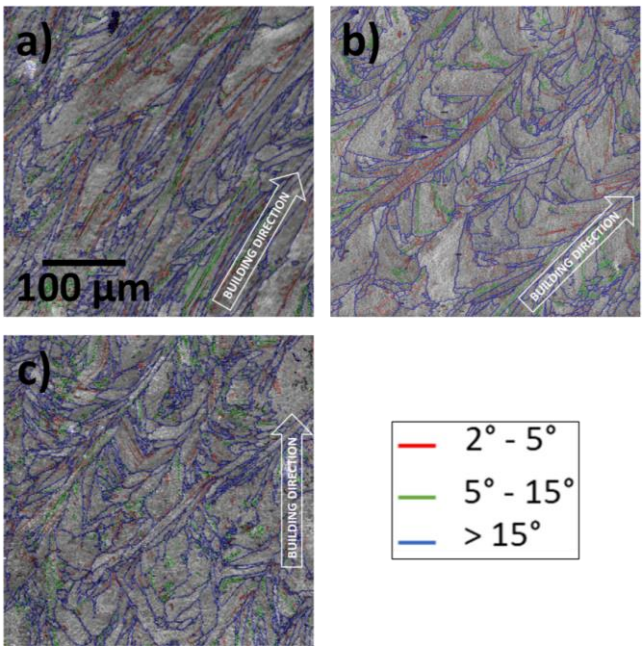

Figure 4.27. EBSD grain boundary maps of AB a) IN718-Y, b) IN718-YF, c) IN718-YFH alloys.

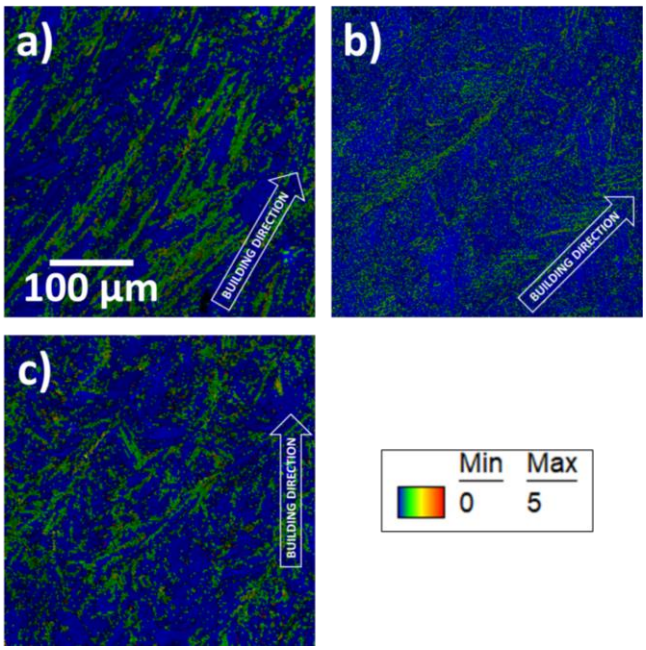

Figure 4.28. EBSD KAM maps of AB a) IN718-Y, b) IN718-YF, c) IN718-YFH alloys.

Figure 4.29 shows SEM micrographs of AB IN718-Y alloy with different second phase particles. According to SEM morphology analysis, coarse (~40 µm) irregular and small (~3 µm) spherical-like precipitates exist in the microstructure. These particles were determined to be Nb-Mo-C (Figure 4.29 (a)), Y-Ti-Al-O (Figure 4.29 (b,e)), Y-Ti-Al-O-C (Figure 4.29 (c,d)), and Nb-Mo Laves phase (Figure 4.29 (f)) using SEM-EDS technique. Detailed information about the compositions of the second phases is given in Table 4.2. Figure 4.30 shows SEM micrographs of the second phase particles in the AB IN718-YF alloy. SEM micrographs reveal that the morphologies of the precipitates are both spherical and irregular with a size below ~10 µm. According to EDS analyses, these precipitates were determined as Nb-Mo-C (Figure 4.30 (a), Figure 4.30 (b)), and Y-Ti-Al-O (Figure 4.30 (c)). The detailed information for elemental distributions of second phase particles are given in Table 4.3. The SEM micrographs of the second phase particles that exist in the AB IN718-YFH microstructure are given in Figure 4.31. The second phase particles having irregular and spherical shape with a size below ~15 µm were determined as Y-Hf-O with trace amounts of Ti and Al (Figure 4.31 (a,d)) and Y-Hf-O (Figure 4.31 (b,c)).

Especially Y-Hf-O particles were observed in spherical shape with a size below ~2 µm. Chemical compositions of the second phase particles are given in Table 4.4.

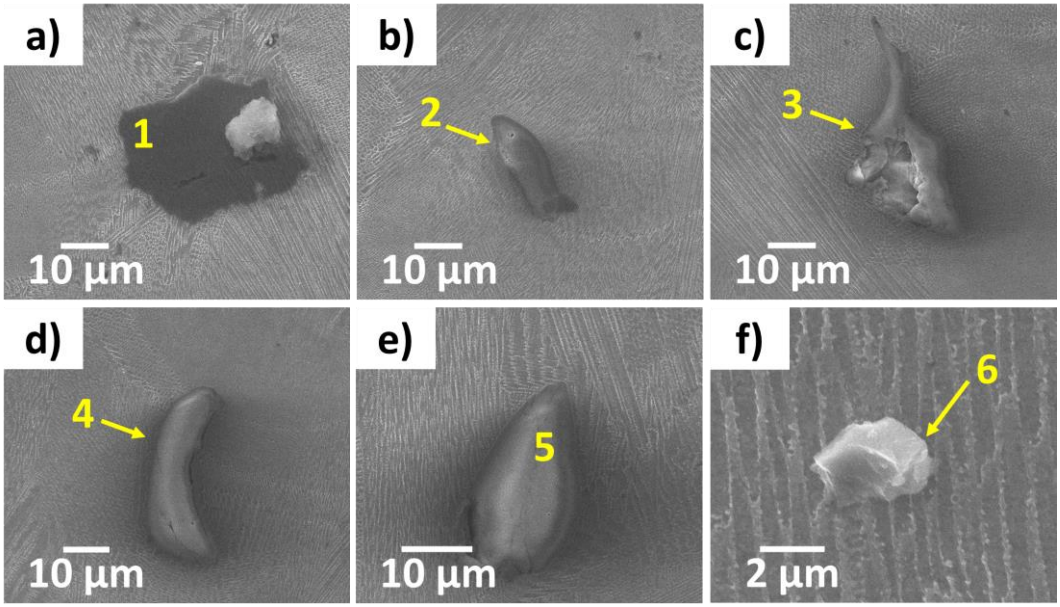

Figure 4.29. SEM micrographs of different precipitates obtained in the AB IN718-Y alloy microstructure.

Table 4.2. Chemical compositions of the precipitates that exist in AB IN718-Y alloy of which SEM micrographs are given in Figure 4.29.

Phase #	**Element fraction (wt.%)**						
	Y	**Ti**	**Al**	**O**	**C**	**Nb**	**Mo**
1	-	-	-	-	18.29	5.31	3.54
2	88.25	3.47	2.91	5.37	-	-	-
3	67.78	4.20	2.40	2.44	4.77	-	-
4	76.76	3.09	2.24	3.88	5.21	-	-
5	79.40	3.30	2.94	3.52	-	-	-
6	-	-	-	-	36.93	-	8.09

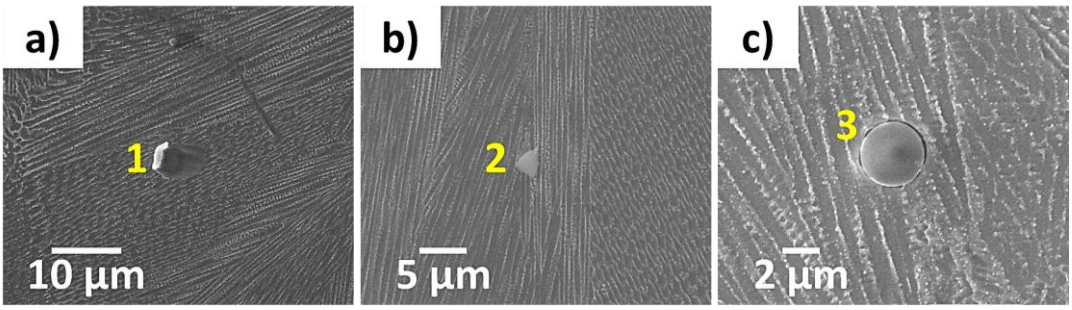

Figure 4.30. SEM micrographs of different precipitates obtained in the AB IN718-YF alloy microstructure.

Table 4.3. Chemical compositions of the precipitates that exist in AB IN718-YF alloy of which SEM micrographs are given in Figure 4.30.

	Element fraction (wt.%)		
	1	**2**	**3**
Y	-	-	74.57
Ti	-	-	3.86
Al	-	-	2.49
O	-	-	3.62
C	0.33	1.59	-
Nb	6.32	5.90	-
Mo	4.55	5.09	-

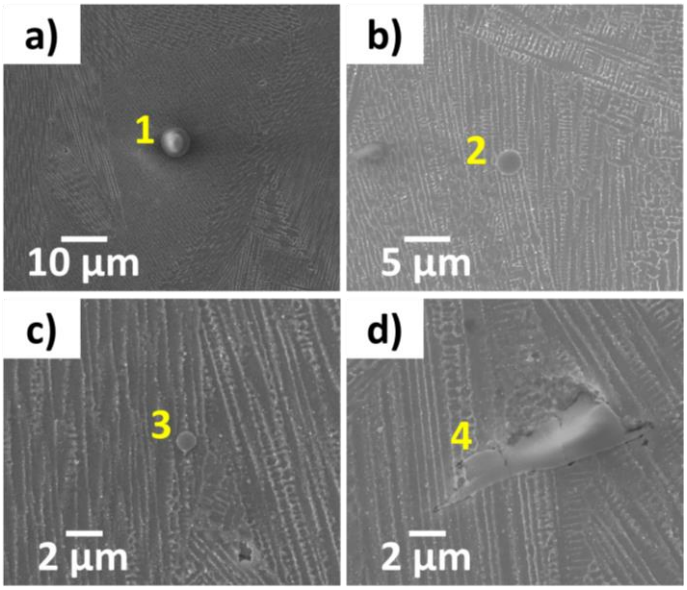

Figure 4.31. SEM micrographs of different precipitates obtained in the AB IN718-YFH alloy microstructure.

Table 4.4. Chemical compositions of the precipitates that exist in AB IN718-YFH alloy of which SEM micrographs are given in Figure 4.31.

	Element fraction (wt.%)			
	1	**2**	**3**	**4**
Y	59.44	41.31	26.17	58.00
Ti	1.85	-	-	2.04
Hf	26.89	24.08	13.48	27.05
Al	1.48	-	-	1.21
O	3.41	2.79	1.75	4.76

Figure 4.32 shows TEM micrographs of AB IN718-Y (Figure 4.32 (a-d)), IN718-YF (Figure 4.32 (e-h)), and IN718-YFH (Figure 4.32 (i-l)) alloys. The micrographs reveal that except Laves particles, almost all particles have circular shape with average particle sizes of 35.2 ± 18.5 nm, 25.6 ± 6.8 nm, and 28.6 ± 5.4 nm for IN718-

Y, IN718-YF, and IN718-YFH alloys, respectively. Number densities of spherical particles were calculated as 2.13 ± 0.35 x 10^{20} m^{-3}, 2.70 ± 0.35 x 10^{20} m^{-3}, and 2.70 ± 1.10 x 10^{20} m^{-3} for IN718-Y, IN718-YF, and IN718-YFH alloys, respectively. Plots showing a comparison of average particle size and number densities of AB alloys are given in Figure 4.33. Figure 4.34 exhibits the plots of the particle size distributions of nano-particles and reveal that most of the particles have size below ~60 nm for IN718-Y alloy while the size is below ~40 nm for IN718-YF and IN718-YFH alloys. Moreover, TEM micrographs of IN718-Y (Figure 4.32 (a)), IN718-YF (Figure 4.32 (e)), and IN718-YFH (Figure 4.32 (i)) reveal that most of the particles precipitated mostly at dislocation cells. The second phase particles precipitated at dislocation cells are reported to stabilize the cells at high temperatures and under irradiation [216]. Sakasegawa et al. that non-stoichiometric Y-Ti-O oxides start to form at sizes below ~15 nm. The oxides gain a stoichiometric form with a size range of ~20-35 nm by Y diffusion and Ostwald ripening during annealing [207,217,218]. Similarly, in their study on Y-(Ce, Hf, La, Sc, and Zr)-O complex oxides, Husák et al. demonstrated that the size range of Y-Hf-O oxides were below ~15 nm when NOs start to form [219]. For number density and particle size distribution analyses in this study, the particles having size up to 100 nm were examined. By TEM-EDS analyses, some of the nano-particles were determined as carbide, Laves phase, and α-Cr, thus the actual number densities of NOs are determined to be less than the values determined using BFTEM images.

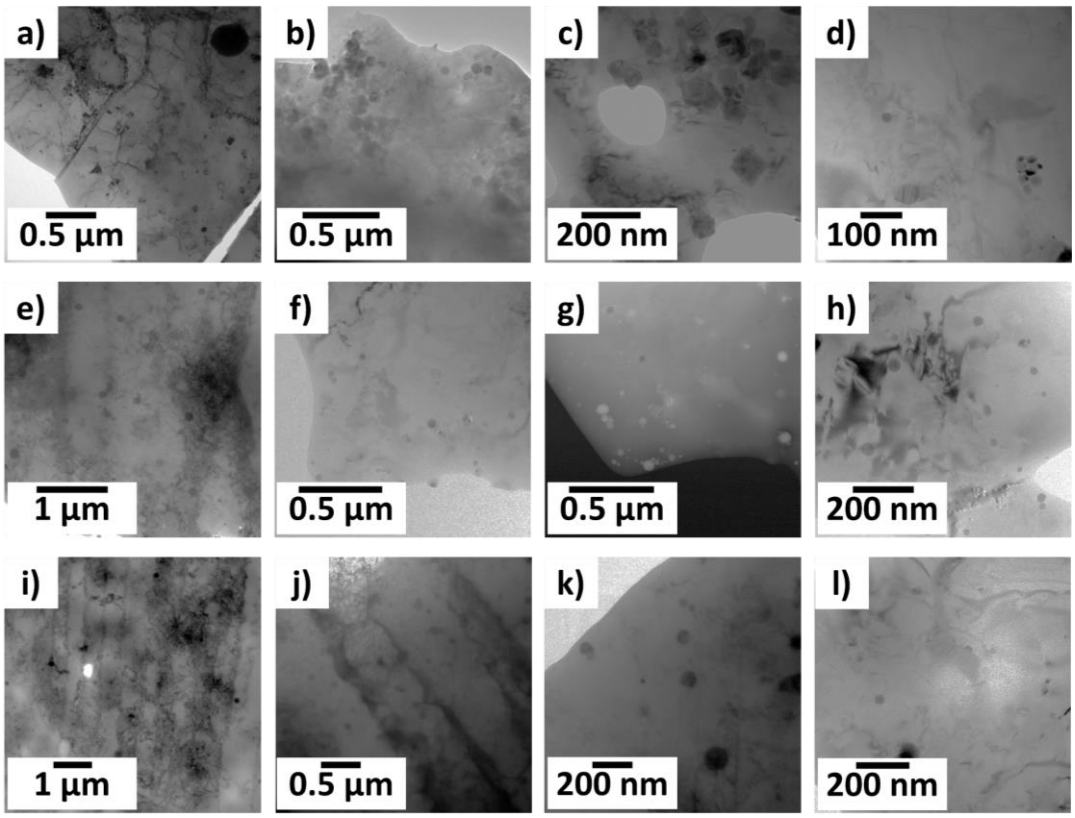

Figure 4.32. BFTEM micrographs of AB (a-d) IN718-Y, (e,f,h) IN718-YF, (i-l) IN718-YFH, and g) STEM/HAADF micrograph of IN718-YF alloy showing second phase particle morphologies and distributions.

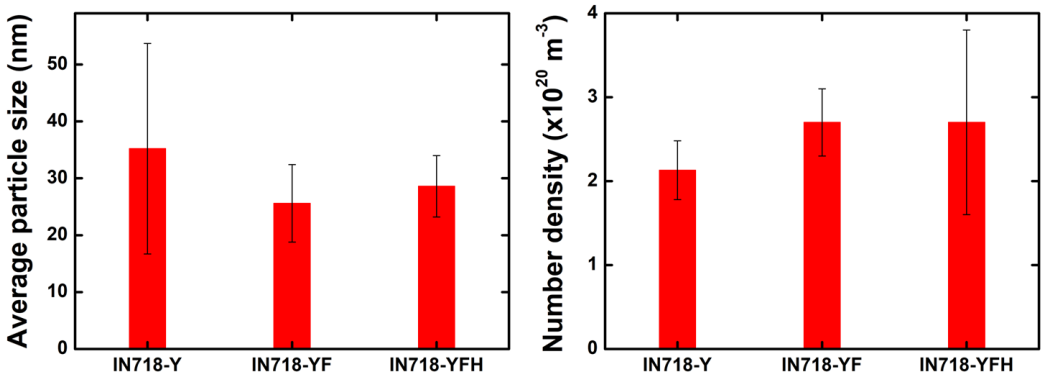

Figure 4.33. Plots showing average particle size and number density comparisons of nano-particles in AB microstructures of IN718-Y, IN718-YF, and IN718-YFH alloys.

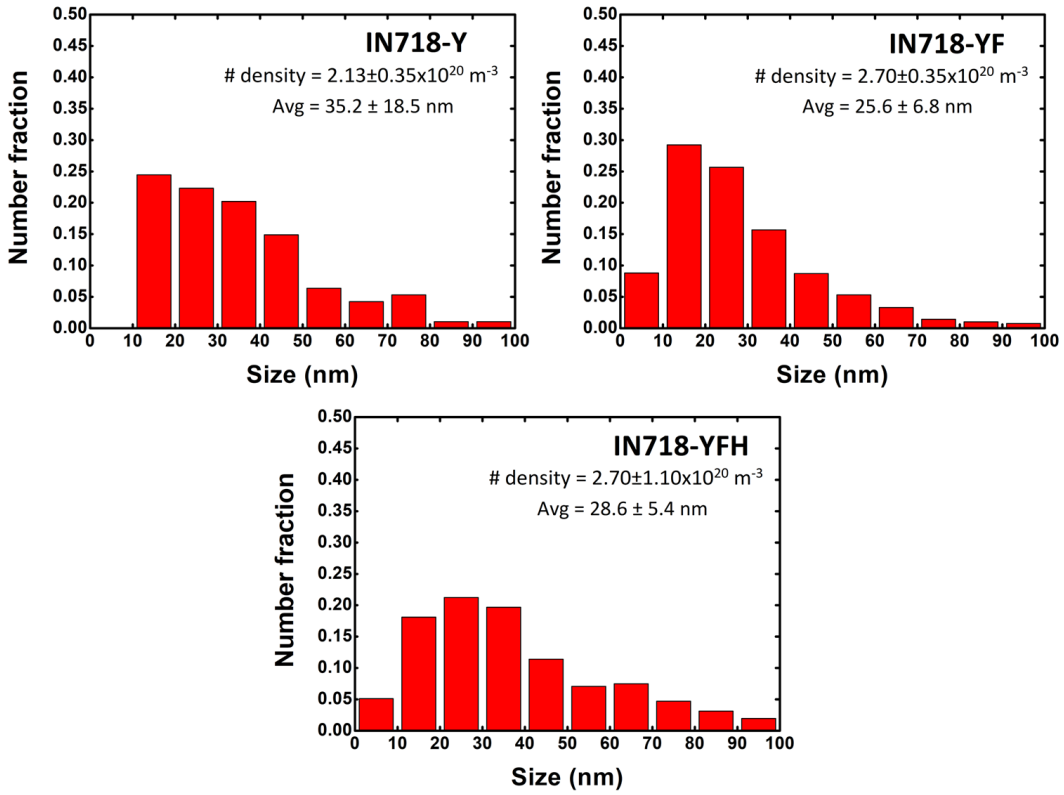

Figure 4.34. Nano-particle size distribution plots of AB IN718-Y, IN718-YF, and IN718-YFH alloys.

In order to determine compositions of second phase particles obtained in Figure 4.32, TEM-EDS analyses were carried out. The EDS maps of AB IN718-Y alloy is given in Figure 4.35. According to the EDS maps, smaller particles were identified as Nb-Mo-Ti carbides, and others are identified as unreacted Y_2O_3, Y-Al-Ti-O, and Nb-Mo (Laves) phase. Figure 4.36 exhibits EDS maps of AB IN718-YF alloy. The maps indicate the existence of Nb-Mo Laves phase, Ti-C, Y-Ti-O, and Y-Ti-Al-O particles. The second phase particles that exist in the AB IN718-YFH alloy are shown in Figure 4.37. The detailed compositional analyses of second phase particles revealed the existence of Nb-C, Y-Hf-O, Si-C, Nb-(Ti)-C, and Nb-Si-C. Chemical compositions of aforementioned precipitates are given in Table 4.5.

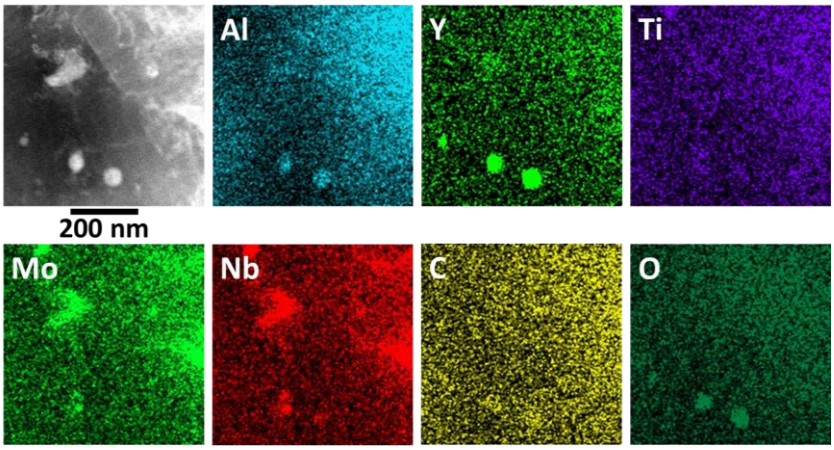

Figure 4.35. TEM-EDS maps of AB IN718-Y alloy.

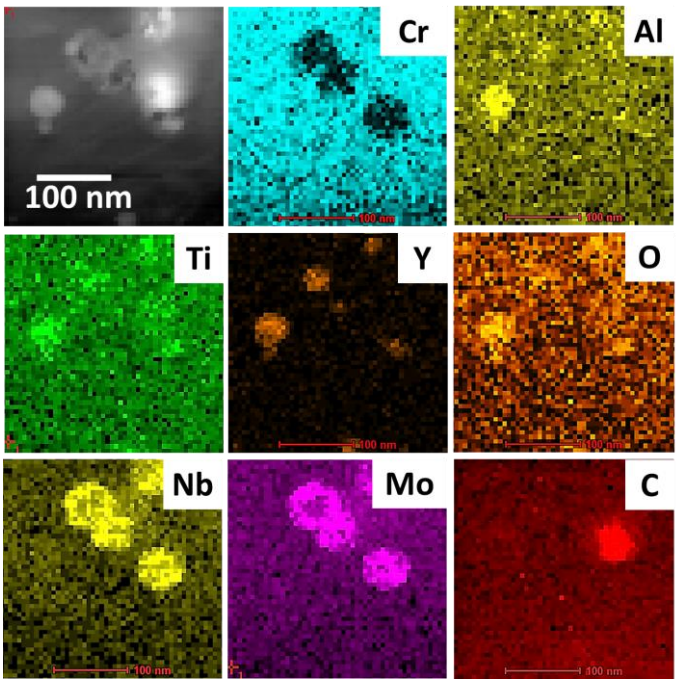

Figure 4.36. TEM-EDS maps of AB IN718-YF alloy.

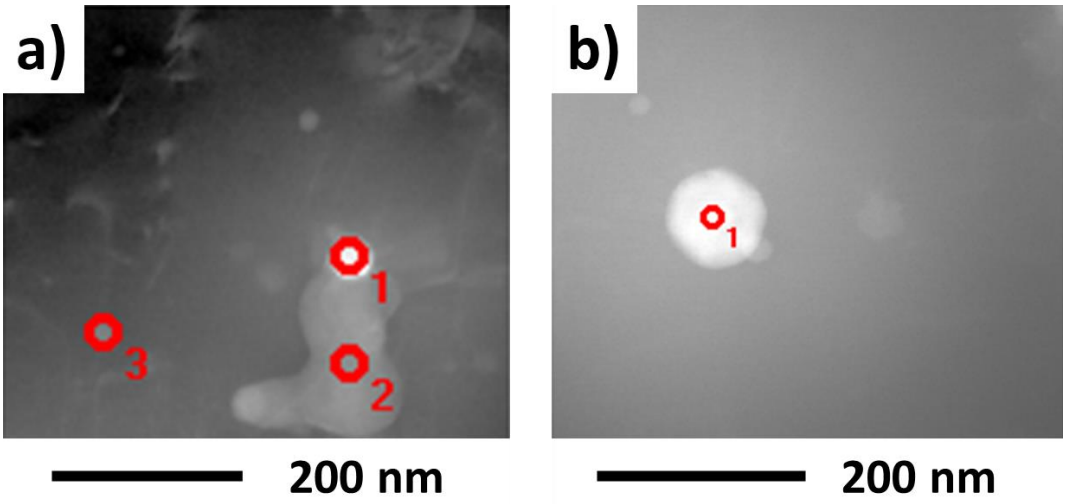

Figure 4.37. STEM/HAADF micrographs of different precipitates obtained in the AB IN718-YFH alloy microstructure.

Table 4.5. TEM-point EDS analysis results of precipitates that exist in AB IN718-YFH alloy of which TEM micrographs are given in Figure 4.37.

Precipitates		**(a)**			**(b)**
		1	**2**	**3**	**1**
Element fraction (wt.%)	**Y**	17.98	16.31	-	10.13
	Ti	1.45	1.54	0.43	0.36
	Hf	18.54	16.20	-	19.67
	Al	-	0.27	-	0.07
	Si	-	1.41	-	1.64
	O	5.14	1.54	2.13	6.44
	C	27.98	30.74	32.04	2.22
	Nb	6.51	0.41	2.07	2.31
	Mo	0.80	-	-	-

When experimental results are compared with thermochemical calculations for AB condition, they are seen to be quite consistent. The existence of quaternary precipitates can be explained by local compositional differences. According to thermochemical calculation results given in Figure 4.3, Y-Al-O starts to form when the Oxygen content exceeds ~1000 ppm at the Al-rich regions which explains the coexistence of Y-Ti-O and Y-Al-O precipitates rather than the formation of Y-Ti-Al-O phase [220,221]. Moreover, the Y-Ti-Al-O-C phase can be explained as coexistence of Y-Ti-O and Al-C phases or Y-Al-O and Ti-C phases [222,223]. Similarly, existences of Y-Hf-O oxides with some carbide contents were reported in the literature [220,224].

Figure 4.38 shows hardness comparison of AB alloys. The plot reveals that increasing nano-particle content results in an increase in hardness values. The increase in Laves phase fraction was also detected for IN718-YF and IN718-YFH alloys which is the main reason of hardness improvement. The hardness values of the AB alloys were measured as 318 ±7, 327 ± 9, and 348 ± 8 for IN718-Y, IN718-YF, and IN718-YFH alloys, respectively. Compared with standard IN718 alloy, ~6%, ~9%, and ~16% increase of the hardness values was observed.

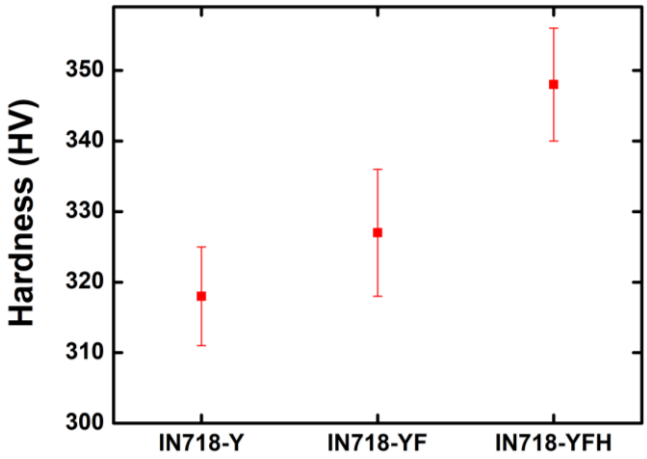

Figure 4.38. The plot showing comparison of hardness values of AB alloys.

Stress (σ) – Strain (ε) plot showing the RT mechanical behaviors of AB alloys under uniaxial tensile stresses is given in Figure 4.39. The yield strengths of the AB IN718-

Y, IN718-YF, and IN718-YFH alloys were determined as 821.5 ± 7.8, 860.0 ± 7.1, and 863.0 ± 4.2 MPa, respectively. Moreover, IN718-Y (~22.2%) and IN718-YFH (~20.3%) alloys showed extensive ductility while IN718-YFH alloy showed relatively limited ductility of ~9.7 % at RT. The yield strength of IN718 alloys produced by SLM is determined to range between ~600 and ~800 MPa with a ductility up to ~25% at RT [113,205,225–227]. Therefore, it is determined that the existence of nano-particles enhanced tensile strengths of AB alloys with a negligible loss of ductility for IN718-Y and IN718-YF alloys, and with a considerable reduction in ductility for IN718-YFH alloy.

At 700°C, the yield strengths of AB IN718-YF and IN718-YFH alloys were determined as 715.0 ± 36.1 and 752.0 ± 84.2 MPa with ductility of 4.4% and 4.2%, respectively. The plot showing tensile behaviors of AB IN718-YF and IN718-YFH alloys at 700 °C is given in Figure 4.40. Also, the numerical values of tensile properties of AB IN718-Y, IN718-YF, and IN718-YFH alloys at RT and 700 °C are given in Table 4.6. Compared with RT tensile properties, the decreases of ~17% and ~13% in yield strengths and the losses of ~78% and ~57% in ductility were obtained at 700 °C for AB IN718-YF and IN718-YFH alloys, respectively. The loss of strength of IN718-YFH alloy were less than IN718-YF, so IN718-YFH alloy showed higher stability than IN718-YF alloy. Moreover, the reason of the loss of ductility at 700 °C is explained by nucleation of strengthening precipitates of γ'/γ" and their pinning activities at elevated temperatures [113]. Sun et al. in their study on improvement of mechanical properties of IN718 produced by SLM method obtained that AB IN718 alloy has a yield strength of ~691 MPa and a ductility of 42.5% at 650 °C [228]. In other study on temperature-strain rate dependence of SLM'ed IN718 alloy at elevated temperatures, the yield strength of AB IN718 alloy was obtained as ~876 MPa and ~647 MPa at 650 and 750 °C, respectively. The ductility was obtained as ~5.9 and ~7.6% for the tensile tests that were carried out at 10^{-4} s^{-1} strain rate [229]. The tensile test results obtained from literature indicate that IN718 alloy is strengthened by nano-particles at RT and even at 700 °C.

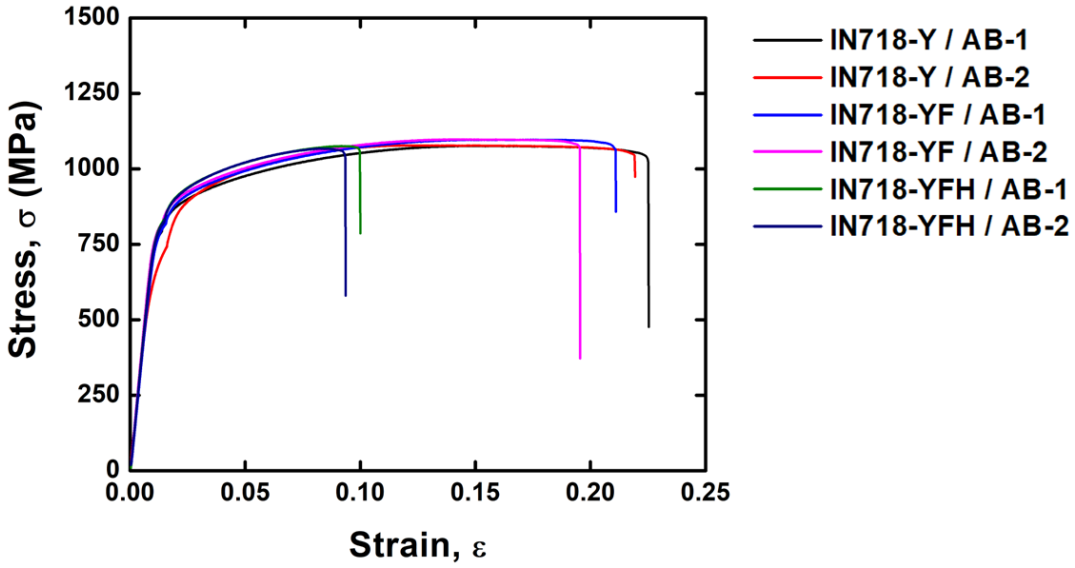

Figure 4.39. Stress-Strain curves of AB alloys tested at RT.

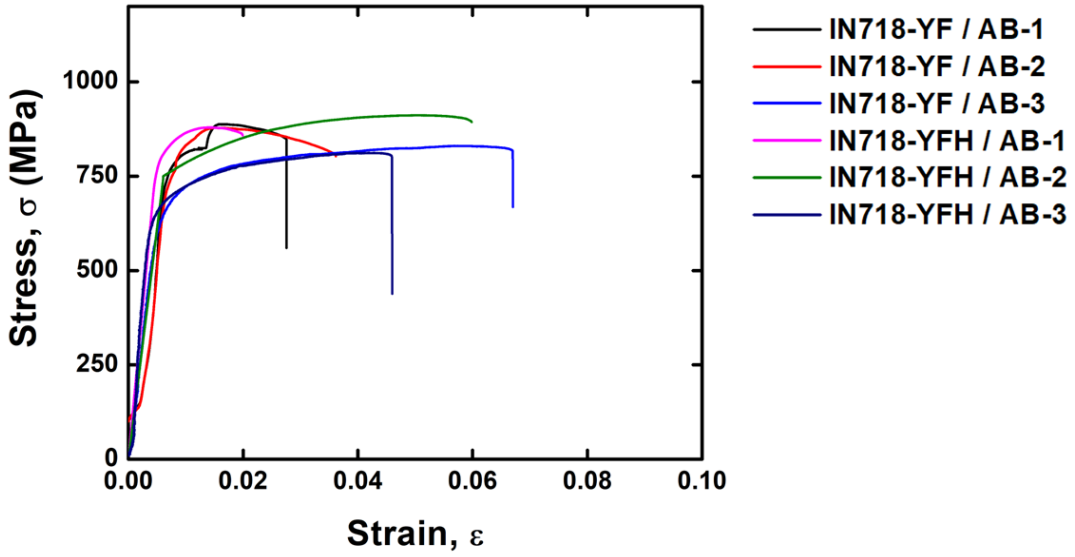

Figure 4.40. Stress-Strain curves of AB alloys tested at 700 °C.

Table 4.6. Tensile properties of AB samples tested at RT and 700 °C.

Sample	T (°C)	Elastic Modulus (E)	Yield Strength (MPa)	Tensile Strength (MPa)	Strain at Fracture (%)
IN718-Y	RT	221.0 ± 41.0	821.5 ± 7.8	1077.0 ± 1.4	22.2 ± 0.4
IN718-YF	RT	194.0 ± 4.2	860.0 ± 7.1	1097.5 ± 0.7	20.3 ± 1.1
IN718-YF	700	146.7 ± 9.0	715.0 ± 36.1	865.3 ± 31.0	4.4 ± 2.1
IN718-YFH	RT	202.5 ± 12.0	863.0 ± 4.2	1071.5 ± 6.4	9.7 ± 0.4
IN718-YFH	700	162.7 ± 40.0	752.0 ± 84.2	867.7 ± 51.0	4.2 ± 2.0

4.6 Microstructures and Mechanical Properties in Heat-treated Condition

Figure 4.41 shows SEM micrographs of IN718-Y (Figure 4.41 (a,d)), IN718-YF (Figure 4.41 (b,e)), and IN718-YFH (Figure 4.41 (c,f)) alloys in HT condition (1050 °C – 1h). According to SEM micrographs, HT microstructures consist of relatively fine and spherical second phase particles with some irregular shaped precipitates. Figure 4.42 shows EBSD orientation maps of HT IN718-Y (Figure 4.42 (a)), IN718-YF (Figure 4.42 (b)), and IN718-YFH (Figure 4.42 (c)) alloys. Orientation maps indicate no considerable preferred orientation for all the alloys. Moreover, it is seen that melt pools are preserved for all the alloys after heat treatment. For IN718 alloy, well defined grains are supposed to be observed after heat treatment at 1050 °C for 1h [230,231]. The behavior of preserving melt pool structure, i.e, stabilization of the initial microstructure, is addressed to grain boundary pinning effect provided by NOs [142,169,178,232]. For further texture analysis, pole figures were obtained for (001), (011), and (111) planes. Related pole figures are given in Figure 4.43. Random texture evolution was observed for all the HT grades. However, preferred grain growth along (001) orientation was detected for IN718-Y alloy while no growth in preferred direction was detected for IN718-YF and IN718-YFH alloys.

Figure 4.44 shows EBSD grain boundary maps of HT IN718-Y (Figure 4.44 (a)), IN718-YF (Figure 4.44 (b)), and IN718-YFH (Figure 4.44 (c)) alloys. As indicated by the maps, higher fractions of low angle grain boundaries (misorientation between 2 and 15°) were detected in the microstructures of IN718-Y alloy while less amounts of LAGBs were detected in IN718-YF and IN718-YFH alloys. When compared with the LAGB fractions in AB condition, all the alloys have shown decrease in strains after heat treatment. It has been observed that the alloy in the minimum residual strain state is the IN718-YF alloy, as in the AB condition. Consisting higher fractions of low angle grain boundaries of IN718-Y and IN718-YFH alloys than IN718-YF alloy indicates that the maximum fraction of residual strains was relieved in IN718-YF alloy. Figure 4.45 shows KAM maps of HT IN718-Y (Figure 4.45 (a)), IN718-YF (Figure 4.45 (b)), and IN718-YFH (Figure 4.45 (c)) alloys. KAM maps indicate that all the HT alloys include residual strains in their microstructures. The minimum residual strain fraction was obtained for IN718-YF alloy compared with the others which verifies the information about LAGBs and residual strains acquired from grain boundary maps given in Figure 4.44.

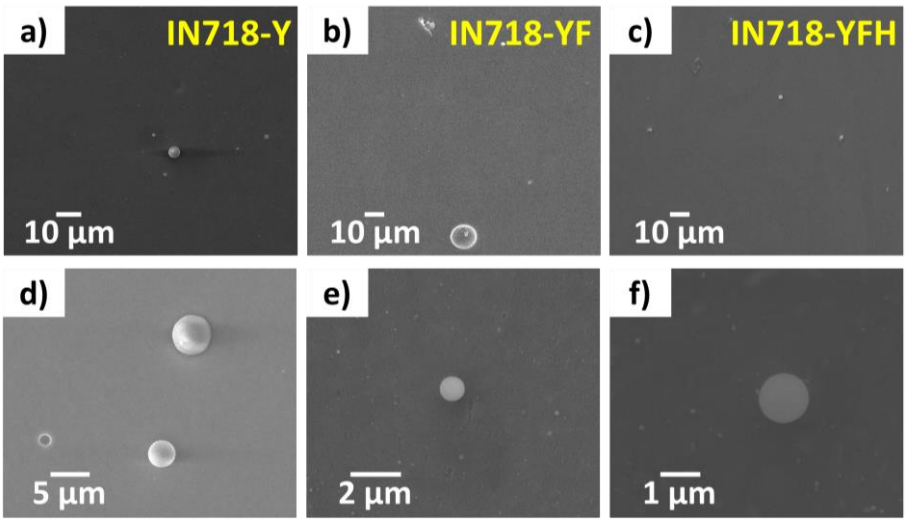

Figure 4.41. SEM micrographs of HT microstructures: (a,d) IN718-Y, (b,e) IN718-YF, (c,f) IN718-YFH.

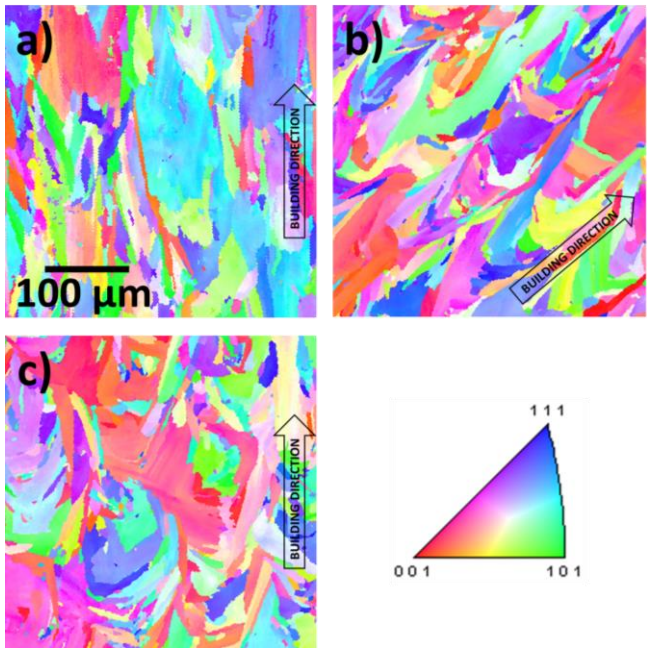

Figure 4.42. EBSD orientation maps of HT a) IN718-Y, b) IN718-YF, c) IN718-YFH alloys.

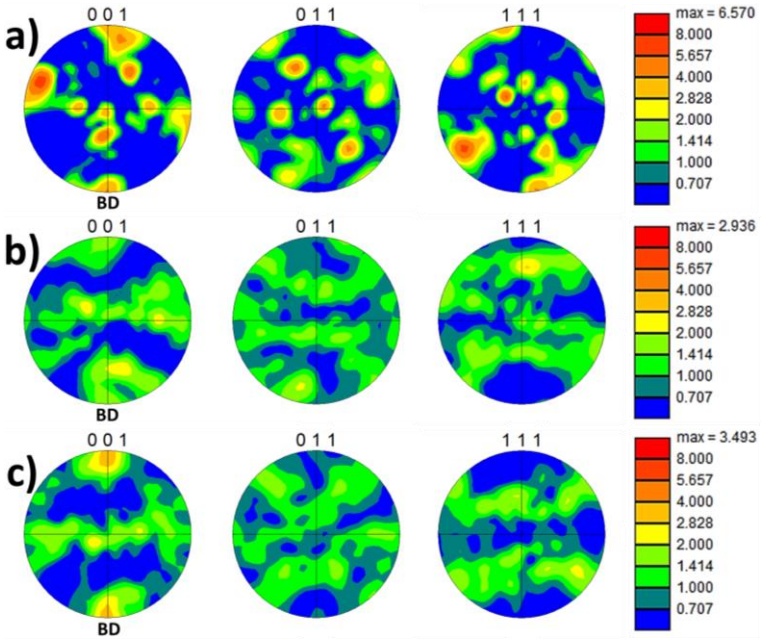

Figure 4.43. Pole figures of HT a) IN718-Y, b) IN718-YF, c) IN718-YFH alloys for (001), (011), and (111) planes.

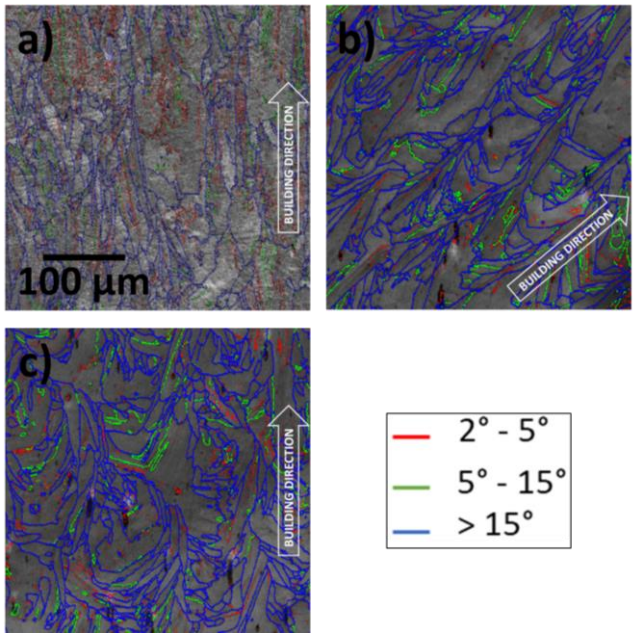

Figure 4.44. EBSD grain boundary maps of HT a) IN718-Y, b) IN718-YF, c) IN718-YFH alloys.

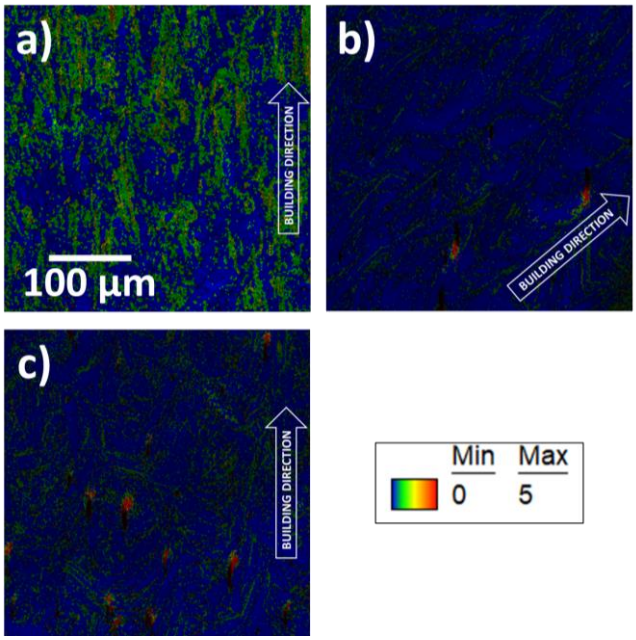

Figure 4.45. EBSD KAM maps of HT a) IN718-Y, b) IN718-YF, c) IN718-YFH alloys.

Figure 4.46 shows SEM micrographs of HT IN718-Y alloy with different second phase particles. According to SEM morphology analysis, coarse (~50 µm) irregular

and small (< 10 μm) spherical-like shaped precipitates exist in the microstructure. These particles were determined to be Y-Ti-Al-O (Figure 4.46 (a,c,d)) and α-Cr (Cr-Ni-Fe) with a trace amount of Ti (Figure 4.46 (b)), by compositional analyses performed with SEM-EDS method. The detailed information about elemental distribution of second phases is given in Table 4.7. Figure 4.47 shows SEM micrographs of the second phase particles in the HT IN718-YF alloy microstructure. SEM micrographs reveal that the precipitates are either in spherical or irregular shape with a size below ~5 μm. According to EDS analyses, these precipitates were determined as Nb-Mo-C (Figure 4.47 (a)), Nb-Ti-C-N (Figure 4.47 (b)), and Y-Ti-Al-O (Figure 4.47 (c)). The detailed information for elemental distributions of second phase particles are given in Table 4.8. The SEM micrographs of the second phase particles that exist in the HT IN718-YFH microstructure are given in Figure 4.48. The second phase particles were determined as Y-Hf-O with trace amounts of Ti and Al with irregular and spherical shape in size below ~10 μm. Chemical compositions of these second phase particles are given in Table 4.9.

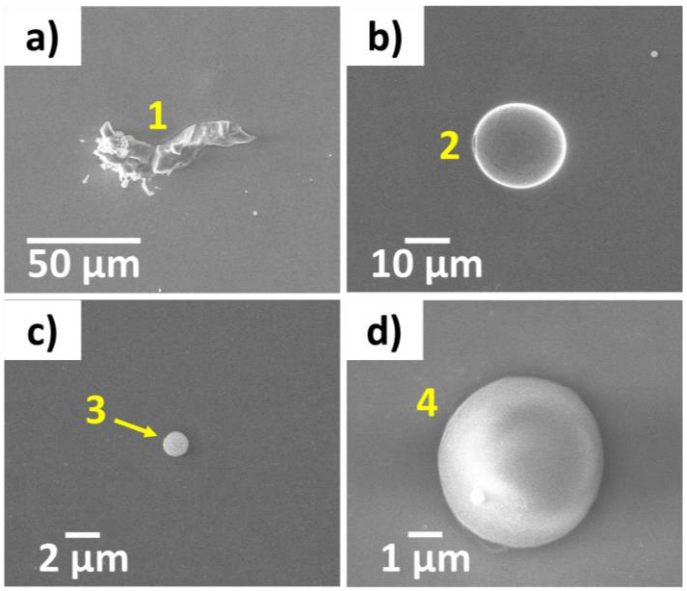

Figure 4.46. SEM micrographs of different precipitates obtained in the HT IN718-Y alloy microstructure.

Table 4.7. Chemical compositions of the precipitates that exist in HT IN718-Y alloy of which SEM micrographs are given in Figure 4.46.

	Element fraction (wt.%)			
	1	**2**	**3**	**4**
Y	87.88	-	47.30	88.27
Ti	3.29	1.31	1.35	2.06
Al	2.89	-	2.88	1.62
O	5.93	-	3.76	8.05
Ni	-	56.88	-	-
Cr	-	22.84	-	-
Fe	-	18.97	-	-

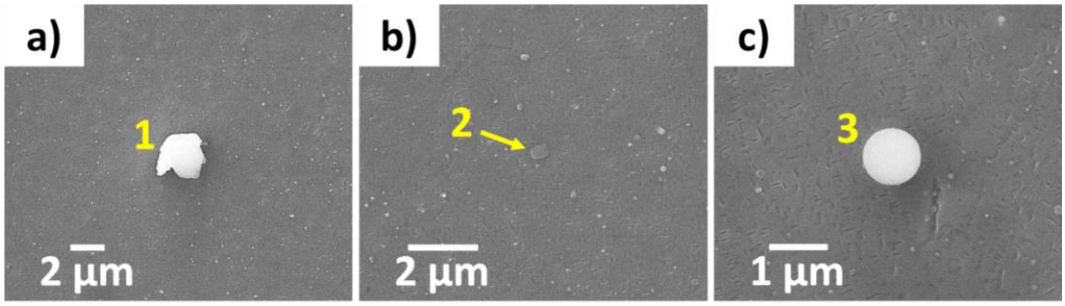

Figure 4.47. SEM micrographs of different precipitates obtained in the HT IN718-YF alloy microstructure.

Table 4.8. Chemical compositions of the precipitates that exist in HT IN718-YF alloy of which SEM micrographs are given in Figure 4.47.

	Element fraction (wt.%)		
	1	**2**	**3**
Y	-	-	34.01
Ti	-	3.65	1.95
Al	-	-	7.12
N	-	0.68	-
O	-	-	2.57
C	1.62	2.90	-
Nb	6.89	24.76	-
Mo	5.56	-	-

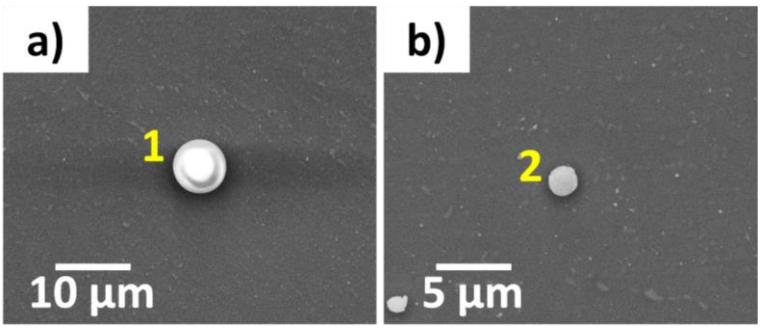

Figure 4.48. SEM micrographs of different precipitates obtained in the HT IN718-YFH alloy microstructure.

Table 4.9. Chemical compositions of the precipitates that exist in HT IN718-YFH alloy of which SEM micrographs are given in Figure 4.48.

Element fraction (wt.%)		
	1	**2**
Y	60.66	41.74
Ti	1.82	2.94
Al	1.10	9.50
Hf	23.23	12.51
O	3.36	3.53

Figure 4.49 shows BFTEM micrographs of HT IN718-Y (Figure 4.49 (a-d)), IN718-YF (Figure 4.49 (e-h)), and IN718-YFH (Figure 4.49 (i-l)) alloys. The micrographs reveal that except bulk shaped Laves and disc-shaped γ" particles, almost all particles have circular shape with average particle sizes of 12.7 ± 8.2 nm, 19.5 ± 13.8 nm, and 20.8 ± 15.3 nm for IN718-Y, IN718-YF, and IN718-YFH alloys, respectively. Moreover, the average particle sizes of γ" precipitates were calculated as 86.3 ± 36.3 and 88.8 ± 34.1 nm for IN718-YF and IN718-YFH alloys, respectively. For HT IN718-Y alloy, a trace amount of γ" was detected, however, the amount was

insufficient to carry out particle size and number density analyses. BFTEM micrograph inferring the existence of needle-like γ" precipitates in trace amount is given in Figure 4.50. The reason of existence of γ" precipitates is the cooling rate applied after heat treatments. Moreover, in BFTEM microstructures of HT IN718-YF (Figure 4.49 (g,h)) and IN718-YFH (Figure 4.49 (k,l)) alloys, the existence of spherical-shaped nano-particles can be clearly seen. These particles are assumed to be secondary γ' precipitates that form during cooling period [233]. It is known that γ' and γ" precipitations depend on cooling rates of 5 K/s and 0.2 K/s, respectively [234,235]. In this study, the cooling time elapsed between 900 and 600 °C was determined as 96 min (0.052 °C/s) which provides enough time for γ' and γ" precipitations.

Plots showing comparisons of average particle sizes of spherical shaped nano-particles (Figure 4.51 (a)) and average particle sizes of disc-shaped γ" precipitates (Figure 4.51 (b)) are given in Figure 4.51. Moreover, the number densities of spherical particles were calculated as 8.81 ± 4.12 x 10^{21} m^{-3}, 4.15 ± 0.80 x 10^{22} m^{-3}, and 1.57 ± 1.0 x 10^{21} m^{-3} for HT IN718-Y, IN718-YF, and IN718-YFH alloys, respectively. The number densities of γ" particles were calculated as 3.72 ± 2.53 x 10^{20} m^{-3} and 2.51 ± 0.71 x 10^{20} m^{-3} for HT IN718-YF and IN718-YFH alloys, respectively. Figure 4.52 exhibits the plots showing comparison of number densities of spherical nano-particles (Figure 4.52 (a)) and γ" precipitates (Figure 4.52 (b)). According to particle size distribution plots of nano-particles existing in the alloy microstructures (Figure 4.53), most of the particles have a size below ~20 nm for IN718-Y alloy while particle size is below ~30 nm for IN718-YF and IN718-YFH alloys. Moreover, there is ~64%, ~24%, and ~27% decrease in the particle size for HT IN718-Y, IN718-YF, and IN718-YFH alloys.

The BFTEM micrograph of IN718-YF alloy (Figure 4.49 (e)) reveals the formation of annealing twins while the BFTEM micrograph of IN718-YFH alloy given in Figure 4.49 (i) reveals the conservation of cellular structure where most of the precipitates are precipitated preferentially at dislocation cells stabilizing the cells at

high temperatures and under irradiation [216]. This explains the existence of dislocation cells even after heat treatment.

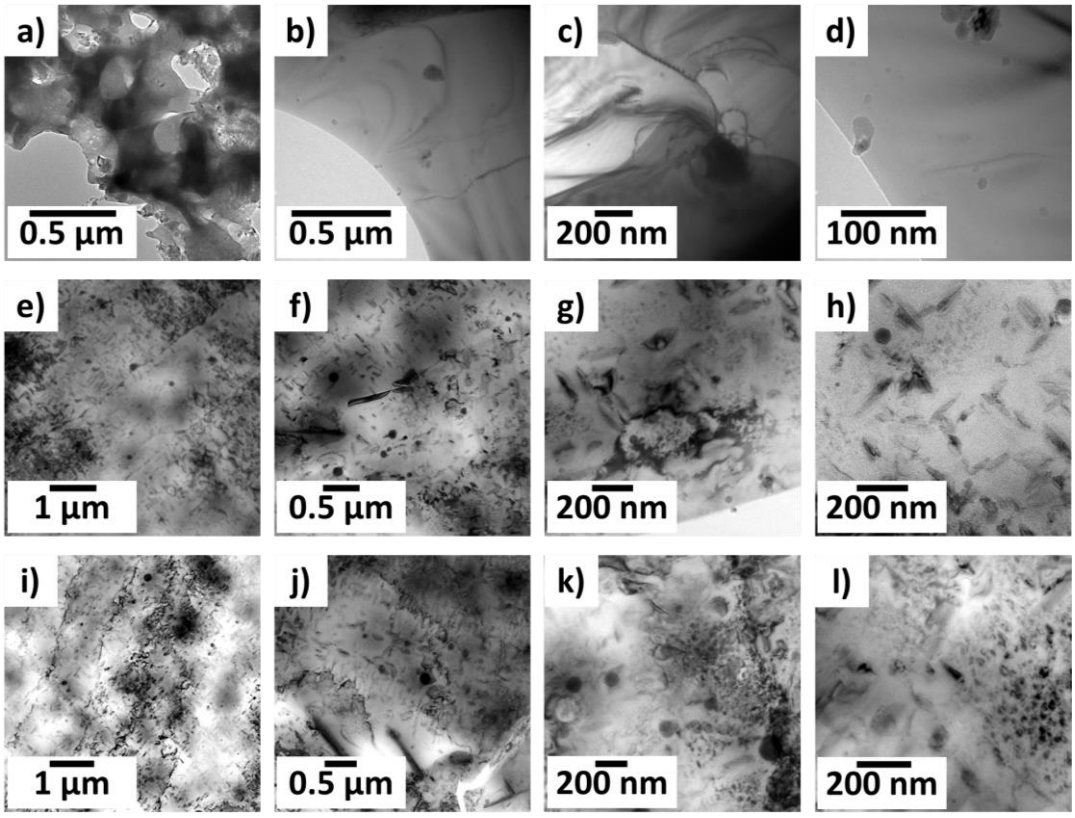

Figure 4.49. BFTEM micrographs of HT (a-d) IN718-Y, (e-h) IN718-YF, and (i-l) IN718-YFH alloys showing second phase particle morphologies and distributions.

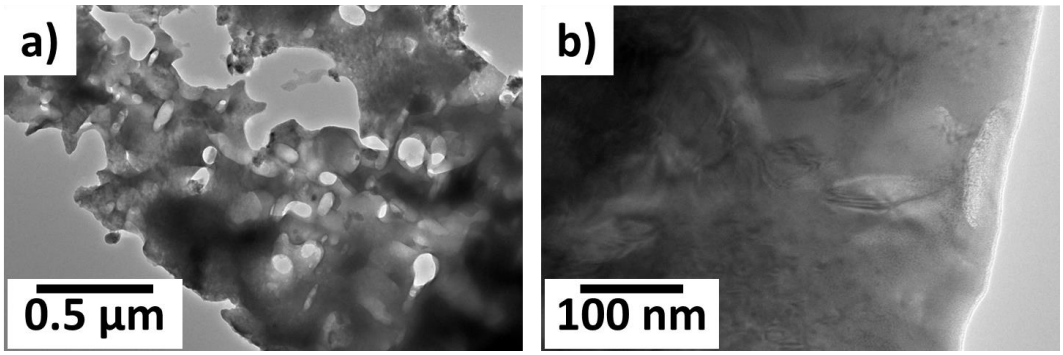

Figure 4.50. BFTEM micrographs of HT IN718-Y alloy that infer the existence of γ" precipitates.

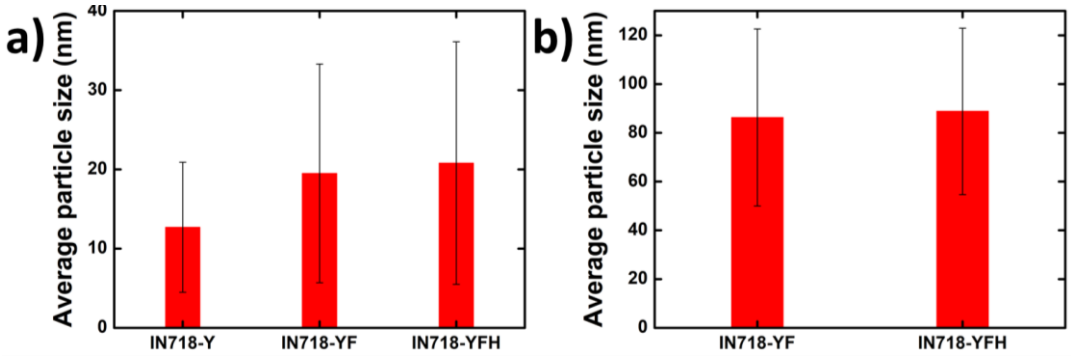

Figure 4.51. Plots showing average particle size comparisons of a) nano-particles and b) γ" precipitates in HT microstructures of IN718-Y, IN718-YF, and IN718-YFH alloys.

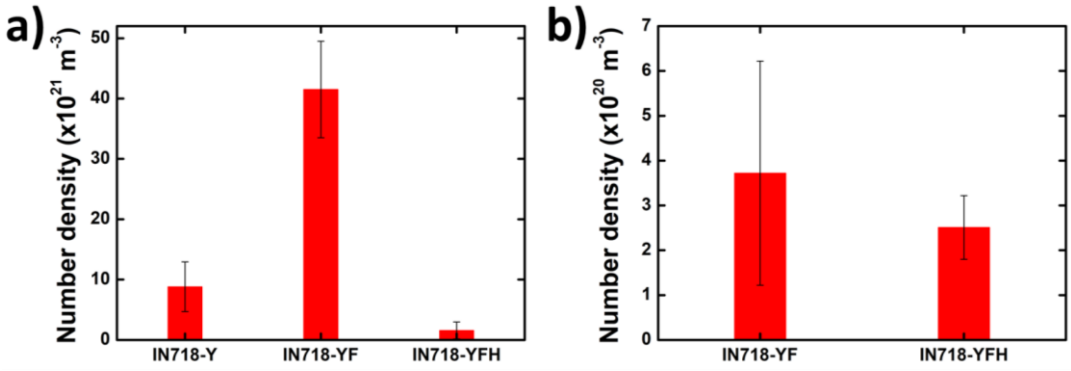

Figure 4.52. Plots showing number density comparisons of a) nano-particles and b) γ" precipitates in HT microstructures of IN718-Y, IN718-YF, and IN718-YFH alloys.

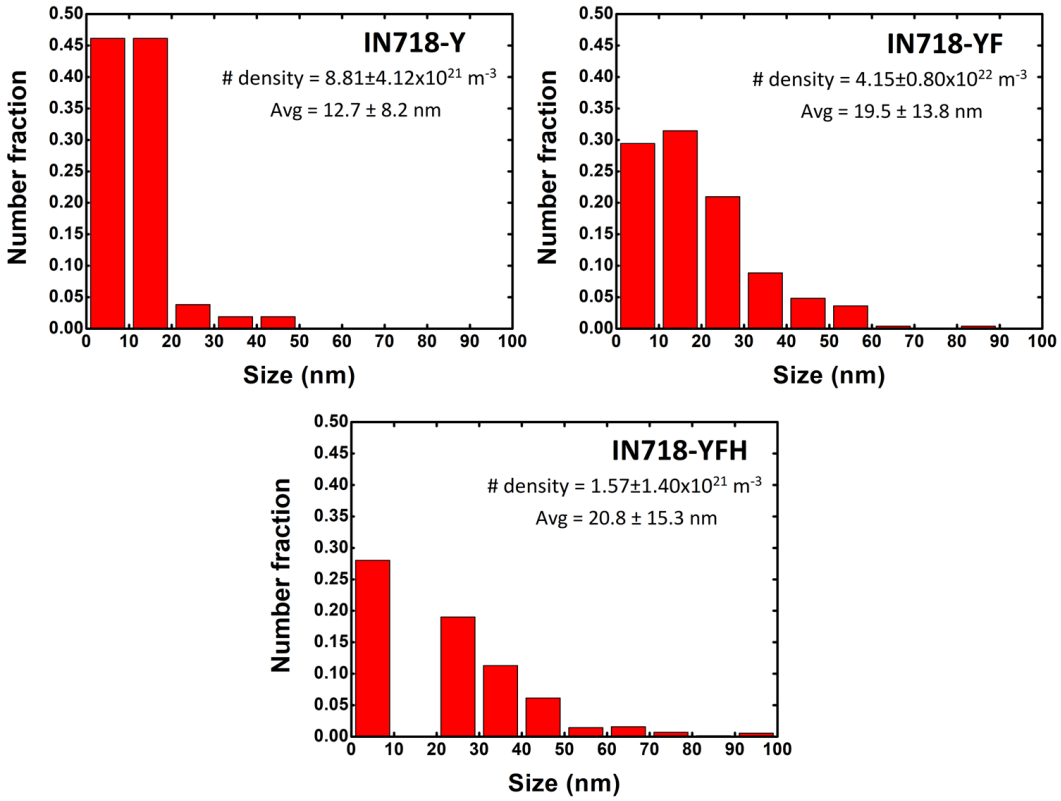

Figure 4.53. Nano-particle size distribution plots of HT IN718-Y, IN718-YF, and IN718-YFH alloys.

Figure 4.54 shows EDS maps of nanoparticles that were obtained in HT IN718-Y microstructure. In the maps, high density of Ni-Cr-Fe-(Ti) particles was observed. These particles are attributed to be Laves phase. Moreover, the existence of Ni-Cr-Fe-(Ti) Laves particles having ~15 μm has been revealed by SEM-EDS analysis given in Figure 4.46. The change of morphology to spherical shaped particles enables the use of Laves phase for strengthening purposes. HAADF TEM micrographs of HT IN718-YF alloy are given in Figure 4.55. The particles observed in HAADF images were identified as δ phase, Ni-Nb-Ti Laves phase, Nb-Mo-Ti Laves phase, and Ni-Nb-Ti-(Mo) Laves phase. Point EDS results showing chemical compositions of mentioned particles are given in Table 4.10. Figure 4.56 represents HAADF TEM micrographs that show the particles observed in HT IN718-YFH microstructure. According to point EDS analyses, these particles were identified as Nb-Mo Laves,

Nb-Ti-C, Nb-Mo-C, Y-Ti-Al-O coexisting with Nb-Mo-C, and γ'' phases. Numerical results of EDS analyses of these particles are given in Table 4.11.

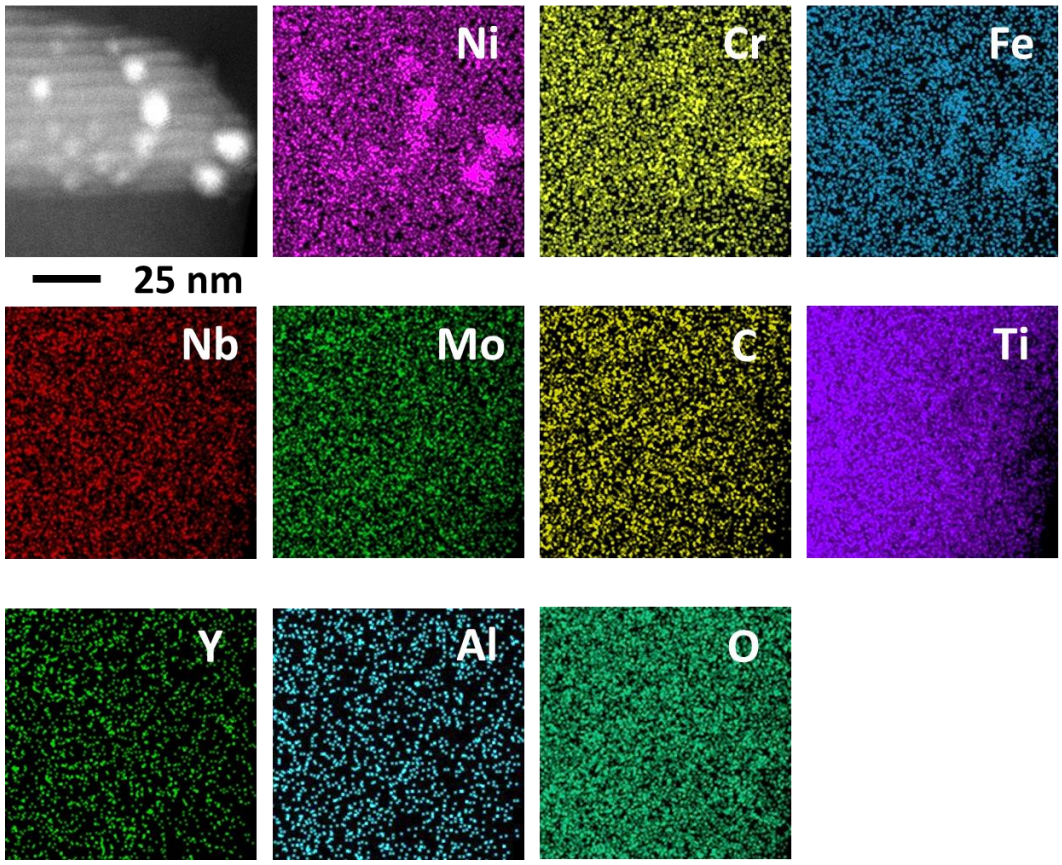

Figure 4.54. TEM-EDS maps of HT IN718-Y alloy.

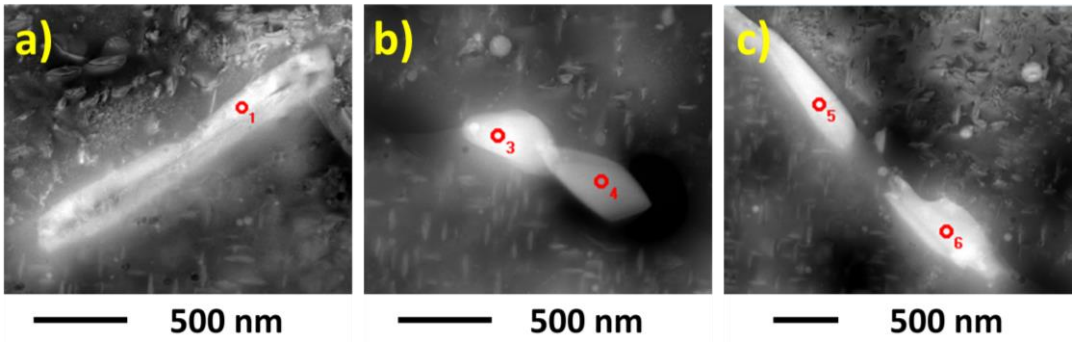

Figure 4.55. STEM/HAADF micrographs of different precipitates obtained in the HT IN718-YF alloy microstructure.

Table 4.10. TEM-point EDS analysis results of the precipitates that exist in HT IN718-YF alloy of which TEM micrographs are given in Figure 4.55.

Precipitates		**(a)**	**(b)**		**(c)**	
		1	**3**	**4**	**5**	**6**
Element fraction (wt.%)	Y	-	-	-	-	-
	Ti	-	2.48	3.99	2.26	1.93
	Nb	24.28	16.98	38.46	18.30	23.28
	Mo	-	-	1.11	0.72	0.16
	Ni	40.32	50.62	-	55.65	50.81

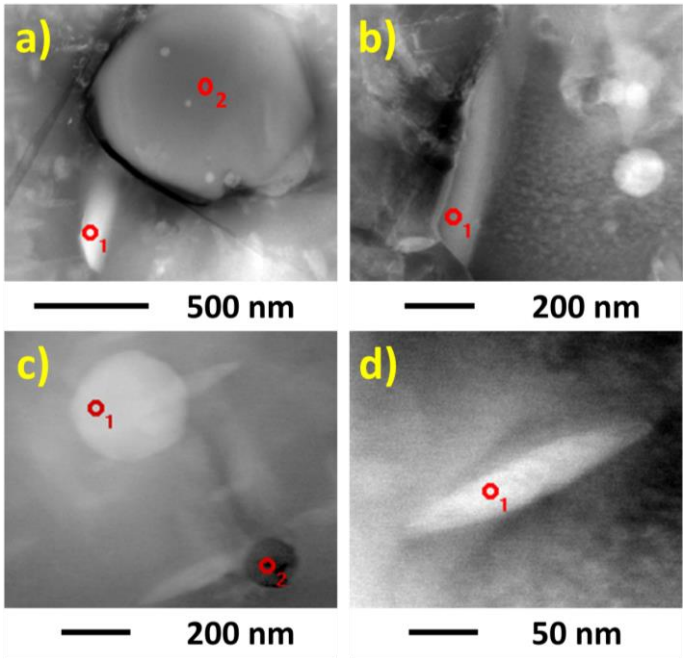

Figure 4.56. STEM/HAADF micrographs of different precipitates obtained in the HT IN718-YFH alloy microstructure.

Table 4.11. TEM-point EDS analysis results of the precipitates that exist in HT IN718-YFH alloy of which TEM micrographs are given in Figure 4.56.

Precipitates		**(a)**		**(b)**	**(c)**		**(d)**
		1	**2**	**1**	**1**	**2**	**1**
Element fraction (wt.%)	Y	-	-	-	13.61	9.83	-
	Ti	-	2.53	-	0.50	0.18	-
	Al	-	-	-	1.56	1.33	-
	O	-	-	-	4.08	2.32	-
	C	-	47.49	35.90	15.62	38.16	-
	Nb	13.41	47.70	15.82	2.94	2.43	7.93
	Mo	7.85	-	9.58	1.50	3.04	-
	Ni	-	-	-	-	-	36.57

Figure 4.57 shows hardness comparison of HT alloys. The plot reveals that after heat treatment, increasing oxide content with decreasing non-homogeneity in the microstructures results in an increase in hardness values, which verifies the effectiveness of oxide dispersion strengthening. The hardness values of the HT alloys were measured as 389 ±8, 401 ± 7, and 416 ± 8 for IN718-Y, IN718-YF, and IN718-YFH alloys, respectively. Compared with AB state, ~22%, ~23%, and ~20% increase in hardness values were observed after heat treatment for IN718-Y, IN718-YF, and IN718-YFH alloys, respectively.

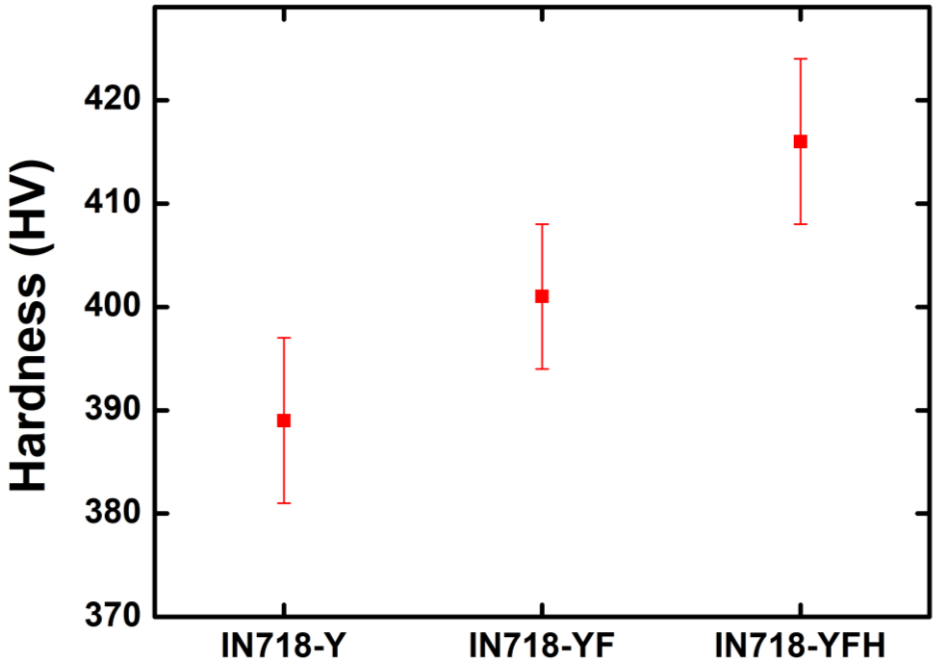

Figure 4.57. The plot showing comparison of hardness values of HT alloys.

Stress (σ) – Strain (ε) plot showing the RT mechanical behaviors of HT alloys under uniaxial tensile stresses is given in Figure 4.58. The yield strengths of the HT IN718-Y, IN718-YF, and IN718-YFH alloys were determined as 1045.5 ± 4.9, 1022.5 ± 5.0, and 1016.0 ± 5.7 MPa, respectively. Moreover, IN718-Y (~17.2%) and IN718-YFH (~18.9%) alloys showed higher ductility while IN718-YFH alloy showed relatively limited ductility of ~8.1% at RT. The yield strength of IN718 alloys after solutionizing and/or homogenization followed by double aging heat treatment is determined to range between ~1000 and ~1300 MPa with a ductility up to ~20% at

RT [113,236]. During aforementioned heat treatment route, detrimental phases dissolve in the matrix, and strengthening precipitates, γ' and γ", form in extensive number fractions. In this study, one-step heat treatment with a short duration was applied. BFTEM micrographs given in Figure 4.49 revealed the existence of γ" precipitate in HT microstructures of IN718-YF and IN718-YFH alloys. After HT1050 heat treatment, the fractions of strengthening precipitates are expected to be way less than the fractions obtained after homogenization and/or solutionizing followed by double aging heat treatment since the duration of heat treatment is 1h for this study while it exceeds ~17h for the other heat treatment routes [21]. Therefore, the strengths of HT alloys in this study are expected to be less than aforementioned samples even if the microstructure contains strengthening precipitate, γ". Despite the existences of Laves and carbide phases in high fractions and the existence of γ" in low fractions, HT alloys showed yield strengths as high as precipitation hardened IN718 alloys. Moreover, compared with the AB IN718-Y, IN718-YF, and IN718-YFH alloys, the increase of ~27%, ~19%, and ~18% in yield strength and the decrease of ~23%, ~7%, and ~20% in ductility was observed for HT IN718-Y, IN718-YF, and IN718-YFH alloys, respectively. Moreover, the decrease in yield strength was obtained in spite of increase in nano-particle content in HT alloys. It was determined that IN718-Y alloy had the highest yield strength. As a result, the existence of nano-particles enhanced tensile strengths of HT alloys with a negligible loss of ductility for IN718-YF alloy, and with a remarkable reduction in ductility for IN718-Y and IN718-YFH alloy.

At 700°C, the yield strengths of HT IN718-Y, IN718-YF and IN718-YFH alloys were determined as 910.5 ± 10.6, 771.3 ± 51.8, and 761.7 ± 26.7 MPa with ductility of ~14.3%, ~6% and ~2.8%, respectively. The plot showing tensile behaviors of HT IN718-Y, IN718-YF and IN718-YFH alloys at 700 °C is given in Figure 4.59. Also, the numerical values of tensile properties of HT IN718-Y, IN718-YF, and IN718-YFH alloys at RT and 700 °C are given in Table 4.12. Compared with AB tensile properties, the increases of ~6.4% and ~1.3% in yield strengths where the increase of ~36% and the decrease ~33% in ductility were obtained at 700 °C for HT IN718-

YF and IN718-YFH alloys, respectively. The higher amount of strengthening obtained for IN718-YF alloy is explained by the fact that the number density of NOs was calculated as 30 times of NO number density of IN718-YFH alloy. Compared with the RT tensile properties of HT alloys, the loss of strength was calculated as ~13%, ~25%, and ~25% for HT IN718-Y, IN718-YF, and IN718-YFH alloys, respectively. The decrease in ductility was calculated as ~17%, ~68%, and ~65% for IN718-Y, IN718-YF, and IN718-YFH alloys, respectively.

Compared with RT yield strengths, the loss of strength of IN718-Y alloy were less than IN718-YF and IN718-YFH alloys, so IN718-YF alloy showed higher mechanical stability than the other HT alloys. The particle size refinement and increase in number density of NOs (see Figure 4.49, Figure 4.51, and Figure 4.52) indicate the further formation of NOs rather than NO particle growth. In the literature, most of the in-situ tensile tests are conducted at 650 °C at which IN718 alloy starts to lose it strength due to dissolution and growth of strengthening precipitates, γ' and γ''. Trosch et al. [82] in their study on mechanical properties of SLM'ed IN718, they obtained the yield strength and ductility values of solution treated and double-aged HB IN718 alloy as ~870 MPa and ~3.6%, respectively. Moreover, McLouth et al. [229] in their study on dependence of high temperature ductility on temperature and strain rate of SLM'ed IN718 alloy, they applied HIP, solutionizing and double aging heat treatment to AB IN718 alloy. Then, the HT IN718 alloy was tested with different strain rates at 650 °C. The sample tested with 10^{-4} s^{-1} rate, which is close to the strain rate used in this study, showed ~856 MPa yield strength and ~2.9% ductility. At 750 °C and 10^{-4} s^{-1} strain rate, yield strength decreased drastically to ~647 MPa while the ductility was increased to ~3.4%. Compared with literature studies, similar yield strengths are observed with enhanced ductility for HT alloys even though number density of NOs and γ'' precipitates were way less than that they should be to gain effective strengthening [25,237,238]. Moreover, it should be noted that existence of grain boundary carbides, coarse irregular precipitates, and Laves phase has a detrimental effect on strength and ductility of the alloys.

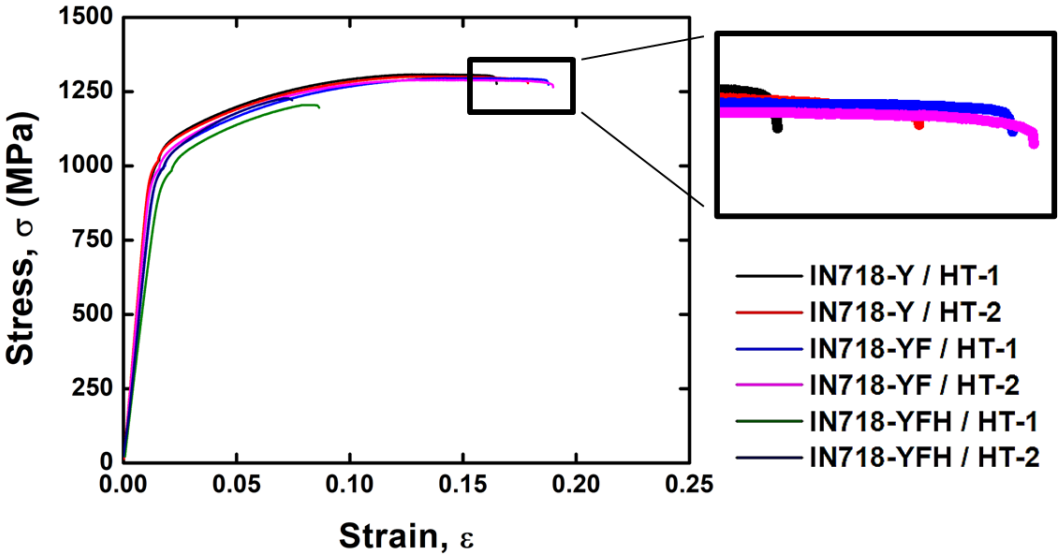

Figure 4.58. Stress-Strain curves of HT alloys tested at RT.

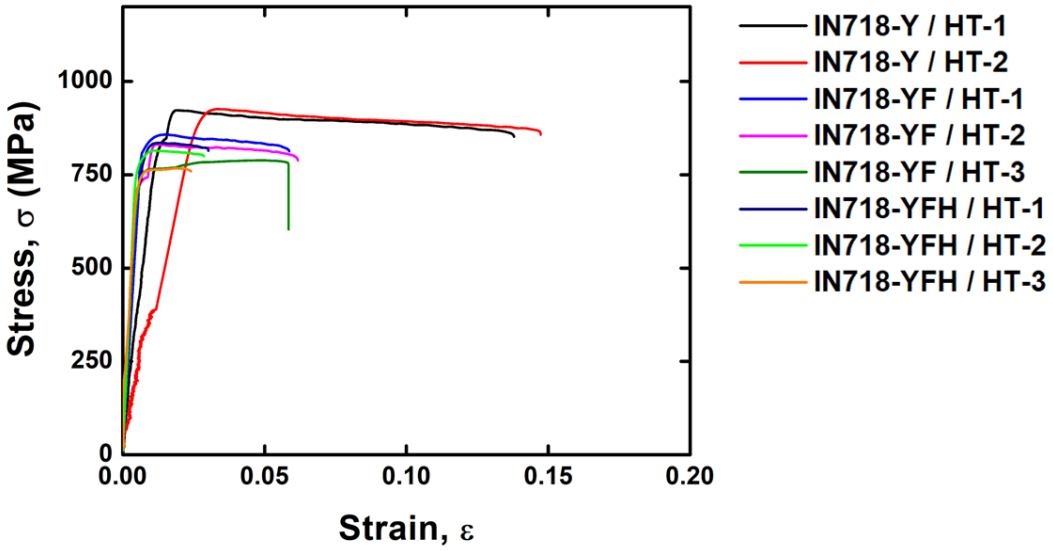

Figure 4.59. Stress-Strain curves of HT alloys tested at 700 °C.

Table 4.12. Tensile properties of HT samples tested at RT and 700 °C.

Sample	T (°C)	Elastic Modulus (E)	Yield Strength (MPa)	Tensile Strength (MPa)	Strain at Fracture (%)
IN718-Y	RT	211 ± 8.5	1045.5 ± 4.9	1304.5 ± 5.0	17.2 ± 1.0
IN718-Y	700	89.0 ± 29.7	910.5 ± 10.6	924.5 ± 2.1	14.3 ± 0.6
IN718-YF	RT	210.0 ± 4.3	1022.5 ± 5.0	1292.0 ± 4.2	18.9 ± 0.1
IN718-YF	700	142.0 ± 15.4	771.3 ± 51.8	826.0 ± 34.8	6.0 ± 0.2
IN718-YFH	RT	204.0 ± 1.4	1016.0 ± 5.7	1216.5 ± 16.3	8.1 ± 0.9
IN718-YFH	700	154.3 ± 22.3	761.7 ± 26.7	803.0 ± 40.4	2.8 ± 0.3

CHAPTER 5

CONCLUSION

In this study, IN718 superalloy is strengthened by Y-Ti-(Al)-O and Y-Hf-(Ti)-(Al)-O oxide dispersoids. Three different ODS IN718 alloys were produced by SLM method and then heat treatment was applied to improve alloy properties. The alloys were named as "IN718-Y (IN718 – Y_2O_3)", "IN718-YF (IN718 – Y_2O_3 – FeO)", and "IN718 – YFH (IN718 – Y_2O_3 – FeO – Hf)". The aim was to promote formation of Y-Ti-O (for IN718-Y and IN718-YF alloys) and Y-Hf-O (for IN718-YFH) NOs in the IN718 matrix to enhance the tensile strength of IN718 alloy at elevated temperatures at which the strength of the alloy starts to degrade due to lack of strengthening precipitates, γ' and γ''. Moreover, the heat treatment was applied to ODS alloys to increase number densities of NOs and solutionize/homogenize the microstructure. Based on the microstructural and mechanical characterizations of AB and HT ODS alloy, following conclusions can be drawn for this study:

1- Experimental results are highly consistent with the thermochemical calculations except the oxides consist of more than three components. During SLM processing, a product is exposed to rapid heating and cooling cycles with high thermal gradients up to ~10^6 K/s that causes the non-equilibrium microstructure. Thermochemical calculations predicted the non-equilibrium phases with high precision, meaning that the CALPHAD method can be used to predict AB microstructures of alloys produced by SLM technique.
2- For SLM production, it is essential to carry out the process with spherical powders having specified sizes. In literature, mechanical alloying for longer than 20h with grinding balls is recommended to obtain effective strengthening for ODS alloys. However, the particle shape is lost and the size distribution is distorted at the end of mechanical alloying process. So, in this study, the mechanical mixing was applied to ODS alloy mixtures. To

optimize the duration of mechanical mixing process without grinding balls, the mechanical mixing process was applied for different time periods. After mechanical mixing for 10 min, the sphericity and initial powder size were preserved. Also, mechanical bonding between oxide/oxide formers and IN718 powders was provided. Therefore, mechanical mixing for 10 min without grinding balls was found as optimum mixing process in terms of preserving powder characteristics and time saving.

3- With SLM process parameters of 220 W – 960 mm/s for IN718-Y and 350 W – 750 mm/s for IN718-YF & IN718-YFH alloys, the products with higher than 99.7% densification were produced. Power has a predominant role in porosity formation rather than velocity. Increasing oxide/oxide former fraction resulted in the requirement of the use of higher power values to obtain almost fully dense products.

4- The existence of coarse sized and irregular shaped particles was observed for all the grades in AB condition. Additionally, existence of Laves phase and different carbide phases was detected. Although they are detrimental for mechanical properties, alloys showed higher strengths than IN718 alloy, which indicates the strengthening was provided successfully.

5- All the grades have shown almost random texture in AB and in HT conditions. In AB condition, none of the grades have shown directional growth in preferred orientation. The same phenomenon was valid for HT IN718-YF and HT IN718-YFH alloys. Only HT IN718-Y alloy showed epitaxial growth in preferred direction of (001).

6- Heat treatment route was found successful for improvement of number density of nanoparticles. However, the existence of Laves phase and carbides was detected for all the grades in HT condition, which indicates inefficiency of heat treatment for dissolution of detrimental phases. Thus, the application of heat treatment at a higher temperature would enhance the strength and ductility of each HT alloy by dissolution of grain boundary carbides and

Laves phase combined with increase in number density of NOs and strengthening precipitates.

7- Compared with heat treated IN718 alloy, HT IN718-Y, IN718-YF, and IN718-YFH alloys showed higher strengths in spite of the existence of detrimental phases. So, IN718-Y, IN718-YF, and IN718-YFH alloys were found to be feasible for the use of applications with service temperatures of 700 °C.

8- For all grades in both AB and HT conditions, less amount of strengthening than anticipated. The spherical particles observed in BFTEM micrographs were assumed to be NOs because of their shape for number density analyses. However, some of these particles were identified as Laves phase, carbides, and α-Cr phases which are detrimental for mechanical properties. Therefore, the actual NO number densities are assumed to be lower than the calculated values which explains observations of lower strengths than anticipated.

REFERENCES

[1] M.J. Donachie, S.James. Donachie, Superalloys: A Technical Guide, ASM International, 2002.

[2] J.R. Davis, ASM Specialty Handbook: Nickel, Cobalt, and Their Alloys, ASM International, 2000.

[3] R.C. (Roger C. Reed, The Superalloys: Fundamentals and Applications, Cambridge University Press, 2006.

[4] B. Geddes, H. Leon, X. Huang, Superalloys: Alloying and Performance, ASM International, 2010. http://books.google.ca/books/about/Superalloys.html?id=UCiHLGu4uGUC&pgis=1 (accessed December 15, 2022).

[5] J.K. Tien, Thomas. Caulfield, Superalloys, Supercomposites, and Superceramics, Academic Press, 1989.

[6] B. Zhang, P. Wang, Y. Chew, Y. Wen, M. Zhang, P. Wang, G. Bi, J. Wei, Mechanical properties and microstructure evolution of selective laser melting Inconel 718 along building direction and sectional dimension, Materials Science and Engineering A. 794 (2020). https://doi.org/10.1016/j.msea.2020.139941.

[7] M. Shahwaz, P. Nath, I. Sen, A critical review on the microstructure and mechanical properties correlation of additively manufactured nickel-based superalloys, J Alloys Compd. 907 (2022). https://doi.org/10.1016/j.jallcom.2022.164530.

[8] M.F. Moreira, L.B. Fantin, F. Beneduce Neto, C.R.F. Azevedo, Microstructural and mechanical characterization of as-cast nickel-based superalloy (IN-713C), International Journal of Metalcasting. 15 (2021) 1129–1148. https://doi.org/10.1007/s40962-020-00540-0.

[9] G. Liu, X. Xiao, M. Véron, S. Birosca, The nucleation and growth of η phase in nickel-based superalloy during long-term thermal exposure, Acta Mater. 185 (2020) 493–506. https://doi.org/10.1016/j.actamat.2019.12.038.

[10] M. Durand-Charre, The Microstructure of Superalloys, Routledge, 2017. https://doi.org/10.1201/9780203736388.

[11] N. Volz, C.H. Zenk, R. Cherukuri, T. Kalfhaus, M. Weiser, S.K. Makineni, C. Betzing, M. Lenz, B. Gault, S.G. Fries, J. Schreuer, R. Vaßen, S. Virtanen, D. Raabe, E. Spiecker, S. Neumeier, M. Göken, Thermophysical and mechanical properties of advanced single crystalline co-base superalloys, Metall Mater Trans A Phys Metall Mater Sci. 49 (2018) 4099–4109. https://doi.org/10.1007/s11661-018-4705-1.

[12] A. Kracke, Superalloys, the most successful alloy system of modern times - past, present, and future, 2016.

[13] M.M. de Oliveira, A.A. Couto, G.F.C. Almeida, D.A.P. Reis, N.B. de Lima, R. Baldan, Mechanical behavior of Inconel 625 at elevated temperatures, Metals (Basel). 9 (2019). https://doi.org/10.3390/met9030301.

[14] A.P. Mouritz, Introduction to Aerospace Materials, Woodhead Publishing Limited, 2012.

[15] N. Eswara, P.R.J.H. Wanhill, Aerospace Materials and Material Technologies - Volume 1: Aerospace Materials, Springer, 2017. http://www.springer.com/series/15453.

[16] T.M. Pollock, S. Tin, Nickel-based superalloys for advanced turbine engines: chemistry, microstructure, and properties, J Propuls Power. 22 (2006) 361–374. https://doi.org/10.2514/1.18239.

[17] J.R. Davis, ASM Specialty Handbook: Heat-Resistant Materials, ASM International, 1999.

[18] M.C. Hardy, M. Detrois, E.T. McDevitt, C. Argyrakis, V. Saraf, P.D. Jablonski, J.A. Hawk, R.C. Buckingham, H.S. Kitaguchi, S. Tin, Solving recent challenges for wrought ni-base superalloys, Metall Mater Trans A Phys Metall Mater Sci. 51 (2020) 2626–2650. https://doi.org/10.1007/s11661-020-05773-6.

[19] J.R. (Joseph R.) Davis, Alloying: Understanding the Basics, ASM International, 2001.

[20] H. Wu, X. Zhuang, Y. Nie, Y. Li, L. Jiang, Effect of heat treatment on mechanical property and microstructure of a powder metallurgy nickel-based superalloy, Materials Science and Engineering A. 754 (2019) 29–37. https://doi.org/10.1016/j.msea.2019.03.064.

[21] X. Li, J.J. Shi, C.H. Wang, G.H. Cao, A.M. Russell, Z.J. Zhou, C.P. Li, G.F. Chen, Effect of heat treatment on microstructure evolution of Inconel 718 alloy fabricated by selective laser melting, J Alloys Compd. 764 (2018) 639–649. https://doi.org/10.1016/j.jallcom.2018.06.112.

[22] Ł. Rakoczy, B. Rutkowski, M. Grudzień-Rakoczy, R. Cygan, W. Ratuszek, A. Zielińska-Lipiec, Analysis of γ′ precipitates, carbides and nano-borides in heat-treated ni-based superalloy using SEM, STEM-EDX, and HRSTEM, Materials. 13 (2020) 1–24. https://doi.org/10.3390/ma13194452.

[23] G.H. Cao, T.Y. Sun, C.H. Wang, X. Li, M. Liu, Z.X. Zhang, P.F. Hu, A.M. Russell, R. Schneider, D. Gerthsen, Z.J. Zhou, C.P. Li, G.F. Chen, Investigations of γ′ γ″ and δ precipitates in heat-treated Inconel 718 alloy fabricated by selective laser melting, Mater Charact. 136 (2018) 398–406. https://doi.org/10.1016/j.matchar.2018.01.006.

[24] S. Mahadevan, S. Nalawade, J.B. Singh, A. Verma, B. Paul, K. Ramaswamy, Evolution of delta phase microstructure in Alloy 718, in: 7th International Symposium on Superalloy 718 and Derivatives, TMS (The Minerals, Metals & Materials Society), 2010.

[25] H. Qin, Z. Bi, H. Yu, G. Feng, J. Du, J. Zhang, Influence of stress on γ″ precipitation behavior in Inconel 718 during aging, J Alloys Compd. 740 (2018) 997–1006. https://doi.org/10.1016/j.jallcom.2018.01.030.

[26] T. Wittenzellner, S. Sumarli, H. Schaar, F. Wang, D. Ma, A. Bührig-Polaczek, Microstructural investigations of ni-based superalloys by directional solidification quenching technique, Materials. 13 (2020). https://doi.org/10.3390/MA13194265.

[27] H.P. Zhang, J.M. Bai, X.K. Li, X.Y. Li, J. Jia, J.T. Liu, Y.W. Zhang, Effect of hafnium and tantalum on the microstructure of PM ni-based superalloys, J Mater Sci. 57 (2022) 6803–6818. https://doi.org/10.1007/s10853-022-07052-8.

[28] X. Dong, X. Zhang, K. Du, Y. Zhou, T. Jin, H. Ye, Microstructure of carbides at grain boundaries in nickel based superalloys, J. Mater. Sci. Technol. 28 (2012) 1031–1038.

[29] X. Xiang, Z. Yao, J. Dong, L. Sun, Dissolution behavior of intragranular M23C6 carbide in 617B ni-base superalloy during long-term aging, J Alloys Compd. 787 (2019) 216–228. https://doi.org/10.1016/j.jallcom.2019.01.389.

[30] M. Smith, L. Bichler, J. Gholipour, P. Wanjara, Mechanical properties and microstructural evolution of in-service Inconel 718 superalloy repaired by linear friction welding, International Journal of Advanced Manufacturing Technology. 90 (2017) 1931–1946. https://doi.org/10.1007/s00170-016-9515-2.

[31] P. Hoier, A. Malakizadi, P. Stuppa, S. Cedergren, U. Klement, Microstructural characteristics of Alloy 718 and Waspaloy and their influence on flank wear during turning, Wear. 400–401 (2018) 184–193. https://doi.org/10.1016/j.wear.2018.01.011.

[32] G.A. Rao, M. Kumar, M. Srinivas, D.S. Sarma, Effect of standard heat treatment on the microstructure and mechanical properties of hot isostatically

pressed superalloy Inconel 718, Materials Science and Engineering A. 355 (2003) 114–125. https://doi.org/10.1016/S0921-5093(03)00079-0.

[33] X. Song, Y. Wang, X. Zhao, J. Zhang, Y. Li, Y. Wang, Z. Chen, Analysis of carbide transformation in MC-M23C6 and its effect on mechanical properties of ni-based superalloy, J Alloys Compd. 911 (2022). https://doi.org/10.1016/j.jallcom.2022.164959.

[34] D.I. Davidov, N. v. Kazantseva, N.I. Vinogradova, I. v. Ezhov, Study of the structure and chemical composition of the protective coating of a fist stage gas turbine blade after regenerative heat treatment, in: IOP Conf Ser Mater Sci Eng, Institute of Physics Publishing, 2018. https://doi.org/10.1088/1757-899X/286/1/012007.

[35] D.I. Davidov, N.V. Kazantseva, N.I. Vinogradova, I.V. Ezhov, N.N. Stepanova, Analysis of the grain boundary microstructure and degradation in a gas turbine blade, in: Material Science Nonequilibrium Phase Transformations, 2017: pp. 26–29.

[36] L. Xiao, Z. Peng, X. Zhao, X. Tu, Z. Cai, Q. Zhong, S. Wang, H. Yu, Microstructure and mechanical properties of crack-free ni-based GH3536 superalloy fabricated by laser solid forming, J Alloys Compd. 921 (2022). https://doi.org/10.1016/j.jallcom.2022.165950.

[37] T. Xia, R. Wang, Z. Bi, R. Wang, P. Zhang, G. Sun, J. Zhang, Microstructure and mechanical properties of carbides reinforced nickel matrix alloy prepared by selective laser melting, Materials. 14 (2021). https://doi.org/10.3390/ma14174792.

[38] A. Mashhuriazar, C. Hakan Gur, Z. Sajuri, H. Omidvar, Effects of heat input on metallurgical behavior in HAZ of multi-pass and multi-layer welded IN-939 superalloy, Journal of Materials Research and Technology. 15 (2021) 1590–1603. https://doi.org/10.1016/j.jmrt.2021.08.113.

[39] P. Kontis, H.A.M. Yusof, S. Pedrazzini, M. Danaie, K.L. Moore, P.A.J. Bagot, M.P. Moody, C.R.M. Grovenor, R.C. Reed, On the effect of boron on grain boundary character in a new polycrystalline superalloy, Acta Mater. 103 (2016) 688–699. https://doi.org/10.1016/j.actamat.2015.10.006.

[40] R. Gupta, K.C.H. Kumar, M.J.N.V. Prasad, P. Pant, Compositionally graded nano-sized borides in a directionally solidified nickel-base superalloy, Scr Mater. 201 (2021). https://doi.org/10.1016/j.scriptamat.2021.113981.

[41] P.J. Zhou, J.J. Yu, X.F. Sun, H.R. Guan, Z.Q. Hu, The role of boron on a conventional nickel-based superalloy, Materials Science and Engineering A. 491 (2008) 159–163. https://doi.org/10.1016/j.msea.2008.02.019.

[42] A.M. da Silva Costa, C.A. Nunes, R. Baldan, G.C. Coelho, Thermodynamic evaluation of the phase stability and microstructural characterization of a cast B1914 superalloy, J Mater Eng Perform. 23 (2014) 819–825. https://doi.org/10.1007/s11665-013-0814-6.

[43] C. Pauzon, A. Markström, S.D. le Goff, E. Hryha, Effect of the process atmosphere composition on alloy 718 produced by laser powder bed fusion, Metals (Basel). 11 (2021). https://doi.org/10.3390/met11081254.

[44] J.S. Zuback, A.D. Iams, F. Zhang, L.A. Giannuzzi, T.A. Palmer, Stable nitride precipitation in additively manufactured nickel superalloys, J Alloys Compd. 910 (2022). https://doi.org/10.1016/j.jallcom.2022.164918.

[45] A. Mitchell, S.L. Cockcroft, C.E. Schvezov, A.J. Schmalz, J.-N. Loquet, J. Fernihough, Primary carbide and nitride precipitation in superalloys containing niobium, High Temperature Materials and Processes. 15 (1996) 27–40.

[46] Y. Zhang, Z. Li, P. Nie, Y. Wu, Carbide and nitride precipitation during laser cladding of Inconel 718 alloy coatings, Opt Laser Technol. 52 (2013) 30–36. https://doi.org/10.1016/j.optlastec.2013.03.023.

[47] D. Texier, J.C. Stinville, M.P. Echlin, S. Pierret, P. Villechaise, T.M. Pollock, J. Cormier, Short crack propagation from cracked non-metallic inclusions in a ni-based polycrystalline superalloy, Acta Mater. 165 (2019) 241–258. https://doi.org/10.1016/j.actamat.2018.11.051.

[48] L. Xue, J. Wang, L. Li, G. Chen, L. Sun, S. Yu, Enhancement of wear and erosion-corrosion resistance of Inconel 718 alloy by liquid nitriding, Mater Res Express. 7 (2020). https://doi.org/10.1088/2053-1591/abb426.

[49] S. Kathiravan, G.S. Kaliaraj, A.M. Kamalan Kirubaharan, R.R. Kumar, Study of oxide layer formation on Inconel 718 during isothermal oxidation between 800 °C to 1200 °C in hot air, Ceram Int. (2022). https://doi.org/10.1016/j.ceramint.2022.07.187.

[50] Z. Zhu, Y. Li, C. Ma, X. Liu, G. Liu, S. Wang, H. Xu, N. Zhang, The corrosion behavior of nickel-based alloy Inconel 740 H in supercritical water, Corros Sci. 192 (2021). https://doi.org/10.1016/j.corsci.2021.109848.

[51] A.M. de Sousa Malafaia, R.B. de Oliveira, L. Latu-Romain, Y. Wouters, R. Baldan, Isothermal oxidation of Inconel 625 superalloy at 800 and 1000 °C: Microstructure and oxide layer characterization, Mater Charact. 161 (2020). https://doi.org/10.1016/j.matchar.2020.110160.

[52] Y.N. Zhang, X. Cao, P. Wanjara, M. Medraj, Oxide films in laser additive manufactured Inconel 718, Acta Mater. 61 (2013) 6562–6576. https://doi.org/10.1016/j.actamat.2013.07.039.

[53] K.D. Ramkumar, S.S. Mulimani, K. Ankit, A. Kothari, S. Ganguly, Effect of grain boundary precipitation on the mechanical integrity of EBW joints of Inconel 625, Materials Science and Engineering A. 808 (2021). https://doi.org/10.1016/j.msea.2021.140926.

[54] N. Kazantseva, D. Davidov, N. Vinogradova, I. Ezhov, N. Stepanova, Analysis of phase transformations in Inconel 738C alloy after regenerative

heat treatment, in: IOP Conf Ser Mater Sci Eng, Institute of Physics Publishing, 2018. https://doi.org/10.1088/1757-899X/324/1/012001.

[55] R. Krishna, S. v. Hainsworth, S.P.A. Gill, A. Strang, H. v. Atkinson, Topologically close-packed μ phase precipitation in creep-exposed Inconel 617 alloy, Metall Mater Trans A Phys Metall Mater Sci. 44 (2013) 1419–1429. https://doi.org/10.1007/s11661-012-1491-z.

[56] H. Jiang, J. Dong, M. Zhang, The characteristics of μ phase precipitated during 720 °C long-term aging in alloy 617B, Journal of Materials Research and Technology. 8 (2019) 2461–2465. https://doi.org/10.1016/j.jmrt.2018.11.006.

[57] X. Yu, X. Lin, F. Liu, L. Wang, Y. Tang, J. Li, S. Zhang, W. Huang, Influence of post-heat-treatment on the microstructure and fracture toughness properties of Inconel 718 fabricated with laser directed energy deposition additive manufacturing, Materials Science and Engineering A. 798 (2020). https://doi.org/10.1016/j.msea.2020.140092.

[58] E. Chlebus, K. Gruber, B. Kuźnicka, J. Kurzac, T. Kurzynowski, Effect of heat treatment on the microstructure and mechanical properties of Inconel 718 processed by selective laser melting, Materials Science and Engineering A. 639 (2015) 647–655. https://doi.org/10.1016/j.msea.2015.05.035.

[59] E.L. Stevens, J. Toman, A.C. To, M. Chmielus, Variation of hardness, microstructure, and Laves phase distribution in direct laser deposited alloy 718 cuboids, Mater Des. 119 (2017) 188–198. https://doi.org/10.1016/j.matdes.2017.01.031.

[60] Y. Zhao, K. Guan, Z. Yang, Z. Hu, Z. Qian, H. Wang, Z. Ma, The effect of subsequent heat treatment on the evolution behavior of second phase particles and mechanical properties of the Inconel 718 superalloy manufactured by selective laser melting, Materials Science and Engineering A. 794 (2020). https://doi.org/10.1016/j.msea.2020.139931.

[61] F. Liu, F. Lyu, F. Liu, X. Lin, C. Huang, Laves phase control of Inconel 718 superalloy fabricated by laser direct energy deposition via δ aging and solution treatment, Journal of Materials Research and Technology. 9 (2020) 9753–9765. https://doi.org/10.1016/j.jmrt.2020.06.061.

[62] R. Darolia, Development of strong, oxidation and corrosion resistant nickel-based superalloys: critical review of challenges, progress and prospects, International Materials Reviews. 64 (2019) 355–380. https://doi.org/10.1080/09506608.2018.1516713.

[63] S.-H. Chen, Y.-L. Ho, Lifespan of super-alloy Waspaloy cutting tools, (2019). https://doi.org/10.1016/j.heliyon.2019.

[64] X. Lv, F. Sun, J. Tong, Q. Feng, J. Zhang, Paired dislocations and their interactions with γ′ particles in polycrystalline superalloy GH4037, J Mater Eng Perform. 24 (2015) 143–148. https://doi.org/10.1007/s11665-014-1307-y.

[65] Y. Han, P. Deb, M.C. Chatuverdi, Coarsening behavior of γ" and γ’ particles in Inconel alloy 718, Metal Science. 16 (1982) 555–561. https://doi.org/10.1179/030634582790427118.

[66] A. Behera, Advanced Materials: An Introduction to Modern Materials Science, Springer International Publishing, Cham, 2022. https://doi.org/10.1007/978-3-030-80359-9.

[67] A.J. Goodfellow, Strengthening mechanisms in polycrystalline nickel-based superalloys, Materials Science and Technology (United Kingdom). 34 (2018) 1793–1808. https://doi.org/10.1080/02670836.2018.1461594.

[68] M.T. Jovanović, B. Lukić, Z. Mišković, Processing and some applications of nickel, cobalt and titanium-based alloys, Metalurgija-Journal of Metallurgy. 13 (2007) 91–106.

[69] F. Zupanic, T. Boncina, A. Krizman, F.D. Tichelaar, Structure of continuously cast ni-based superalloy Inconel 713C, 2001. www.elsevier.com/locate/jallcom.

[70] S. Barella, A. Gruttadauria, C. Mapelli, D. Mombelli, P. Taiana, M. Bosatra, A. Morini, Solidification microstructure of centrifugally cast Inconel 625, China Foundry. 14 (2017) 304–312. https://doi.org/10.1007/s41230-017-7017-y.

[71] Y. Zhao, K. Li, M. Gargani, W. Xiong, A comparative analysis of Inconel 718 made by additive manufacturing and suction casting: Microstructure evolution in homogenization, Addit Manuf. 36 (2020). https://doi.org/10.1016/j.addma.2020.101404.

[72] F. Soffel, D. Eisenbarth, E. Hosseini, K. Wegener, Interface strength and mechanical properties of Inconel 718 processed sequentially by casting, milling, and direct metal deposition, J Mater Process Technol. 291 (2021). https://doi.org/10.1016/j.jmatprotec.2020.117021.

[73] R.P. Silva, R. Soares, R. Neto, A. Reis, R. Paiva, R. Madureira, J. Silva, Grain refinement of Inconel 718 superalloy - The effect of rotating magnetic field, Materials. 15 (2022). https://doi.org/10.3390/ma15062038.

[74] W. Wang, C. Zhu, J. Zeng, C. Lu, H. Qian, H. Xu, P. Lyu, Microstructures and Nb-rich precipitation behaviors of Inconel 718 superalloy under sub-rapid solidification process, Metall Mater Trans A Phys Metall Mater Sci. 51 (2020) 2306–2317. https://doi.org/10.1007/s11661-020-05696-2.

[75] X. Zhang, F. Liou, Introduction to additive manufacturing, in: Addit Manuf, Elsevier, 2021: pp. 1–31. https://doi.org/10.1016/B978-0-12-818411-0.00009-4.

[76] A. Badiru, V. Valencia, D. Liu, Additive Manufacturing Handbook - Product Development for Defense Industry, CRC Press, 2017.

[77] M. Yakout, M.A. Elbestawi, S.C. Veldhuis, A review of metal additive manufacturing technologies, Solid State Phenomena. 278 SSP (2018) 1–14. https://doi.org/10.4028/www.scientific.net/SSP.278.1.

[78] ISO/ASTM 52900:2021(E), Standard Terminology for Additive Manufacturing - General Principles - Terminology, 2021. https://www.iso.org/obp.

[79] B. Graybill, M. Li, D. Malawey, C. Ma, J.M. Alvarado-Orozco, E. Martinez-Franco, Additive manufacturing of nickel-based superalloys, ASME 2018 13th International Manufacturing Science and Engineering Conference, MSEC 2018. 1 (2018). https://doi.org/10.1115/MSEC2018-6666.

[80] J.R. Hwang, J.Y. Zheng, P.C. Kuo, C.D. Huang, C.P. Fung, Process optimization of Inconel 718 alloy produced by laser powder bed fusion, Metals (Basel). 12 (2022). https://doi.org/10.3390/met12091494.

[81] D. Zhang, Z. Feng, C. Wang, W. Wang, Z. Liu, W. Niu, Comparison of microstructures and mechanical properties of Inconel 718 alloy processed by selective laser melting and casting, Materials Science and Engineering A. 724 (2018) 357–367. https://doi.org/10.1016/j.msea.2018.03.073.

[82] T. Trosch, J. Strößner, R. Völkl, U. Glatzel, Microstructure and mechanical properties of selective laser melted Inconel 718 compared to forging and casting, Mater Lett. 164 (2016) 428–431. https://doi.org/10.1016/j.matlet.2015.10.136.

[83] S.S. Babu, N. Raghavan, J. Raplee, S.J. Foster, C. Frederick, M. Haines, R. Dinwiddie, M.K. Kirka, A. Plotkowski, Y. Lee, R.R. Dehoff, Additive manufacturing of nickel superalloys: Opportunities for innovation and challenges related to qualification, Metall Mater Trans A Phys Metall Mater Sci. 49 (2018) 3764–3780. https://doi.org/10.1007/s11661-018-4702-4.

[84] S. Sanchez, P. Smith, Z. Xu, G. Gaspard, C.J. Hyde, W.W. Wits, I.A. Ashcroft, H. Chen, A.T. Clare, Powder bed fusion of nickel-based

superalloys: A review, Int J Mach Tools Manuf. 165 (2021). https://doi.org/10.1016/j.ijmachtools.2021.103729.

[85] C.Y. Yap, C.K. Chua, Z.L. Dong, Z.H. Liu, D.Q. Zhang, L.E. Loh, S.L. Sing, Review of selective laser melting: Materials and applications, Appl Phys Rev. 2 (2015). https://doi.org/10.1063/1.4935926.

[86] L. Jiao, Z.Y. Chua, S.K. Moon, J. Song, G. Bi, H. Zheng, Femtosecond laser produced hydrophobic hierarchical structures on additive manufacturing parts, Nanomaterials. 8 (2018). https://doi.org/10.3390/nano8080601.

[87] X. Wang, K. Chou, Effects of thermal cycles on the microstructure evolution of Inconel 718 during selective laser melting process, Addit Manuf. 18 (2017) 1–14. https://doi.org/10.1016/j.addma.2017.08.016.

[88] H. Wang, L. Wang, R. Cui, B. Wang, L. Luo, Y. Su, Differences in microstructure and nano-hardness of selective laser melted Inconel 718 single tracks under various melting modes of molten pool, Journal of Materials Research and Technology. 9 (2020) 10401–10410. https://doi.org/10.1016/j.jmrt.2020.07.029.

[89] I. Serrano-Munoz, T. Mishurova, T. Thiede, M. Sprengel, A. Kromm, N. Nadammal, G. Nolze, R. Saliwan-Neumann, A. Evans, G. Bruno, The residual stress in as-built laser powder bed fusion IN718 alloy as a consequence of the scanning strategy induced microstructure, Sci Rep. 10 (2020) 1–15. https://doi.org/10.1038/s41598-020-71112-9.

[90] R. Priya Parida, V. Senthilkumar, Experimental studies of defect generation in selective laser melted Inconel 718 alloy, in: Mater Today Proc, Elsevier Ltd, 2020: pp. 1372–1377. https://doi.org/10.1016/j.matpr.2020.04.698.

[91] M.M. Attallah, R. Jennings, X. Wang, L.N. Carter, Additive manufacturing of ni-based superalloys: The outstanding issues, MRS Bull. 41 (2016) 758–764. https://doi.org/10.1557/mrs.2016.211.

[92] H. Nadiyadi, H. Gajera, R. Bidajwala, K. Abhisek, K. Dave, Effects of powder bed fusion process parameters on hardness for Inconel 718, in: Mater Today Proc, Elsevier Ltd, 2020: pp. 2275–2280. https://doi.org/10.1016/j.matpr.2020.06.388.

[93] D.S. Watring, J.T. Benzing, N. Hrabe, A.D. Spear, Effects of laser-energy density and build orientation on the structure–property relationships in as-built Inconel 718 manufactured by laser powder bed fusion, Addit Manuf. 36 (2020). https://doi.org/10.1016/j.addma.2020.101425.

[94] X. Wang, X. Gong, K. Chou, Review on powder-bed laser additive manufacturing of Inconel 718 parts, Proc Inst Mech Eng B J Eng Manuf. 231 (2017) 1890–1903. https://doi.org/10.1177/0954405415619883.

[95] M. Balbaa, S. Mekhiel, M. Elbestawi, J. McIsaac, On selective laser melting of Inconel 718: Densification, surface roughness, and residual stresses, Mater Des. 193 (2020). https://doi.org/10.1016/j.matdes.2020.108818.

[96] D. Gu, M. Xia, D. Dai, On the role of powder flow behavior in fluid thermodynamics and laser processability of ni-based composites by selective laser melting, Int J Mach Tools Manuf. 137 (2019) 67–78. https://doi.org/10.1016/j.ijmachtools.2018.10.006.

[97] L. Cordova, M. Campos, T. Tinga, Revealing the effects of powder reuse for selective laser melting by powder characterization, JOM. 71 (2019) 1062–1072. https://doi.org/10.1007/s11837-018-3305-2.

[98] M.C. Karia, M.A. Popat, K.B. Sangani, Selective laser melting of Inconel super alloy-a review, in: AIP Conf Proc, American Institute of Physics Inc., 2017. https://doi.org/10.1063/1.4990166.

[99] P. Tao, H. Li, B. Huang, Q. Hu, S. Gong, Q. Xu, The crystal growth, intercellular spacing and microsegregation of selective laser melted Inconel 718 superalloy, Vacuum. 159 (2019) 382–390. https://doi.org/10.1016/j.vacuum.2018.10.074.

[100] K. yun Feng, P. Liu, H. xue Li, S. yu Sun, S. bo Xu, J. ning Li, Microstructure and phase transformation on the surface of Inconel 718 alloys fabricated by SLM under 1050°C solid solution + double ageing, Vacuum. 145 (2017) 112–115. https://doi.org/10.1016/j.vacuum.2017.08.044.

[101] W. Huang, J. Yang, H. Yang, G. Jing, Z. Wang, X. Zeng, Heat treatment of Inconel 718 produced by selective laser melting: Microstructure and mechanical properties, Materials Science and Engineering A. 750 (2019) 98–107. https://doi.org/10.1016/j.msea.2019.02.046.

[102] D. Zhang, W. Niu, X. Cao, Z. Liu, Effect of standard heat treatment on the microstructure and mechanical properties of selective laser melting manufactured Inconel 718 superalloy, Materials Science and Engineering A. 644 (2015) 32–40. https://doi.org/10.1016/j.msea.2015.06.021.

[103] K. Moussaoui, W. Rubio, M. Mousseigne, T. Sultan, F. Rezai, Effects of selective laser melting additive manufacturing parameters of Inconel 718 on porosity, microstructure and mechanical properties, Materials Science and Engineering A. 735 (2018) 182–190. https://doi.org/10.1016/j.msea.2018.08.037.

[104] L. Yang, K. Hsu, B. Baughman, D. Godfrey, F. Medina, M. Menon, S. Wiener, Additive Manufacturing of Metals: The Technology, Materials, Design and Production, Springer Series in Advanced Manufacturing, 2017. http://www.springer.com/series/7113.

[105] I. Gibson, D. Rosen, B. Stucker, Additive Manufacturing Technologies: 3D Printing, Rapid Prototyping, and Direct Digital Manufacturing, Second edition, 2015. https://doi.org/10.1007/978-1-4939-2113-3.

[106] P.K. Gokuldoss, S. Kolla, J. Eckert, Additive manufacturing processes: Selective laser melting, electron beam melting and binder jetting-selection guidelines, Materials. 10 (2017). https://doi.org/10.3390/ma10060672.

[107] L.E. Murr, S.M. Gaytan, D.A. Ramirez, E. Martinez, J. Hernandez, K.N. Amato, P.W. Shindo, F.R. Medina, R.B. Wicker, Metal fabrication by additive manufacturing using laser and electron beam melting technologies, J. Mater. Sci. Technol. 28 (2012) 1–14.

[108] A.R. Balachandramurthi, J. Moverare, S. Mahade, R. Pederson, Additive manufacturing of alloy 718 via electron beam melting: Effect of post-treatment on the microstructure and the mechanical properties, Materials. 12 (2018). https://doi.org/10.3390/ma12010068.

[109] H.J. Lee, H.K. Kim, H.U. Hong, B.S. Lee, Influence of the focus offset on the defects, microstructure, and mechanical properties of an Inconel 718 superalloy fabricated by electron beam additive manufacturing, J Alloys Compd. 781 (2019) 842–856. https://doi.org/10.1016/j.jallcom.2018.12.070.

[110] S.H. Sun, Y. Koizumi, T. Saito, K. Yamanaka, Y.P. Li, Y. Cui, A. Chiba, Electron beam additive manufacturing of Inconel 718 alloy rods: Impact of build direction on microstructure and high-temperature tensile properties, Addit Manuf. 23 (2018) 457–470. https://doi.org/10.1016/j.addma.2018.08.017.

[111] SAE International - Aerospace Materials Systems, AMS 5662 - Nickel Alloy, Corrosion and Heat-Resistant, Bars, Forgings, and Rings 52.5Ni - 19Cr - 3.0Mo - 5.1Cb (Nb) - 0.90Ti - 0.50AI - 18Fe Consumable Electrode or Vacuum Induction Melted 1775 °F (968 °C) Solution Heat Treated, Precipitation-Hardenable - UNS N07718, 2016.

[112] A. Thomas, M. El-Wahabi, J.M. Cabrera, J.M. Prado, High temperature deformation of Inconel 718, J Mater Process Technol. 177 (2006) 469–472. https://doi.org/10.1016/j.jmatprotec.2006.04.072.

[113] E. Hosseini, V.A. Popovich, A review of mechanical properties of additively manufactured Inconel 718, Addit Manuf. 30 (2019) 100877. https://doi.org/10.1016/j.addma.2019.100877.

[114] Q. Jia, D. Gu, Selective laser melting additive manufacturing of Inconel 718 superalloy parts: Densification, microstructure and properties, J Alloys Compd. 585 (2014) 713–721. https://doi.org/10.1016/j.jallcom.2013.09.171.

[115] W.M. Tucho, P. Cuvillier, A. Sjolyst-Kverneland, V. Hansen, Microstructure and hardness studies of Inconel 718 manufactured by selective laser melting before and after solution heat treatment, Materials Science and Engineering A. 689 (2017) 220–232. https://doi.org/10.1016/j.msea.2017.02.062.

[116] K.N. Amato, S.M. Gaytan, L.E. Murr, E. Martinez, P.W. Shindo, J. Hernandez, S. Collins, F. Medina, Microstructures and mechanical behavior of Inconel 718 fabricated by selective laser melting, Acta Mater. 60 (2012) 2229–2239. https://doi.org/10.1016/j.actamat.2011.12.032.

[117] S. Zhang, L. Wang, X. Lin, H. Yang, W. Huang, The formation and dissolution mechanisms of Laves phase in Inconel 718 fabricated by selective laser melting compared to directed energy deposition and cast, Compos B Eng. 239 (2022). https://doi.org/10.1016/j.compositesb.2022.109994.

[118] R.J. Vikram, A. Singh, S. Suwas, Effect of heat treatment on the modification of microstructure of selective laser melted (SLM) IN718 and its consequences on mechanical behavior, J Mater Res. 35 (2020) 1949–1962. https://doi.org/10.1557/jmr.2020.129.

[119] D. Deng, R.L. Peng, H. Brodin, J. Moverare, Microstructure and mechanical properties of Inconel 718 produced by selective laser melting: Sample orientation dependence and effects of post heat treatments, Materials Science and Engineering A. 713 (2018) 294–306. https://doi.org/10.1016/j.msea.2017.12.043.

[120] J. Lee, M. Lee, I.D. Jung, J. Choe, J.-H. Yu, S. Kim, H. Sung, Correlation between microstructure and tensile properties of STS 316L and Inconel 718 fabricated by selective laser melting (SLM), J Nanosci Nanotechnol. 20 (2020) 6807–6814. https://doi.org/10.1166/jnn.2020.18792.

[121] Q. Zhang, P. Ren, X. Tu, Y. Dai, X. Wang, W. Li, Effect of heat treatment on microstructure evolution and mechanical properties of selective laser melted Inconel 718 alloy, J Mater Eng Perform. 28 (2019) 5376–5386. https://doi.org/10.1007/s11665-019-04309-3.

[122] F. Brenne, A. Taube, M. Pröbstle, S. Neumeier, D. Schwarze, M. Schaper, T. Niendorf, Microstructural design of ni-base alloys for high-temperature applications: impact of heat treatment on microstructure and mechanical properties after selective laser melting, Progress in Additive Manufacturing. 1 (2016) 141–151. https://doi.org/10.1007/s40964-016-0013-8.

[123] V.P. Sabelkin, G.R. Cobb, T.E. Shelton, M.N. Hartsfield, D.J. Newell, R.P. O'Hara, R.A. Kemnitz, Mitigation of anisotropic fatigue in nickel alloy 718 manufactured via selective laser melting, Mater Des. 182 (2019). https://doi.org/10.1016/j.matdes.2019.108095.

[124] M.E. Aydinöz, F. Brenne, M. Schaper, C. Schaak, W. Tillmann, J. Nellesen, T. Niendorf, On the microstructural and mechanical properties of post-treated additively manufactured Inconel 718 superalloy under quasi-static and cyclic loading, Materials Science and Engineering A. 669 (2016) 246–258. https://doi.org/10.1016/j.msea.2016.05.089.

[125] L. Huang, Y. Cao, G. Li, Y. Wang, Microstructure characteristics and mechanical behaviour of a selective laser melted Inconel 718 alloy, Journal of Materials Research and Technology. 9 (2020) 2440–2454. https://doi.org/10.1016/j.jmrt.2019.12.075.

[126] V.A. Popovich, E. v. Borisov, A.A. Popovich, V.S. Sufiiarov, D. v. Masaylo, L. Alzina, Impact of heat treatment on mechanical behaviour of Inconel 718 processed with tailored microstructure by selective laser melting, Mater Des. 131 (2017) 12–22. https://doi.org/10.1016/j.matdes.2017.05.065.

[127] Z. Liu, X. Li, X. Wang, C. Tian, L. Wang, Comparative investigation on grindability of Inconel 718 made by selective laser melting (SLM) and

casting, International Journal of Advanced Manufacturing Technology. 100 (2019) 3155–3166. https://doi.org/10.1007/s00170-018-2850-8.

[128] S. Raghavan, B. Zhang, P. Wang, C. Sun, M.L. Sharon, B. Zhang, P. Wang, C. Sun, M.L. Sharon, Effect of different heat treatments on the microstructure and mechanical properties in selective laser melted Inconel 718 alloy, Materials and Manufacturing Processes. 32 (2017) 1588–1595. https://doi.org/10.1080/10426914.2016.1257805.

[129] A. Mostafa, I.P. Rubio, V. Brailovski, M. Jahazi, M. Medraj, Structure, texture and phases in 3D printed IN718 alloy subjected to homogenization and HIP treatments, Metals (Basel). 7 (2017). https://doi.org/10.3390/met7060196.

[130] E.M. Fayed, M. Saadati, D. Shahriari, V. Brailovski, M. Jahazi, M. Medraj, Effect of homogenization and solution treatments time on the elevated-temperature mechanical behavior of Inconel 718 fabricated by laser powder bed fusion, Sci Rep. 11 (2021) 1–17. https://doi.org/10.1038/s41598-021-81618-5.

[131] T.B. Massalski, Binary Alloy Phase Diagrams, American society for Metals, 1987.

[132] M. Dadé, J. Malaplate, J. Garnier, F. de Geuser, F. Barcelo, P. Wident, A. Deschamps, Influence of microstructural parameters on the mechanical properties of oxide dispersion strengthened Fe-14Cr steels, Acta Mater. 127 (2017) 165–177. https://doi.org/10.1016/j.actamat.2017.01.026.

[133] R.L. Klueh, J.P. Shingledecker, R.W. Swindeman, D.T. Hoelzer, Oxide dispersion-strengthened steels: A comparison of some commercial and experimental alloys, Journal of Nuclear Materials. 341 (2005) 103–114. https://doi.org/10.1016/j.jnucmat.2005.01.017.

[134] G.R. Odette, M.J. Alinger, B.D. Wirth, Recent developments in irradiation-resistant steels, (2000). https://doi.org/10.1146/annurev.matsci.38.060407.130315.

[135] J. Jang, T.K. Kim, C.H. Han, H.K. Min, S.H. Jeong, D.H. Kim, A preliminary development and characterization of ni-based ODS alloys, Procedia Eng. 55 (2013) 284–288. https://doi.org/10.1016/j.proeng.2013.03.255.

[136] M.S. Dhanya, A.K. Shukla, S. Dineshraj, R.R. Kumar, K. Prabhakaran, S.V.S.N. Murty, P.R. Narayanan, Processing and characterization of yttria-dispersed Inconel 718 ODS alloy, Transactions of the Indian Institute of Metals. 72 (2019) 1395–1398. https://doi.org/10.1007/s12666-019-01649-5.

[137] M. Nganbe, M. Heilmaier, Modelling of particle strengthening in the γ′ and oxide dispersion strengthened nickel-base superalloy PM3030, Materials Science and Engineering A. 387–389 (2004) 609–612. https://doi.org/10.1016/j.msea.2004.01.109.

[138] R. Xu, Z. Geng, Y. Wu, C. Chen, M. Ni, D. Li, T. Zhang, H. Huang, F. Liu, R. Li, K. Zhou, Microstructure and mechanical properties of in-situ oxide-dispersion-strengthened NiCrFeY alloy produced by laser powder bed fusion, Advanced Powder Materials. 1 (2022) 100056. https://doi.org/10.1016/j.apmate.2022.100056.

[139] Q. song Song, Y. Zhang, Y. feng Wei, X. yi Zhou, Y. fu Shen, Y. min Zhou, X. mei Feng, Microstructure and mechanical performance of ODS superalloys manufactured by selective laser melting, Opt Laser Technol. 144 (2021). https://doi.org/10.1016/j.optlastec.2021.107423.

[140] S. Ukai, K. Taya, K. Nakamura, M.S. Aghamiri, N. Oono, S. Hayashi, T. Okuda, Directional recrystallization by zone annealing in a ni-based ODS superalloy, J Alloys Compd. 744 (2018) 204–210. https://doi.org/10.1016/j.jallcom.2018.01.406.

[141] W. He, F. Liu, L. Tan, L. Huang, Y. Nie, G. Wang, X. Zhan, Z. Qin, Bimodal-grained high-strength nickel-base ODS alloy fabricated by mechanical alloying and hot extrusion, Mater Today Commun. 26 (2021). https://doi.org/10.1016/j.mtcomm.2020.101921.

[142] L. Tan, G. Wang, Y. Guo, Q. Fang, Z. Liu, X. Xiao, W. He, Z. Qin, Y. Zhang, F. Liu, L. Huang, Additively manufactured oxide dispersion strengthened nickel-based superalloy with superior high temperature properties, Virtual Phys Prototyp. 15 (2020) 555–569. https://doi.org/10.1080/17452759.2020.1848283.

[143] X. Mao, K.H. Oh, J. Jang, Evolution of ultrafine grained microstructure and nano-sized semi-coherent oxide particles in austenitic oxide dispersion strengthened steel, Mater Charact. 117 (2016) 91–98. https://doi.org/10.1016/j.matchar.2016.04.022.

[144] R. Gao, L. Zeng, H. Ding, T. Zhang, X. Wang, Q. Fang, Characterization of oxide dispersion strengthened ferritic steel fabricated by electron beam selective melting, Mater Des. 89 (2016) 1171–1180. https://doi.org/10.1016/j.matdes.2015.10.073.

[145] M. Ni, C. Chen, R. Xu, S.R.E. Hosseini, R. Li, X. Zhang, K. Zhou, Microstructure and mechanical properties of additive manufactured Inconel 718 alloy strengthened by oxide dispersion with 0.3 wt% Sc addition, J Alloys Compd. 918 (2022). https://doi.org/10.1016/j.jallcom.2022.165763.

[146] C. Qiu, A new approach to synthesise high strength nano-oxide dispersion strengthened alloys, J Alloys Compd. 790 (2019) 1023–1033. https://doi.org/10.1016/j.jallcom.2019.03.221.

[147] M. Bartsch, A. Wasilkowska, A. Czyrska-Filemonowicz, U. Messerschmidt, Dislocation dynamics in the oxide dispersion strengthened alloy Incoloy MA956, 1999. www.elsevier.com/locate/msea.

[148] Z. Mao, L. Xiong, S. Liu, The formation of the complex oxide in ni-based alloy powder during mechanical milling and heat treatment, J Alloys Compd. 879 (2021). https://doi.org/10.1016/j.jallcom.2021.160333.

[149] M.B. Wilms, S.K. Rittinghaus, M. Goßling, B. Gökce, Additive manufacturing of oxide-dispersion strengthened alloys: Materials, synthesis and manufacturing, Prog Mater Sci. 133 (2023). https://doi.org/10.1016/j.pmatsci.2022.101049.

[150] R. Nunes, J.H. Adams, J.C. Bean, B. Laboratories, B.J. Beaudry, David, F. Berry, ASM Handbook Volume 2 - Properties and Selection: Nonferrous Alloys and Special-purpose Materials, 1990.

[151] C. Suryanarayana, Mechanical Alloying and Milling, Prog Mater Sci. 46 (2001) 1–184. www.elsevier.com/locate/pmatsci.

[152] L. Lü, M.O. Lai, Introduction to Mechanical Alloying, in: Mechanical Alloying, Springer, Boston, MA, 1998. https://doi.org/10.1007/978-1-4615-5509-4_1.

[153] C.A. Williams, P. Unifantowicz, N. Baluc, G.D.W. Smith, E.A. Marquis, The formation and evolution of oxide particles in oxide-dispersion- strengthened ferritic steels during processing, Acta Mater. 61 (2013) 2219–2235. https://doi.org/10.1016/j.actamat.2012.12.042.

[154] Z.W. Zhang, L. Yao, X.L. Wang, M.K. Miller, Vacancy-controlled ultrastable nanoclusters in nanostructured ferritic alloys, Sci Rep. 5 (2015). https://doi.org/10.1038/srep10600.

[155] M.J. Alinger, G.R. Odette, D.T. Hoelzer, On the role of alloy composition and processing parameters in nanocluster formation and dispersion strengthening in nanostuctured ferritic alloys, Acta Mater. 57 (2009) 392–406. https://doi.org/10.1016/j.actamat.2008.09.025.

[156] M. Brocq, B. Radiguet, J.M. le Breton, F. Cuvilly, P. Pareige, F. Legendre, Nanoscale characterisation and clustering mechanism in an Fe-Y2O3 model ODS alloy processed by reactive ball milling and annealing, Acta Mater. 58 (2010) 1806–1814. https://doi.org/10.1016/j.actamat.2009.11.022.

[157] M.J. Alinger, G.R. Odette, D.T. Hoelzer, The development and stability of Y-Ti-O nanoclusters in mechanically alloyed Fe-Cr based ferritic alloys, in: Journal of Nuclear Materials, 2004: pp. 382–386. https://doi.org/10.1016/j.jnucmat.2004.04.042.

[158] J. Wang, S. Liu, B. Xu, M. Sun, X. Liu, D. Li, Y. Li, Microstructural stability of a 9Cr oxide dispersion strengthened alloy under thermal aging at high temperatures, J Alloys Compd. 932 (2023). https://doi.org/10.1016/j.jallcom.2022.167691.

[159] A. Arora, S. Mula, Effect of Ti addition on thermal stability and phase evolution of super-invar based yttria added ODS alloys developed by mechanical alloying and spark plasma sintering, J Alloys Compd. 899 (2022). https://doi.org/10.1016/j.jallcom.2021.163336.

[160] N. Cunningham, Y. Wu, D. Klingensmith, G.R. Odette, On the remarkable thermal stability of nanostructured ferritic alloys, Materials Science and Engineering A. 613 (2014) 296–305. https://doi.org/10.1016/j.msea.2014.06.097.

[161] J. Shen, H. Yang, Y. Li, S. Kano, Y. Matsukawa, Y. Satoh, H. Abe, Microstructural stability of an as-fabricated 12Cr-ODS steel under elevated-temperature annealing, J Alloys Compd. 695 (2017) 1946–1955. https://doi.org/10.1016/j.jallcom.2016.11.029.

[162] L. Wang, Z. Bai, H. Shen, C. Wang, T. Liu, Creation of Y2Ti2O7 nanoprecipitates to strengthen the Fe-14Cr-3Al-2W steels by adding Ti hydride and Y2O3 nanoparticles, Journal of Nuclear Materials. 488 (2017) 319–327. https://doi.org/10.1016/j.jnucmat.2017.03.015.

[163] X. Boulnat, M. Perez, D. Fabrègue, S. Cazottes, Y. de Carlan, Characterization and modeling of oxides precipitation in ferritic steels during fast non-isothermal consolidation, Acta Mater. 107 (2016) 390–403. https://doi.org/10.1016/j.actamat.2016.01.034.

[164] J. Shen, Y. Li, F. Li, H. Yang, Z. Zhao, S. Kano, Y. Matsukawa, Y. Satoh, H. Abe, Microstructural characterization and strengthening mechanisms of a 12Cr-ODS steel, Materials Science and Engineering A. 673 (2016) 624–632. https://doi.org/10.1016/j.msea.2016.07.030.

[165] P. Dou, L. Qiu, S. Jiang, A. Kimura, Crystal and metal/oxide interface structures of nanoparticles in Fe–16Cr–0.1Ti–0.35Y2O3 ODS steel, Journal of Nuclear Materials. 523 (2019) 320–332. https://doi.org/10.1016/j.jnucmat.2019.05.015.

[166] A. Hirata, T. Fujita, C.T. Liu, M.W. Chen, Characterization of oxide nanoprecipitates in an oxide dispersion strengthened 14YWT steel using aberration-corrected STEM, Acta Mater. 60 (2012) 5686–5696. https://doi.org/10.1016/j.actamat.2012.06.042.

[167] S. Yamashita, S. Ohtsuka, N. Akasaka, S. Ukai, S. Ohnuki, Formation of nanoscale complex oxide particles in mechanically alloyed ferritic steel, Philos Mag Lett. 84 (2004) 525–529. https://doi.org/10.1080/09500830412331303609.

[168] M.K. Miller, D.T. Hoelzer, E.A. Kenik, K.F. Russell, Nanometer scale precipitation in ferritic MA/ODS alloy MA957, in: Journal of Nuclear Materials, 2004: pp. 338–341. https://doi.org/10.1016/j.jnucmat.2004.04.085.

[169] C.W. Park, J.M. Byun, W.J. Choi, S.Y. Lee, Y. do Kim, Improvement of high temperature mechanical properties of ni-based oxide dispersion strengthened alloys by preferential formation of Y-Ti-O complex oxide, Materials Science and Engineering A. 740–741 (2019) 363–367. https://doi.org/10.1016/j.msea.2018.10.004.

[170] V. Sagaradze, A. Litvinov, V. Shabashov, N. Vil'danova, A. Mukoseev, K. Kozlov, New method of mechanical alloying of ODS steels using iron oxides, Physics of Metals and Metallography. 101 (2006) 566–576. https://doi.org/10.1134/S0031918X06060081.

[171] L. Barnard, G.R. Odette, I. Szlufarska, D. Morgan, An ab initio study of Ti-Y-O nanocluster energetics in nanostructured ferritic alloys, Acta Mater. 60 (2012) 935–947. https://doi.org/10.1016/j.actamat.2011.11.011.

[172] Y. Jiang, J.R. Smith, G.R. Odette, Formation of Y-Ti-O nanoclusters in nanostructured ferritic alloys: A first-principles study, Phys Rev B Condens Matter Mater Phys. 79 (2009). https://doi.org/10.1103/PhysRevB.79.064103.

[173] Y. Wen, Y. Liu, D. Liu, B. Tang, C.T. Liu, Microstructural evolution of ferritic steel powder during mechanical alloying with iron oxide, n.d. www.hanser-elibrary.com.

[174] Q. Tang, T. Hoshino, S. Ukai, B. Leng, S. Hayashi, Y. Wang, Refinement of oxide particles by addition of Hf in Ni-0.5mass%Al- 1mass%Y2O3 alloys, Mater Trans. 51 (2010) 2019–2024. https://doi.org/10.2320/matertrans.M2010163.

[175] N. Oono, Q.X. Tang, S. Ukai, Oxide particle refinement in ni-based ODS alloy, Materials Science and Engineering A. 649 (2016) 250–253. https://doi.org/10.1016/j.msea.2015.09.094.

[176] L. Yu, Z. Lu, S. Peng, X. Li, Effect of Al/Ti ratio on γ′ and oxide dispersion strengthening in ni-based ODS superalloys, Materials Science and Engineering A. 845 (2022). https://doi.org/10.1016/j.msea.2022.143240.

[177] H. Dong, L. Yu, Y. Liu, C. Liu, H. Li, J. Wu, Effect of hafnium addition on the microstructure and tensile properties of aluminum added high-Cr ODS steels, J Alloys Compd. 702 (2017) 538–545. https://doi.org/10.1016/j.jallcom.2017.01.298.

[178] Q. Tang, S. Ukai, N. Oono, S. Hayashi, B. Leng, Y. Sugino, W. Han, T. Okuda, Oxide particle refinement in 4.5 mass%Al Ni-based ODS superalloys, in: Mater Trans, 2012: pp. 645–651. https://doi.org/10.2320/matertrans.M2011251.

[179] L. Zhang, S. Ukai, T. Hoshino, S. Hayashi, X. Qu, Y2O3 evolution and dispersion refinement in co-base ODS alloys, Acta Mater. 57 (2009) 3671–3682. https://doi.org/10.1016/j.actamat.2009.04.033.

[180] P. Dou, A. Kimura, R. Kasada, T. Okuda, M. Inoue, S. Ukai, S. Ohnuki, T. Fujisawa, F. Abe, S. Jiang, Z. Yang, TEM and HRTEM study of oxide particles in an Al-alloyed high-Cr oxide dispersion strengthened ferritic steel with Hf addition, Journal of Nuclear Materials. 485 (2017) 189–201. https://doi.org/10.1016/j.jnucmat.2016.12.001.

[181] S.M. Seyyed Aghamiri, H.R. Shahverdi, S. Ukai, N. Oono, K. Taya, S. Miura, S. Hayashi, T. Okuda, Microstructural characterization of a new mechanically alloyed ni-base ODS superalloy powder, Mater Charact. 100 (2015) 135–142. https://doi.org/10.1016/j.matchar.2014.12.008.

[182] T. Antonsson, H. Fredriksson, The effect of cooling rate on the solidification of Inconel 718, Metallurgical and Materials Transactions B: Process Metallurgy and Materials Processing Science. 36B (2005) 85–96.

[183] L. Tan, Y. Yang, In situ phase transformation of Laves phase from Chi-phase in Mo-containing Fe-Cr-Ni alloys, Mater Lett. 158 (2015) 233–236. https://doi.org/10.1016/j.matlet.2015.06.018.

[184] U.R. Kattner, The CALPHAD method and its role In material and process development, Tecnol Metal Mater Min. 13 (2016) 3–15. https://doi.org/10.4322/2176-1523.1059.

[185] J. Agren, Calculation of phase diagrams: Calphad, Curr Opin Solid State Mater Sci. 1 (1996) 355–360.

[186] C.W. Bale, E. Belisle, P. Chartrand, S.A. Decterov, G. Eriksson, A.E. Gheribi, K. Hack, I.H. Jung, Y.B. Kang, J. Melançon, A.D. Pelton, S. Petersen, C. Robelin, J. Sangster, P. Spencer, M.A. van Ende, FactSage thermochemical software and databases - 2010-2016, CALPHAD. 54 (2016) 35–53. www.factsage.com.

[187] ShefkiEsadi, J. Fazlic, Open databases. Matcalc., (n.d.). https://www.matcalc.at/index.php/databases/open-databases.

[188] GTT-Technologies, The ab initio materials project (AIMP) v4.0 database AiMP-v4.0-documentation, (2021). https://gtt-technologies.de/wp-content/uploads/2021/04/AiMP-v4.0-documentation.pdf.

[189] Oerlikon Metco, MetcoAdd 718C, (n.d.). https://mymetco.oerlikon.com/en-us/product/metcoadd718c (accessed December 29, 2022).

[190] N.J. Cunningham, Y. Wu, A. Etienne, E.M. Haney, G.R. Odette, E. Stergar, D.T. Hoelzer, Y.D. Kim, B.D. Wirth, S.A. Maloy, Effect of bulk oxygen on 14YWT nanostructured ferritic alloys, Journal of Nuclear Materials. 444 (2014) 35–38. https://doi.org/10.1016/j.jnucmat.2013.09.013.

[191] J. Zhang, Y. Li, F. Bao, X. Rui, Z. Duan, W. Yan, Q. Shi, W. Wang, Y. Shan, K. Yang, Study on the formation mechanism of Y-Ti-O oxides during mechanical milling and annealing treatment, Advanced Powder Technology. 32 (2021) 582–590. https://doi.org/10.1016/j.apt.2021.01.005.

[192] K. Gruber, R. Dziedzic, B. Kuźnicka, B. Madejski, M. Malicki, Impact of high temperature stress relieving on final properties of Inconel 718 processed by laser powder bed fusion, Materials Science and Engineering A. 813 (2021). https://doi.org/10.1016/j.msea.2021.141111.

[193] ASTM, Designation: E8/E8M − 16a Standard Test Methods for Tension Testing of Metallic Materials 1, n.d. https://doi.org/10.1520/E0008_E0008M-16A.

[194] ASTM E21-20, Standard Test Methods for Elevated Temperature Tension Tests of Metallic Materials 1, n.d. https://doi.org/10.1520/E0021-20.

[195] ISO 6892-1, Metallic materials-Tensile testing-Part 1: Method of test at room temperature, 2009. www.iso.org.

[196] ISO 6892-2, Metallic materials-Tensile testing-Part 2: Method of test at elevated temperature, 2018. www.iso.org.

[197] E. Aydogan, O. El-Atwani, S. Takajo, S.C. Vogel, S.A. Maloy, High temperature microstructural stability and recrystallization mechanisms in 14YWT alloys, Acta Mater. 148 (2018) 467–481. https://doi.org/10.1016/j.actamat.2018.02.006.

[198] E. Aydogan, S.A. Maloy, O. Anderoglu, C. Sun, J.G. Gigax, L. Shao, F.A. Garner, I.E. Anderson, J.J. Lewandowski, Effect of tube processing methods on microstructure, mechanical properties and irradiation response of 14YWT nanostructured ferritic alloys, Acta Mater. 134 (2017) 116–127. https://doi.org/10.1016/j.actamat.2017.05.053.

[199] J. Holzer, Gamanov, N. Luptáková, A. Dlouhý, J. Svoboda, Coarsening kinetics of Y2O3 dispersoid in new grade of Fe-Al-Cr-based ODS alloy, Metals (Basel). 12 (2022). https://doi.org/10.3390/met12020210.

[200] Y.T. Chen, A.C. Yeh, M.Y. Li, S.M. Kuo, Effects of processing routes on room temperature tensile strength and elongation for Inconel 718, Mater Des. 119 (2017) 235–243. https://doi.org/10.1016/j.matdes.2017.01.069.

[201] Z. Chen, R.L. Peng, J. Moverare, P. Avdovic, J.M. Zhou, S. Johansson, Surface integrity and structural stability of broached Inconel 718 at high temperatures, Metall Mater Trans A Phys Metall Mater Sci. 47 (2016) 3664–3676. https://doi.org/10.1007/s11661-016-3515-6.

[202] J. Lacaze, M. Dehmas, A. Niang, B. Viguier, TEM study of high-temperature precipitation of delta phase in Inconel 718 alloy, Advances in Materials Science and Engineering. 2011 (2011). https://doi.org/10.1155/2011/940634.

[203] M. Zhang, C.N. Sun, X. Zhang, P.C. Goh, J. Wei, D. Hardacre, H. Li, Fatigue and fracture behaviour of laser powder bed fusion stainless steel 316L: Influence of processing parameters, Materials Science and Engineering A. 703 (2017) 251–261. https://doi.org/10.1016/j.msea.2017.07.071.

[204] W. Wang, J. Ning, S.Y. Liang, Analytical prediction of balling, lack-of-fusion and keyholing thresholds in powder bed fusion, Applied Sciences (Switzerland). 11 (2021). https://doi.org/10.3390/app112412053.

[205] W. Wang, Z. Chen, W. Lu, F. Meng, T. Zhao, Heat treatment for selective laser melting of Inconel 718 alloy with simultaneously enhanced tensile strength and fatigue properties, J Alloys Compd. 913 (2022). https://doi.org/10.1016/j.jallcom.2022.165171.

[206] H.Y. Wan, Z.J. Zhou, C.P. Li, G.F. Chen, G.P. Zhang, Effect of scanning strategy on mechanical properties of selective laser melted Inconel 718, Materials Science and Engineering A. 753 (2019) 42–48. https://doi.org/10.1016/j.msea.2019.03.007.

[207] H. Sakasegawa, F. Legendre, L. Boulanger, M. Brocq, L. Chaffron, T. Cozzika, J. Malaplate, J. Henry, Y. de Carlan, Stability of non-stoichiometric clusters in the MA957 ODS ferrtic alloy, Journal of Nuclear Materials. 417 (2011) 229–232. https://doi.org/10.1016/j.jnucmat.2010.12.056.

[208] S. Tabaie, F. Rézaï-Aria, M. Jahazi, Microstructure evolution of selective laser melted Inconel 718: Influence of high heating rates, Metals (Basel). 10 (2020). https://doi.org/10.3390/met10050587.

[209] J. Svoboda, V. Horník, L. Stratil, H. Hadraba, B. Mašek, O. Khalaj, H. Jirková, Microstructure evolution in ODS alloys with a high-volume fraction

of nano oxides, Metals (Basel). 8 (2018). https://doi.org/10.3390/met8121079.

[210] M. Garibaldi, I. Ashcroft, M. Simonelli, R. Hague, Metallurgy of high-silicon steel parts produced using selective laser melting, Acta Mater. 110 (2016) 207–216. https://doi.org/10.1016/j.actamat.2016.03.037.

[211] M. Gerstgrasser, M. Cloots, J. Stirnimann, K. Wegener, Residual stress reduction of LPBF-processed CM247LC samples via multi laser beam strategies, The International Journal of Advanced Manufacturing Technology. 117 (2021) 2093–2103. https://doi.org/10.1007/s00170-021-07083-6/Published.

[212] L.N. Carter, C. Martin, P.J. Withers, M.M. Attallah, The influence of the laser scan strategy on grain structure and cracking behaviour in SLM powder-bed fabricated nickel superalloy, J Alloys Compd. 615 (2014) 338–347. https://doi.org/10.1016/j.jallcom.2014.06.172.

[213] S. Holland, X. Wang, X.Y. Fang, Y.B. Guo, F. Yan, L. Li, Grain boundary network evolution in Inconel 718 from selective laser melting to heat treatment, Materials Science and Engineering A. 725 (2018) 406–418. https://doi.org/10.1016/j.msea.2018.04.045.

[214] S.I. Wright, M.M. Nowell, D.P. Field, A review of strain analysis using electron backscatter diffraction, Microscopy and Microanalysis. 17 (2011) 316–329. https://doi.org/10.1017/S1431927611000055.

[215] A.J. Schwartz, M. Kumar, B.L. Adams, D.P. Field, Electron Backscatter Diffraction in Materials Science, Springer US, 2009. https://doi.org/10.1007/978-0-387-88136-2.

[216] E. Aydogan, O. El-Atwani, B. Erdem, W.Y. Chen, M. Li, A. Devaraj, B. Koc, S.A. Maloy, In-situ radiation response of additively manufactured modified Inconel 718 alloys, Addit Manuf. 51 (2022). https://doi.org/10.1016/j.addma.2022.102601.

[217] H. Sakasegawa, F. Legendre, L. Boulanger, L. Chaffron, T. Cozzika, J. Malaplate, J. Henry, Y. de Carlan, M. Brocq, Mechanism of oxide particle evolution in the MA957 ODS ferritic alloy, Materials Research Society Symposium Proceedings. 1125 (2009) 25–28. https://doi.org/10.1557/proc-1125-r01-03.

[218] H. Sakasegawa, L. Chaffron, F. Legendre, L. Boulanger, T. Cozzika, M. Brocq, Y. de Carlan, Correlation between chemical composition and size of very small oxide particles in the MA957 ODS ferritic alloy, Journal of Nuclear Materials. 384 (2009) 115–118. https://doi.org/10.1016/j.jnucmat.2008.11.001.

[219] R. Husák, H. Hadraba, Z. Chlup, M. Heczko, T. Kruml, V. Puchý, ODS EUROFER steel strengthened by Y-(Ce, Hf, La, Sc, and Zr) complex oxides, Metals (Basel). 9 (2019). https://doi.org/10.3390/met9111148.

[220] K.A. Unocic, B.A. Pint, D.T. Hoelzer, Advanced TEM characterization of oxide nanoparticles in ODS Fe–12Cr–5Al alloys, J Mater Sci. 51 (2016) 9190–9206. https://doi.org/10.1007/s10853-016-0111-5.

[221] X. Liu, Y. Miao, Y. Wu, S.A. Maloy, J.F. Stubbins, Stability of nanoclusters in an oxide dispersion strengthened alloy under neutron irradiation, Scr Mater. 138 (2017) 57–61. https://doi.org/10.1016/j.scriptamat.2017.05.023.

[222] H.J. Chang, H.Y. Cho, J.H. Kim, Stability of Y-Ti-O nanoparticles during laser melting of advanced oxide dispersion-strengthened steel powder, J Alloys Compd. 653 (2015) 528–533. https://doi.org/10.1016/j.jallcom.2015.08.273.

[223] M.K. Miller, C.M. Parish, Q. Li, Advanced oxide dispersion strengthened and nanostructured ferritic alloys, Materials Science and Technology (United Kingdom). 29 (2013) 1174–1178. https://doi.org/10.1179/1743284713Y.0000000207.

[224] M. Li, Y. Guo, H. Wang, J. Shan, Y. Chang, Microstructures and mechanical properties of oxide dispersion strengthened CoCrFeNi high-entropy alloy produced by mechanical alloying and spark plasma sintering, Intermetallics (Barking). 123 (2020). https://doi.org/10.1016/j.intermet.2020.106819.

[225] Y. Wang, J. Shi, Effect of post heat treatment on the microstructure and tensile properties of nano TiC particulate reinforced Inconel 718 by selective laser melting, Journal of Manufacturing Science and Engineering, Transactions of the ASME. 142 (2020) 1–12. https://doi.org/10.1115/1.4046646.

[226] D. Du, A. Dong, D. Shu, G. Zhu, B. Sun, X. Li, E. Lavernia, Influence of build orientation on microstructure, mechanical and corrosion behavior of Inconel 718 processed by selective laser melting, Materials Science and Engineering A. 760 (2019) 469–480. https://doi.org/10.1016/j.msea.2019.05.013.

[227] X. Li, J.J. Shi, G.H. Cao, A.M. Russell, Z.J. Zhou, C.P. Li, G.F. Chen, Improved plasticity of Inconel 718 superalloy fabricated by selective laser melting through a novel heat treatment process, Mater Des. 180 (2019). https://doi.org/10.1016/j.matdes.2019.107915.

[228] R. Sun, W. Li, Y. Zhang, T. Hu, P. Wang, Effect of solution treatment on high-temperature mechanical properties of IN718 manufactured by selective laser melting, J Mater Eng Perform. 30 (2021) 6821–6831. https://doi.org/10.1007/s11665-021-06024-4.

[229] T.D. McLouth, D.B. Witkin, J.R. Lohser, S.D. Sitzman, P.M. Adams, Z.R. Lingley, G.E. Bean, J.M. Yang, R.J. Zaldivar, Temperature and strain-rate dependence of the elevated temperature ductility of Inconel 718 prepared by selective laser melting, Materials Science and Engineering A. 824 (2021). https://doi.org/10.1016/j.msea.2021.141814.

[230] S. Sreekanth, K. Hurtig, S. Joshi, J. Andersson, Effect of process parameters and heat treatments on delta-phase precipitation in directed energy deposited

alloy 718, Welding in the World. 66 (2022) 863–877. https://doi.org/10.1007/s40194-022-01253-0.

[231] P. Liu, S.Y. Sun, S.B. Xu, M.Q. Cao, C. Hong, J.Y. Hu, Effect of solid solution + double ageing on microstructure and properties in the layer by layer of the Z-Y interface of Inconel 718 alloys fabricated by SLM, Materials Research. 21 (2018). https://doi.org/10.1590/1980-5373-mr-2018-0395.

[232] S.M. Seyyed Aghamiri, H.R. Shahverdi, S. Ukai, N. Oono, M.N. Ahmadabadi, T. Okuda, Nanoscale lamellar γ/γ′ structure and preferred distribution of oxide particles in a new ODS superalloy, Mater Lett. 161 (2015) 568–571. https://doi.org/10.1016/j.matlet.2015.08.107.

[233] A. Devaux, A. Helstroffer, J. Cormier, P. Villechaise, J. Douin, M. Hantcherli, F. Pettinari-Sturmel, Effect of aging heat-treatment on mechanical properties of AD730^{TM} superalloy, in: 8th International Symposium on Superalloy 718 and Derivatives, Wiley-TMS [Imprint], 2014: pp. 521–535.

[234] Y. Zhao, L. Hao, Q. Zhang, W. Xiong, Phase transformations during continuous cooling in Inconel 718 alloys manufactured by laser powder bed fusion and suction casting, Mater Charact. 185 (2022). https://doi.org/10.1016/j.matchar.2022.111764.

[235] J. Ding, S. Xue, Z. Shang, J. Li, Y. Zhang, R. Su, T. Niu, H. Wang, X. Zhang, Characterization of precipitation in gradient Inconel 718 superalloy, Materials Science and Engineering A. 804 (2021). https://doi.org/10.1016/j.msea.2020.140718.

[236] H. Qi, M. Azer, A. Ritter, Studies of standard heat treatment effects on microstructure and mechanical properties of laser net shape manufactured Inconel 718, Metall Mater Trans A Phys Metall Mater Sci. 40 (2009) 2410–2422. https://doi.org/10.1007/s11661-009-9949-3.

[237] J. Wang, S. Liu, B. Xu, J. Zhang, M. Sun, D. Li, Research progress on preparation technology of oxide dispersion strengthened steel for nuclear

energy, International Journal of Extreme Manufacturing. 3 (2021). https://doi.org/10.1088/2631-7990/abff1a.

[238] T. Alam, M. Chaturvedi, S.P. Ringer, J.M. Cairney, Precipitation and clustering in the early stages of ageing in Inconel 718, Materials Science and Engineering A. 527 (2010) 7770–7774. https://doi.org/10.1016/j.msea.2010.08.053.

APPENDICES

A. TEZ İZİN FORMU / THESIS PERMISSION FORM

TEZ İZİN FORMU / THESIS PERMISSION FORM

ENSTİTÜ / INSTITUTE

Fen Bilimleri Enstitüsü / Graduate School of Natural and Applied Sciences	x
Sosyal Bilimler Enstitüsü / Graduate School of Social Sciences	
Uygulamalı Matematik Enstitüsü / Graduate School of Applied Mathematics	
Enformatik Enstitüsü / Graduate School of Informatics	
Deniz Bilimleri Enstitüsü / Graduate School of Marine Sciences	

YAZARIN / AUTHOR

Soyadı / Surname : YALÇIN
Adı / Name : Merve Yeşim
Bölümü / Department : Metalurji ve Malzeme Mühendisliği

TEZİN ADI / TITLE OF THE THESIS (İngilizce / English) : Microstructural and Mechanical Properties of Oxide Dispersion Strengthened INCONEL 718 Alloys Produced by Selective Laser Melting

TEZİN TÜRÜ / DEGREE: Yüksek Lisans / Master [x] Doktora / PhD [ ]

1. Tezin tamamı dünya çapında erişime açılacaktır. / Release the entire work immediately for access worldwide. [ ]
2. Tez iki yıl süreyle erişime kapalı olacaktır. / Secure the entire work for patent and/or proprietary purposes for a period of two year. * [ ]
3. Tez altı ay süreyle erişime kapalı olacaktır. / Secure the entire work for period of six months. * [x]

** Enstitü Yönetim Kurulu Kararının basılı kopyası tezle birlikte kütüphaneye teslim edilecektir. A copy of the Decision of the Institute Administrative Committee will be delivered to the library together with the printed thesis.*

Yazarın imzası / Signature ..... Tarih / Date .....

SKB-SA02/F01 Rev:03 06.08.2018